Optical Fiber Taper Coupled Glass Microsphere Resonators

Thesis by

Ming Cai

In Partial Fulfillment of the Requirements

for the Degree of

Doctor of Philosophy

California Institute of Technology

Pasadena, California

2001

(defended May 14, 2001)

To My Family

Acknowledgments

First and foremost, I wish to express my deepest gratitude to Professor Kerry Vahala. I feel privileged to have him as my advisor. His way of thinking, along with his brilliant ideas, deeply affects my thoughts on the scientific research. This work was possible because of his constant stimulation, keen vision and full support. I feel honored to have been a part of his research group for the past four years and I am sure that his example as both a teacher and a scientist will continue to inspire me in the future.

I am also very grateful to Dr. Guido Hunziker, Dr. Oskar Painter, Dr. Per Olof Henderkvist, and Dr. Peter Sercel for sharing their years of experience and for their excellent collaboration. Their inspiring discussion and valuable advice have made a good contribution to this thesis. I would also like to thank Michael Shumway for his great help to get me started at the early stage of this project.

My special thanks go to all other members of the Vahala group, past and present, who helped me make my Ph.D. pursuit enjoyable and rewarding: Dr. Roberto Paiella, Dr. Mark Brongersma, Dr. Elizabeth Boer, Dr. David Dougherty and Lan Yang, and who were willing to share with me the laboratory equipment: Ashish Bhardwaj, Sean Spillane, and Tobias Kippenberg.

I would further like to say thanks to Dr. Paul Bridger for his wonderful idea on the microsphere sensors.

I would also like to express my gratitude to Prof. William Bridges for his valuable advice on my thesis.

I am also grateful to Rosalie Rowe for her generous help with administrative matters, and Larry Begay for his great patience and incredible skills on machine designs that made the experiments possible.

Most of all, my deepest gratitude goes to my parents, my sister, and Wenjiu for their unconditional patience, support and encouragement through many years. Without their love, the task of completing this thesis would not have been as enjoyable as it has been.

Abstract

This thesis studies optical fiber taper coupled dielectric microsphere resonators and their applications. Fundamental properties including ideal coupling and critical coupling in an optical fiber taper to fused silica glass microsphere coupling system is investigated both theoretically and experimentally. A symmetrical dual-taper coupling configuration is proposed to obtain highly efficient power transfer from the taper coupler to the microsphere resonator. Applications as channel add/drop filters and microsphere lasers are also demonstrated.

The physical essence of the fiber taper to silica microsphere is analyzed using a two-dimensional model. The relationship between the coupling strength and the cavity loss is unveiled. Adiabatic tapers and high-quality microspheres are fabricated and used to demonstrate actual coupling systems. Perfect agreement between the experimental results and the theoretical prediction is presented.

Power transfer from the taper to a microsphere resonator has been significantly improved by employing a dual-taper symmetrically coupling configuration. Up to -28 dB extinction at the central resonant wavelength has been measured.

We then propose a device application of the taper-sphere-taper structure as a channel add/drop filter in the wavelength division multiplexing systems. For a filter with a bandwidth of 3.8 GHz and a dropping channel isolation of 26 dB, the bit-error-rate measurement shows no power penalty at 2.5 Gbit/s.

A 1.5 μm wavelength single-frequency fiber laser is also demonstrated using a single tapered fiber coupling to a highly doped erbium:ytterbium phosphate glass microsphere. The fiber taper serves the dual purpose of transporting optical pump power into the sphere and extracting the resulting laser emission. As low as 60 μW pump threshold and fiber-coupled output power as high as 3 μW with single mode operation are obtained. Imaging of photoluminescence from the sphere at visible wavelengths reveals the pump power is resonantly coupled into semiclassical orbits due to the strong absorption damping in the phosphate glass. A bi-sphere laser system consisting of two microspheres attached to a single fiber taper is also demonstrated.

Finally, a novel hybrid fiber taper, made from a combination of a 980 nm single mode fiber and a 1550 nm single mode fiber, is proposed and demonstrated as the microsphere laser coupler. Both the pump wave and laser emission are found to be more efficiently coupled to and from, respectively, the sphere modes. As high as 112 μW single-frequency laser output power is measured with a differential quantum efficiency of 12%.

Contents

1 Introduction **1**

2 Whispering Gallery Modes in Dielectric Microspheres **7**

2.1 Introduction 7

2.2 Electromagnetic fields in a spherical coordinate system 9

2.3 Whispering gallery modes in microspheres 11

2.3.1 Resonant Mode Distribution in Microspheres 11

2.3.2 Identification of Whispering Gallery Modes 12

2.3.3 Characteristic Equations of Whispering Gallery Modes 14

2.3.4 Quality Factors of Microsphere Resonators 15

2.4 Pictures of Whispering Gallery Modes 17

3 Tapered Optical Fiber to Microsphere Coupling **22**

3.1 Introduction 22

3.2 Modes in Tapered Fiber Couplers 26

3.2.1 Characteristics of Taper Modes 27

3.2.2 Propagation Along Tapered Fibers 32

3.3 Modeling of Taper to Microsphere Coupling 34

3.4 Symmetrical Taper-Resonator-Taper Structure 39

4 Fabrication of Microspheres and Fiber Tapers 46

4.1 Introduction 46

4.2 Fabrication of High-Quality Microspheres 47

4.2.1 Description of Microsphere Fabrication Setup 47

4.2.2 Eccentricity of Real Microspheres 51

4.3 Fabrication of Tapered Fibers 52

4.4 Typical Measurement Setups 55

5 Experimental Observation of Taper to Sphere Coupling 61

5.1 Introduction 61

5.2 Observation of Ideal Coupling 63

5.3 Observation of Critical Coupling 64

5.4 Highly Efficient Power Transfer in a Taper-Resonator-Taper Structure 70

6 Applications Towards Channel Add/Drop Filters 81

6.1 Introduction 82

6.2 All Fiber-Optic Micropshere Channel Add/Drop Devices 84

6.3 Performance of Microsphere Channel Add/Drop Filters 86

6.4 Discussion and Conclusion 91

7 Applications Towards Microsphere Lasers 93

7.1 Introduction 93

7.2 Microsphere Laser Characteristics 94

7.2.1 Erbium:Ytterbium Co-Doped Phosphate Glass 94

7.2.2 Typical Microsphere Laser Performance 97

7.3 Interpretation of the Lasing Action 103

7.3.1 Estimation of the Laser Threshold 103

7.3.2 Resonantly Pumping into the Microsphere 107

7.3.3 Single-Mode Laser Oscillation 116

7.3.4 Temporal Response of the Laser Oscillation 119

7.4 Bi-Sphere Experiment 120

7.5 Hybrid Taper Coupled Microsphere Lasers 122

List of Figures

2.1	Ray path of a tangentially incident ray inside a microsphere	8
2.2	Schematic of the mode propagation constants along the surface of a sphere	13
2.3	Numerical simulation of the electric field distribution for a fundamental mode	17
2.4	Field intensity distribution in a sphere having radius of 25 μm	18
2.5	Calculated resonant frequencies of TE and TM whispering gallery modes for a sphere of $R = 25\ \mu m$	19
3.1	Schematic of a high index prism coupling to a microsphere	23
3.2	Modified prism coupler — angle-polished optical fiber coupler	23
3.3	Polished or eroded optical fiber coupler	25
3.4	Tapered optical fiber coupler	25
3.5	Effective mode index as a function of the core diameter of an optical fiber at 1550 nm	30
3.6	Effective mode index as a function of taper diameter at 1550 nm	30
3.7	Phase matching between the taper and sphere modes	31

3.8	Illustration of a gradually tapered optical fiber	33
3.9	Illustration of a two-dimensional system that consists of a straight waveguide coupler and a disk resonator	36
3.10	Power transmission through the coupler as a function of internal round trip loss factor α	39
3.11	Schematic of a taper-resonator-taper coupling structure	41
4.1	Setup for fabricating microspheres	48
4.2	Magnified pictures of microspheres	49
4.3	Fabrication setup for fiber tapers	53
4.4	Magnified photograph of a tapered fiber	54
4.5	Schematic of the transmission spectrum measurement setup	56
4.6	Experimental setup for characterizing the taper-sphere coupling system	56
4.7	Magnified photography of a single fiber taper to microsphere coupling system	57
4.8	Typical transmission spectrum	57
4.9	Magnified photography of a double-taper to sphere coupling system	59
5.1	Typical transmission spectrum for the microsphere-taper system	66
5.2	Normalized transmission as a function of the probe position	67
5.3	Power transmission as a function of the linewidth (FWHM) of the mode for varying probe position	69
5.4	Power transmission as a function of the linewidth (FWHM) of the mode for varying taper-sphere coupling gap	69

5.5	Normalized transmission spectrum for a single taper coupled microsphere resonator system.	72
5.6	Calculated coupling coefficients κ_1^2 and total cavity loss β_1^2	72
5.7	Microsphere resonator in the dual-taper coupling configuration	74
5.8	Normalized transmission spectra for the dual-taper coupling configuration	76
5.9	Calculated coupling coefficient κ_2^2 and total cavity loss β_2^2	77
5.10	Calculated coupling coefficient κ_1^2, κ_2^2 and total cavity loss β_1^2, β_2^2	77
6.1	Illustration of the add/drop functions	83
6.2	Schematic of the microsphere channel add/drop device	85
6.3	Ideal configuration of an optical add/drop multiplexer (OADM)	85
6.4	Photograph of the top view of the microsphere and double-tapered fiber system	87
6.5	Transmission spectra measured simultaneously at both port 2 and port 3 for the add/drop device	87
6.6	BER experimental setup	90
6.7	BER performance of an add/drop filter using a 45 μm diameter microsphere	90
7.1	Energy level diagram of the erbium:ytterbium system	95
7.2	Image of a fiber taper coupled microsphere laser	98
7.3	Pump transmission spectrum of a fiber taper coupled microsphere laser	99
7.4	Pictures of green emission of the microsphere laser	99

7.5	Photoluminescence spectra of the microsphere	101
7.6	$L_{out} - L_{in}$ curve of the microsphere laser	102
7.7	Illustration of whispering gallery mode precession in an aspherical resonator	109
7.8	Color image of the green up-converted photoluminescence	112
7.9	Ring patterns as the pump wavelength varies taken by Apogee CCD camera	114
7.10	Pump ring pattern switches as the pump polarization state changes	115
7.11	Photoluminescence spectra of the 980 nm pumped microsphere	118
7.12	Bi-sphere experiment	121
7.13	Effective index of fiber modes in a standard 1550 nm single mode fiber	123
7.14	Schematic of hybrid fiber taper coupling to a microsphere laser	125
7.15	Magnified photograph of the hybrid taper-sphere coupling system	125
7.16	Pump band transmission spectrum of the hybrid-taper coupled microsphere laser	128
7.17	Hybrid Laser spectrum collected from the 1550 nm fiber end	128
7.18	Laser spectrum observed using a Fabry-Perot etalon	129
7.19	Measured, total output laser power versus absorbed pump power in the microsphere	129

Chapter 1

Introduction

The interaction of optical waves with small dielectric particles has been a subject of long-term interest. The early treatments pioneered by Lorenz, Mie, and Debye provide the framework for the description of various natural light scattering phenomena. In 1939, Richtmyer first proposed the employment of an axially symmetric dielectric object to create electromagnetic resonator with high quality factor (Q). The resonator modes strongly confined just within the inside surface by continuous total internal reflection are so called whispering gallery modes (WGMs). The unique properties of very high Q's and very small mode volumes simultaneously obtainable in a WGM resonator have attracted intensive attention since then.

Microwave resonators of this type have been thoroughly studied and successfully used in engineering. In the optical frequency domain, a number of research interests have been concentrated on both linear (e.g., Raman scattering, optical bi-stability, optical levitation, etc.) and nonlinear (e.g., lasing, stimulated

Raman scattering, intensity-dependent refractive index, etc.) applications. The microcavities take many forms, such as liquid droplets, aerosols, and solid-state spheres. More recently, Ilchenko et al. first shown that one could obtain very high quality factor in a pure silica microsphere. The record Q, as high as 10^{10} at 633 nm, reached the intrinsic absorption limit of fused silica. This made the silica glass microsphere an excellent candidate for cavity QED experiments, quantum nondemolition measurements, and frequency stabilization of lasers and nonlinear optics.

The coupling technique has also been evolved along with the study on microcavities. A straightforward method is to shine light onto the sphere directly, however, free space beams are not favored when coupling efficiency and/or high quality factors are concerned. A high-index prism coupler was first introduced by Gorodetsky et al. to provide evanescent coupling to the silica microsphere, where frustrated totally internal reflection occurred on the inner surface of the prism at the contact point with the resonator. In the mid 1990s, waveguide coupling technique, particularly, using an eroded, polished or tapered optical fiber, was proposed by several research groups. It has been shown that the coupling efficiency can be improved dramatically if the discrete guided modes are well matched to the sphere modes. The compatibility to optical fiber, as well as the ease of fabrication of such a miniature system, inspired many potential applications to modern telecommunication systems.

This thesis investigates the physics and applications of optical fiber taper-coupled microsphere resonators. In the first part, the physical principle of the

fiber taper to microsphere coupling is studied. We focus on the mode conversion in the tapered fibers and the mode matching between the taper and sphere modes, then demonstrate the ideal coupling, the critical coupling and controlled power transfer to high-Q silica microsphere by tuning the cavity loss. We also present symmetrical dual-taper coupling configuration, which enables light wave coupling between two tapers with extremely high efficiency. In the second part, a number of applications of the taper-sphere structure are explored. In particular, an all fiber-optic channel add/drop filter based on taper-resonator-taper (TRT) structure is demonstrated, and an optical fiber taper coupled 1.5 μm microsphere laser is developed.

Chapter 2 contains a general description of the whispering gallery modes in a dielectric spherical cavity. We will introduce a few definitions and conventions that are used in the rest part of the thesis.

Chapter 3 gives a brief review of microsphere coupling schemes. By comparison, we point out the advantages of using fiber taper couplers over other schemes. A simple model is presented to describe the basic mechanism of the waveguide to resonator coupling, and a symmetrical dual-taper coupling configuration is proposed. It is predicted that ideal coupling and full power transfer (critical coupling) to a high Q microsphere resonator are possible.

Chapter 4 introduces the fabrication procedures for the microspheres and tapered fibers. Experimental setup and measurement skills are also described.

Chapter 5 investigates the taper to sphere coupling experimentally. Results concerning the ideal coupling, the critical coupling, and high efficient power

transfer in a high Q silica microsphere are presented. Critical coupling to the resonator is demonstrated while the quality factor of the cavity remains as high as 10^7. Up to 99.8% power transfer into the microsphere is also observed.

Chapter 6 is devoted to the application of the symmetrical taper-resonator-taper coupling structure. An all fiber-optic passive device based on this structure is proposed as a channel add/drop filter. The characteristics of the device are studied and the bit-error-rate performance of the device is measured.

Chapter 7 demonstrates an active device application as a fiber taper-coupled microsphere laser. The pump wave and the laser are both collected by a single tapered fiber. Single frequency lasing is observed under optimized pump and laser coupling. A hybrid fiber taper is designed to improve pump coupling to the microsphere, and thus laser output power significantly.

The work presented in this thesis has appeared in the journal articles [1]-[6] and conference presentations [7]-[11] listed at the end of this chapter.

Bibliography

[1] M. Cai and K. Vahala, "High Efficient Microsphere Laser Coupled Using a Hybrid Fiber Taper," to be published in *Optics Letters*, vol.26, June 15, 2001.

[2] M. Cai, O. Painter, K. Vahala and P.C. Sercel, "Fiber-Coupled Microsphere Laser," *Optics Letters*, vol. 25, pp. 1430-1432, 2000.

[3] M. Cai, P. O. Hedekvist, A. Bhardwaj and K. Vahala, "5 Gbit/S BER Performance on an All Fiber-Optic Add/Drop Device Based on a Taper-Resonator-Taper Structure," *IEEE Photonics Technology Letters*, vol. 12, pp. 1177-1179, 2000.

[4] M. Cai, O. Painter, and K. Vahala, "Observation of Critical Coupling in a Fiber Taper to Silica-Microsphere Whispering Gallery Mode System," *Physics Review Letters*, vol. 85, pp. 74-77, 2000.

[5] M. Cai and K. Vahala, "Highly Efficient Optical Power Transfer to Whispering Gallery Modes Using a Symmetrical Dual-Coupling Configuration," *Optics Letters*, vol. 25, pp. 260-262, 2000.

[6] M. Cai, G. Hunziker, and K. Vahala, "Fiber-Optic Add-Drop Device Based on a Silica Microsphere-Whispering Gallery Mode System," *IEEE Photonics Technology Letters*, vol. 11, pp. 686-687, 1999.

[7] M. Cai, and K. Vahala, "Highly Efficient Hybrid Fiber Taper Coupled Microsphere Laser," *Conference on Laser and Electro-Optics,* Baltimore, Maryland, May 6-11, 2001, paper CTuD1 (Invited Paper).

[8] O. Painter, M. Cai, and K. Vahala, "Pigtailed Microsphere Resonators Having Q > 1 Million," *The Optoelectronics and Communications Conference*, Makuhari Messe, Chiba, Japan, July 11-14, 2000 (Invited Paper).

[9] M. Cai, K. Vahala and O. Painter, "Fiber Coupled High-Q Microsphere Resonators," *Diffractive Optics and Micro-Optics,* Quebec City, Canada, June 18-22, 2000, paper DWA1 (Invited Paper).

[10] K. Vahala and M. Cai, "Ultra-High Q Microsphere Resonators," *Conference on Laser and Electro-Optics*, San Francisco, California, May 7-12, 2000, paper CMN3 (Invited Paper).

[11] M. Cai, P. O. Hedekvist, K. Vahala, "5 Gbit/S Transmission Through An All-Fiber-Optic Add/Drop Device Based on a Microsphere Whispering-Gallery-Resonance System," *Optical Fiber Communication Conference*, Baltimore, Maryland, March 5-10, 2000, paper WN12.

Chapter 2

Whispering Gallery Modes in Dielectric Microspheres

2.1. Introduction

The first observation of an axially symmetrical dielectric cavity functioned as an electromagnetic resonator dates back to Richtmyer [1]. The resonance modes, so-called whispering gallery modes (WGMs), derive their name from the acoustical analogue, which was first described by Rayleigh. A physical interpretation of the resonator is that the electromagnetic wave is trapped by continuous totally internal reflection as it propagates around the circling orbits just inside the surface of the cavity and that after circumnavigating the sphere the wave returns to its starting point in phase. Hence, it takes long time for the energy of a mode to leak out of the sphere, and very large energy densities can

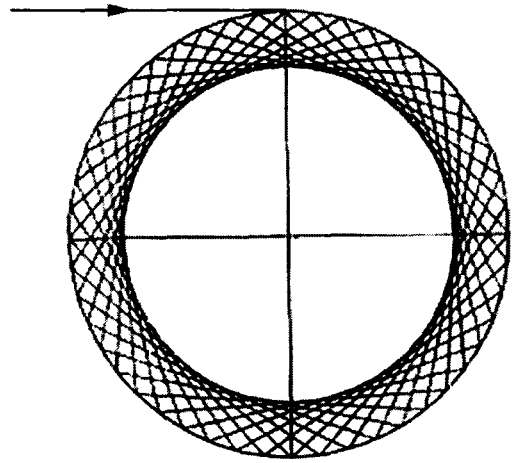

Figure 2.1 Ray path of a tangentially incident ray that makes a number of internal reflections before leaving the cavity in the backscattered direction, adapted from Ref. [2].

accumulate in the resonant modes. Fig. 2.1 is an illustration of a closed orbit of light tangentially incident to a cylindrical cavity in the view of ray optics [2].

Early treatment of optical behavior in small particles in the context of wave optics is described by Mie scattering theory [3], which consists of a rigorous solution of Maxwell's equation for scattering and absorption of electromagnetic waves by a dielectric sphere. More recently, however, intensive studies have been focused on the properties and applications of highly confined whispering gallery modes inside the cavities. Therefore, a straightforward approach based on classical electromagnetic solutions to describe the internal field distribution of the resonant modes is of primary interest.

In the remainder of this chapter, the mathematical solutions of the vector wave equation in a homogeneous dielectric sphere are reviewed (*solutions in a* cylindrical cavity can be obtained accordingly). The eigen frequencies and the

asymptotic formulas are derived. General features of whispering gallery modes and conventional definitions used in the rest of the thesis are discussed.

2.2. Electromagnetic Fields in a Spherical Coordinate System

We start with a homogenous, linear, isotropic media. The vector wave equation in spherical coordinates (r,θ,ϕ) can be expressed as

$$\nabla^2\Psi(r,\theta,\phi;t)-\frac{1}{\upsilon^2}\frac{\partial^2\Psi(r,\theta,\phi;t)}{\partial t^2}=0, \tag{2.1}$$

where $\Psi(r,\theta,\phi;t)$ represents either the electrical field $\vec{E}(r,\theta,\phi;t)$ or the magnetic field $\vec{H}(r,\theta,\phi;t)$ and υ is the light speed in the medium. Assume simple harmonic time dependence, $\Psi(r,\theta,\phi;t)$ can be written as $\psi(r,\theta,\phi)e^{-i\omega t}$, where $\psi(r,\theta,\phi)=\hat{r}\psi_r(r,\theta,\phi)+\hat{\theta}\psi_\theta(r,\theta,\phi)+\hat{\phi}\psi_\phi(r,\theta,\phi)$ is a function of the space variables alone, and satisfies the vector Helmholtz equation

$$\nabla^2\psi(r,\theta,\phi)+n^2k^2\psi(r,\theta,\phi)=0, \tag{2.2}$$

where $k=\omega/c$ is the wave vector in the vacuum and n is the refractive index of the medium.

Eq. (2.2) can be solved explicitly (see, for example, Ref. 4). The vector field distribution is expressed via Debye potentials $\Pi(r,\theta,\phi)=z_l(knr)Y_l^m(\theta,\phi)$, which are solutions of the scalar wave equation $\nabla^2\Pi(r,\theta,\phi)+n^2k^2\Pi(r,\theta,\phi)=0$. Here $z_l(knr)$ is the spherical Bessel function that may be specified as $j_l(knr)$, $n_l(knr)$

or $h_l(knr)$ depending on the boundary conditions, and $Y_l^m(\theta,\phi)$ is the spherical Harmonics of order l, m, with l a positive integer and $m = l, l-1, \ldots -l$.

We decompose the spherical waves into TM and TE modes in respect to the transverse direction to $\hat{r}$. The fields are given by

$$\text{TE modes} \qquad \vec{E} = ik\nabla \times \vec{r}\Pi \qquad \vec{H} = \sqrt{\frac{\varepsilon_0}{\mu_0}}\nabla \times \nabla \times \vec{r}\Pi_l^m$$

$$\text{TM modes} \qquad \vec{E} = \nabla \times \nabla \times \vec{r}\Pi \qquad \vec{H} = ik\sqrt{\frac{\varepsilon_0}{\mu_0}}\nabla \times \vec{r}\Pi$$

Explicitly, the components for TE modes are

$$\begin{aligned}
E_r &= 0, & H_r &= \sqrt{\frac{\varepsilon_0}{\mu_0}}\frac{l(l+1)}{r} z_l(knr) Y_l^m(\theta,\phi) \\
E_\theta &= -\frac{knm}{\sin\theta} z_l(knr) Y_l^m(\theta,\phi), & H_\theta &= \sqrt{\frac{\varepsilon_0}{\mu_0}}\frac{1}{r}\frac{d}{dr}[rz_l(knr)]\frac{\partial}{\partial\theta}[Y_l^m(\theta,\phi)] \\
E_\phi &= -iknz_l(knr)\frac{\partial}{\partial\theta}[Y_l^m(\theta,\phi)], & H_\phi &= \sqrt{\frac{\varepsilon_0}{\mu_0}}\frac{im}{r\sin\theta}\frac{d}{dr}[rz_l(knr)]Y_l^m(\theta,\phi)
\end{aligned} \tag{2.3}$$

and, independently, for TM modes,

$$\begin{aligned}
E_r &= \frac{l(l+1)}{r} z_l(knr) Y_l^m(\theta,\phi), & H_r &= 0 \\
E_\theta &= \frac{1}{r}\frac{d}{dr}[rz_l(knr)]\frac{\partial}{\partial\theta}[Y_l^m(\theta,\phi)], & H_\theta &= \sqrt{\frac{\varepsilon_0}{\mu_0}}\frac{knm}{\sin\theta} z_l(knr) Y_l^m(\theta,\phi) \\
E_\phi &= \frac{im}{r\sin\theta}\frac{d}{dr}[rz_l(knr)]Y_l^m(\theta,\phi), & H_\phi &= ikn\sqrt{\frac{\varepsilon_0}{\mu_0}} z_l(knr)\frac{\partial}{\partial\theta}[Y_l^m(\theta,\phi)]
\end{aligned} \tag{2.4}$$

2.3. Whispering Gallery Modes in Microspheres

2.3.1 Resonant Mode Distribution in Microspheres

Now let's consider a dielectric sphere with refractive index n_s and radius R, located at the center of the spherical coordinates. The resonant fields can be written down immediately in terms of the particular choice of spherical Bessel functions, which satisfie the appropriate boundary conditions. Within the sphere, the exact radial solutions are the spherical Bessel functions $j_l(kn_s r)$, while outside the sphere they are the second order of spherical Hankel functions $h_l^{(2)}(kn_0 r)$, which represent an outgoing tunneling wave, growing unbounded in the radial direction far from the sphere. Very close to the surface, however, the fields decay exponentially in the radial direction. Since only the near field, the bound portion of the field, contributes to the coupling with the external excitations, the radial dependence of the resonant modes can be written as [5]

$$\begin{cases} j_l(kn_s r) & \text{r} < \text{R} \\ j_l(kn_s R)\exp[-\alpha_s(r-R)] & \text{r} \geq \text{R}, \end{cases} \tag{2.5}$$

where α_s is a decay parameter associated with particular resonant mode.

In the limit of the sphere radius R large compared with the wavelength of the modes λ, the electric fields are approximately polarized in radial and polar direction [4]. Within the sphere boundary, the fields can be simplified as

$$\begin{cases} E_\theta(r,\theta,\phi) \sim -\dfrac{kn_s m}{\sin\theta} j_l(kn_s r) Y_l^m(\theta,\phi) & \text{TE modes} \\ E_r(r,\theta,\phi) \sim \dfrac{l(l+1)}{r} j_l(kn_s r) Y_l^m(\theta,\phi) & \text{TM modes.} \end{cases} \tag{2.6}$$

2.3.2 Identification of Whispering Gallery Modes

As solutions of a three-dimensional boundary-value problem, the whispering gallery modes are characterized by four indices (p, n, l, m), where p denotes TE or TM polarizations; n, the radial order number, denotes the number of maxima of the Bessel function $j_l(kn_s r)$ inside the sphere; l, the mode number, approximately equals to the number of wavelengths packed along the circumference of the sphere ($l \approx 2\pi n_s R/\lambda$); m is the number of field maxima in the equatorial plane ($\theta = 0$, measured from the equatorial plane). Note that $l - m + 1$ is the number of extrema of the associated Legendre function $P_l^m(\cos\theta)$ ($Y_l^m(\cos\theta) = P_l^m(\cos\theta)e^{im\phi}$) in the plane $\phi = const.$

The visualization in the concepts of integrated optics [5] or classical precession [6-7] is very helpful to understand the propagation of the whispering gallery modes in a sphere. In the view of integrated optics, a mode can be thought of as tracing out a "zigzag" path around the surface of the sphere with the equatorial plane being the mean plane of propagation, as shown in Fig. 2.2. The mode is confined to a belt around the equatorial plane by the curvature of the sphere in the polar direction. Parallel to the surface, in the direction of the zigzag path, the mode has a propagation constant β_l ($= \sqrt{l(l+1)}/R$), the projection of β_l onto the equator β_m ($= m/R$) is commonly referred to as the "propagation constant", because it is the wave vector in the net direction of propagation. For any fixed value of l, m can range throughout $|m| \le l$. Different values of m imply that the modes travel in zigzag paths with different inclinations with respect to the

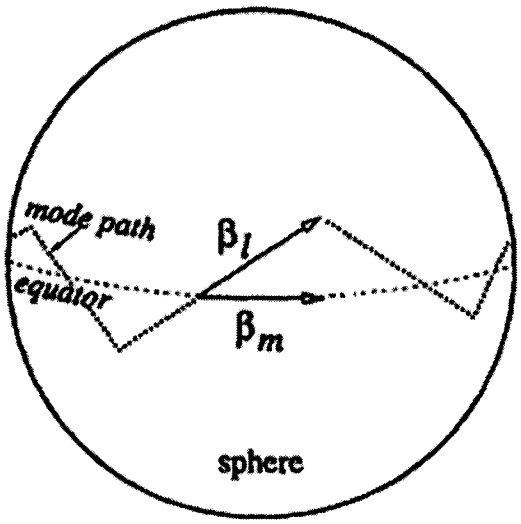

Figure 2.2 Schematic of the mode propagation constants along the surface of a sphere. Adapted from Ref. [5].

equatorial plane. It is so-called the fundamental mode when $m = l$ (particularly, for $n = 1$), which has the smallest inclination, with a value of approximately $1/\sqrt{l}$ radians. Although modes with decreasing values of m propagate at larger inclinations, for the same value of l they all have the same resonant wavelength. This is because modes that take larger excursions away from the equator need to propagate over shorter distances to complete a revolution around the sphere (from the fact that higher latitude circles have less circumference than the equator). In fact, modes with the same l and n values, but arbitrary m, are simply collections of identical fundamental $m = l$ modes that propagate along different great circles, with different inclinations and different phase references. They must have the same resonant wavelength, regardless of m. This is to be shown mathematically in the next section.

The whispering gallery modes can be also interpreted as precessing circular fundamental modes with the precessing rate depending on the value of the resonator nonsphericity. In Chapter 7, we will discuss this in detail and use it to explain the pump ring modes in heavily doped microspheres.

2.3.3 Characteristic Equations of Whispering Gallery Modes

The whispering gallery modes correspond to solutions of the characteristic equations of the electromagnetic fields in the presence of a sphere. The characteristic equations are obtained by expanding the fields in vector spherical harmonics and then matching the tangential components of the electric and magnetic fields at the surface of the sphere:

$$\begin{cases} n_s \dfrac{[n_s x j_l(n_s x)]'}{n_s x j_l(n_s x)} - \dfrac{[x h_l^{(2)}(x)]'}{x h_l^{(2)}(x)} = 0 & \text{TE modes} \\ \dfrac{[n_s x j_l(n_s x)]'}{n_s x j_l(n_s x)} - n_s \dfrac{[x h_l^{(2)}(x)]'}{x h_l^{(2)}(x)} = 0 & \text{TM modes,} \end{cases} \tag{2.7}$$

where $x = 2\pi R/\lambda = kR$ is the size parameter. For each choice of l, the roots of Eqs. (2.7) give a discrete set of resonant wave number $k_{n,l}$ (or angular resonance frequency $\omega_{n,l}$). Note that the resonance frequencies depend on n and l only, which is consistent with the physical interpretation in the last section.

It has been shown [8] that, if $R >> \lambda$ and the radial order number n is small ($n \sim 1$), the resonance frequencies can be accurately computed by an asymptotic expansion in powers of $\nu^{-1/3}$, where $\nu = l + 1/2$. The resonance size parameters

$x_{n,l}$, which are related to the angular resonance frequencies by $\omega_{n,l} = n_s x_{n,l} c/R$, are given by the asymptotic series

$$n_s x_{n,l} = \nu - \zeta_l \left(\frac{\nu}{2}\right)^{1/3} + \sum_{k=0}^{k_{max}} \frac{n_s d_k(n_s, \zeta_l)}{\nu^{k/3}(n_s^2 - 1)^{(k+1)/2}}. \tag{2.8}$$

Here ζ_l denotes the *lth* zero of the Airy function. The coefficients d_k depend on the polarization (TM or TE) of the mode and are given in the reference 8.

2.3.4 Quality Factors of Microsphere Resonators

Quality factor is a very important parameter that provides a convenient measure of confinement time of the light in a cavity. It is defined as

$$Q = \frac{2\pi \text{ Stored energy}}{\text{Enery lost per cycle}} \tag{2.9}$$

or

$$Q = \frac{-\omega W}{\text{dW/dt}}, \tag{2.10}$$

where W is the time-average stored energy, ω is the angular resonance frequency, and the energy lost per cycle is the power loss $(-dW/dt)$ times the period $(1/f)$. Solving for the stored energy as a function of time gives

$$W(t) = W_0 \exp(-\omega t/Q). \tag{2.11}$$

The average lifetime of a photon in the resonant mode is Q/ω.

The actual Q of a resonator is determined by radiative losses and by losses or gain attributable to absorption or emission by the materials of the cavity. It is

convenient to define the Q attributable to external, or radiative losses (i.e., the Q of a resonator having no absorption or emission) as Q_{ext}, and the Q attributable to internal loss or gain as Q_0. The total Q of the cavity is given by

$$\frac{1}{Q} = \frac{1}{Q_{ext}} + \frac{1}{Q_0}. \tag{2.12}$$

In this thesis, the Q refers to the external Q unless otherwise noted.

The electric field in the cavity varies as

$$E(t) = E_0 \exp(i\omega t - \frac{\omega}{2Q} t). \tag{2.13}$$

Near a resonance frequency ω_0, the distribution of the energy in the cavity, $|E(\omega)|^2$ is proportional to

$$\frac{1}{(\omega - \omega_0)^2 + (\omega_0/2Q)^2}. \tag{2.14}$$

The resonance has a Lorentzian lineshape. The width between the two points at which the energy is half of its maximum value is

$$\Delta\omega = \frac{\omega_0}{Q}. \tag{2.15}$$

In a fused silica microsphere, it was observed that the quality factor could approach 10^{10} at 633 nm, which corresponds to a photon lifetime of about 3 μs. In this thesis, we are dealing with microspheres in the 1550 nm band whose quality factors are in the range from 10^4 to 10^8, corresponding to resonance linewidths from 1 MHz to a few GHz.

2.4. Pictures of Whispering Gallery Modes

To conclude this chapter, we show a few pictures and plots that visualize the whispering gallery modes in a microsphere. Fig. 2.3 is a FDTD numerical simulation of the electric field intensity distribution of a fundamental TE mode ($n = 1, m = l = 20$) from different view angles. Fig. 2.4 (a) and (b) show the radial dependence and the polar dependence of the electrical field intensity distribution, respectively. With Eq. 2.8, the calculated resonant frequencies for both TE and TM whispering gallery modes within the 1550 nm band are shown in Fig. 2.5.

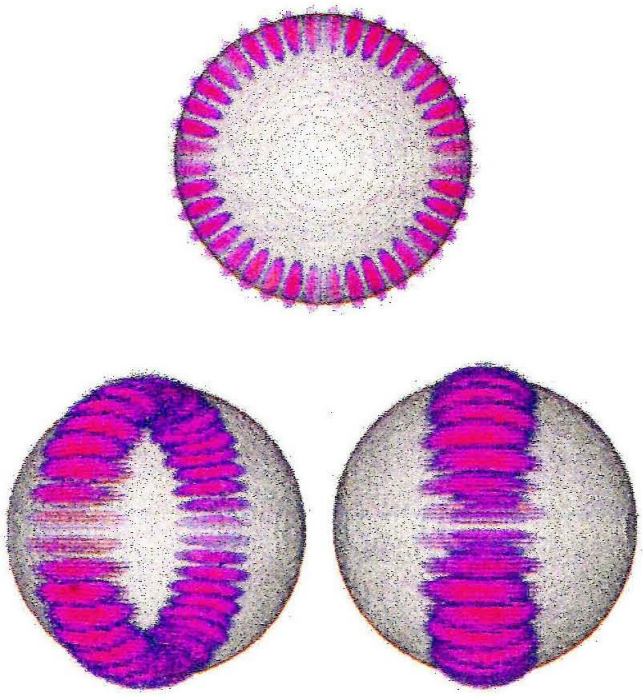

Figure 2.3 Numerical simulation of the electric field distribution for a fundamental mode in a microsphere. The mode is TE polarized with $n = 1, m = l = 20$. Showed at different view angles.

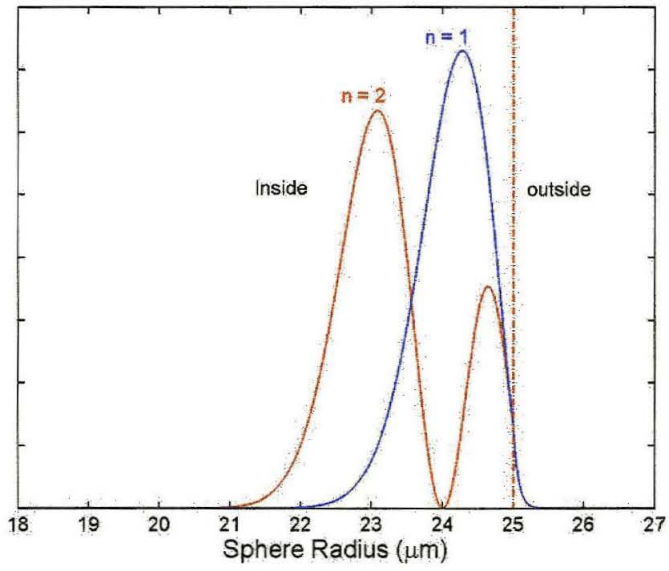

(a)

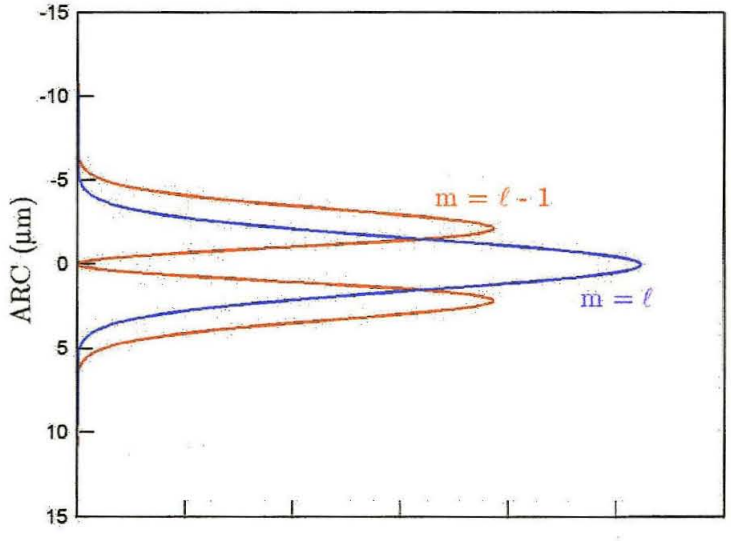

(b)

Figure 2.4 In a sphere having radius of 25 μm, the field intensity distribution (a) in the radial direction for $n = 1$ and 2 (with the same l) and (b) in the polar direction for $m = l$ and $l - 1$ (with the same n), respectively.

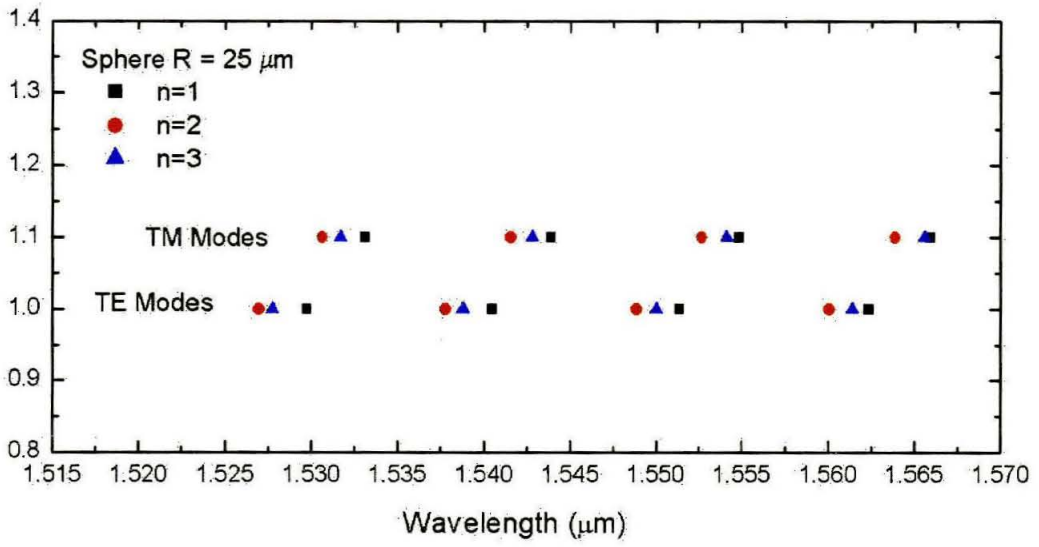

Figure 2.5 For a sphere of $R = 25\ \mu m$, calculated resonant frequencies of TE and TM whispering gallery modes in the 1550 nm band.

Bibliography

[1] R. D. Richtmyer, "Dielectric Resonators," *Journal of Applied Physics*, vol. 10, pp. 391-398, 1939.

[2] V. Khare and H. M. Nussenzveig, "Theory of the Glory," *Physics Review Letters*, vol. 38, pp. 1279-1282, 1977.

[3] G. Mie, "Beitrage Zur Optik Truber Medien Speziell Kolloidaler Metallosungen," *Annual Physics*, vol 25, pp. 377-455, 1908.

[4] W. K. H. Panofsky and M. Phillips, "Classical Electricity and Magnetism," Chapter 13, Addison-Wesley Publishing Company, 1962.

[5] B. E. Little, J.P. Laine and H. A. Haus, "Analytic Theory of Coupling from Tapered Fibers and Half-Blocks into Microsphere Resonators," *Journal of Lightwave Technology*, vol. 17, pp. 704-715, 1999.

[6] J. C. Swindal, D. H. Leach, and R. K. Chang, "Precession of Morphology-Dependent Resonances in Nonspherical Droplets," *Optics Letters*, vol. 18, pp. 191-193, 1993.

[7] M. L. Gorodetsky, V. S. Ilchenko, "High-Q Optical Whispering Gallery Microresonators: Precession Approach for Spherical Mode Analysis and Emission Patterns with Prism Couplers," *Optics Communications*, vol. 112, pp. 133-143, 1994.

[8] S. Schiller, "Asymptotic Expansion of Morphological Resonance Frequencies in Mie Scattering," *Applied Optics*, vol. 32. pp. 2181-2183, 1993.

[9] M. L. Gorodetsky, A. A. Savchenkov, and V. S. Ilchenko, "Ultimate Q of Optical Microsphere Resonators," *Optics Letters*, vol. 21, pp 453-455, 1996.

Chapter 3

Tapered Optical Fiber to Microsphere Coupling

3.1 Introduction

As we have shown in Chapter 2, a fused silica microsphere can support whispering gallery modes with extremely high quality factors up to 10^{10} [1]. Modes of this type possess negligible electrodynamically defined radiative losses, and are not efficiently accessible by illumination from free-space beams. Near-field evanescent wave couplers are required to provide efficient coupling without disturbing the high-Q characteristics.

A high-index prism with frustrated totally internal reflection is one of such couplers that has been widely used since Ilchenko et al. first demonstrated in 1989 [2]. As shown in Fig. 3.1, a Gaussian beam is focused on the inner surface of

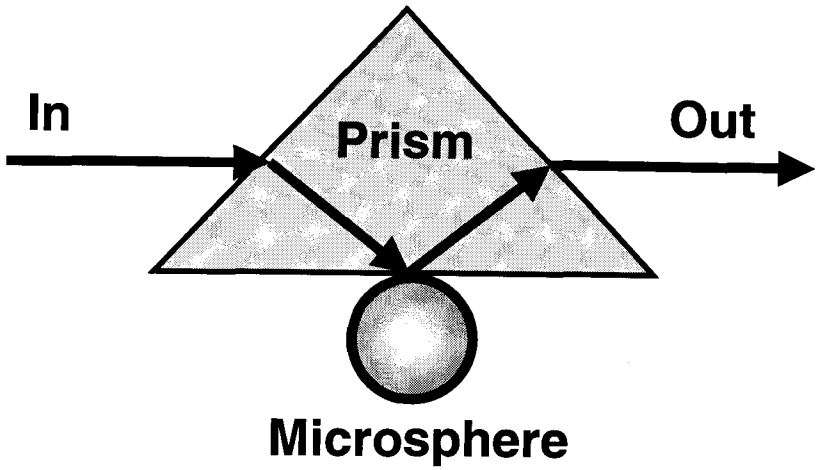

Figure 3.1 Schematic of a high index prism coupling to a microsphere.

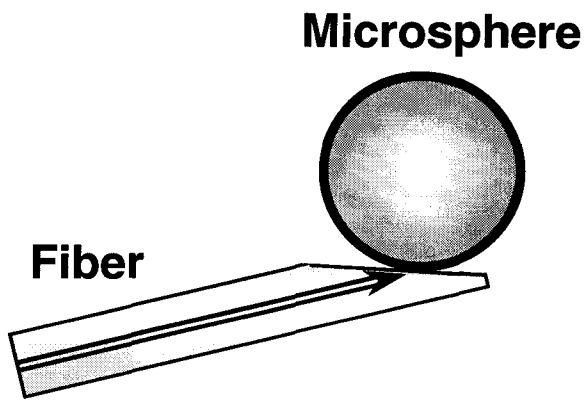

Figure 3.2 Modified prism coupler using an angle-polished optical fiber.

a prism at the contact zone with a microsphere under certain optimal angle. The microsphere is placed at a distance of $(0.1 \sim 1)\lambda$ from the surface in the area of the focal spot. The effective coupling of the beam into whispering gallery modes was reported up to 80% absorption of the incident beam power in fused silica microspheres. The prism coupler, although flexible, is bulky. A modified prism coupler based on an angle-polished optical fiber was proposed *recently [3]*. As

illustrated in Fig. 3.2, the tip of an optical fiber is polished with a steep angle. Incident light is guided through the fiber to the polished surface and undergoes totally internal reflection. The best coupling efficiency reported so far was about 60%. The angle-polished fiber coupler is essentially equivalent to a prism coupler. Both of them require sophisticated alignment for the coupler and the resonator to achieve phase matching to a particular resonant mode.

It is always desirable to couple whispering gallery modes into optical fibers for the purpose of easy measurement and potential device applications. Recently, a broad range of efforts has been led by several research groups, including our own [4-7]. In 1995, Griffel et al. and Dubreuil et al. proposed the use of a side-polished half-block fiber coupler [4] and an eroded single mode fiber [5], respectively. As shown in Fig. 3.3, both methods try to remove the fiber cladding so that the evanescent field of the propagating mode in the core is exposed and can be used for whispering gallery mode excitation. The transverse dimension of the guided mode in a single mode fiber is typically 3-5 μm for visible or near-infrared wavelengths. As a result, the phase matching between the guided fiber mode and the whispering gallery modes is good only in the limit of large spheres. The coupling efficiency was about 20% in a sphere of diameter 1 mm [8], while much less in smaller spheres.

In 1997, by replacing the D-shaped fiber coupler with an adiabatically tapered fiber, Knight et al [6] observed up to 72% absorption of the incident light by a microsphere. In this method, the optical fiber is tapered down to a certain size,

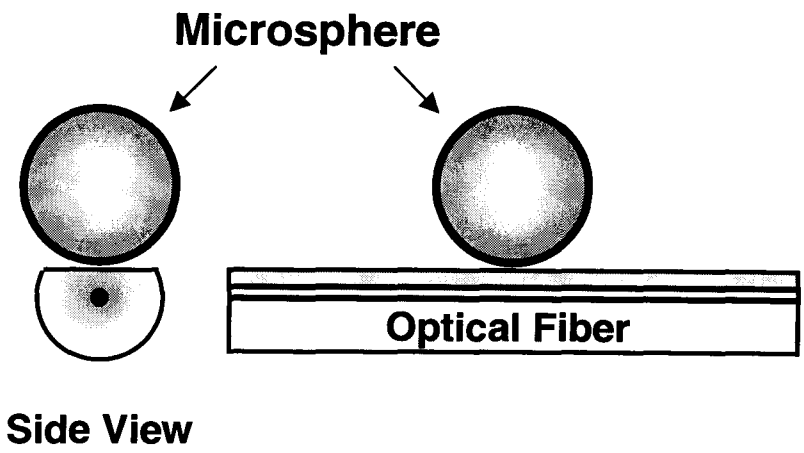

Figure 3.3 Polished or eroded optical fiber coupler.

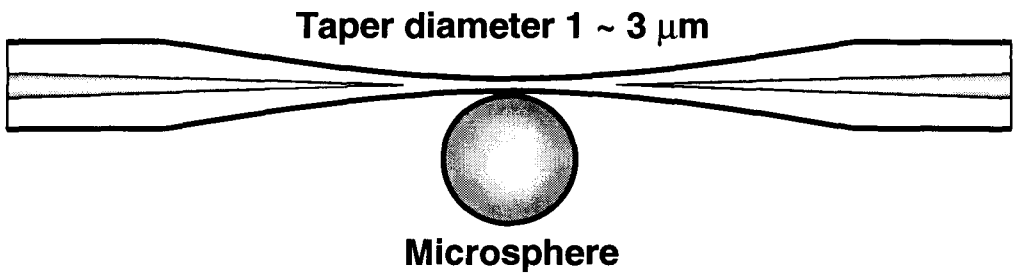

Figure 3.4 Tapered optical fiber coupler.

typically about $1 \sim 3\ \mu m$ in diameter, to achieve the ideal phase matching with a particular whispering gallery mode. Fig. 3.4 shows a schematic of the taper to microsphere coupling.

The Vahala research group has further developed the tapered fiber coupling technique. Coupling efficiency of up to 99.8% was measured in a taper-resonator-taper (TRT) structure [9], which employed two nearly identical fiber taper couplers. Critical coupling (100% power transfer into the sphere) was investigated

using a carefully designed experimental setup [10]. Furthermore, the taper loss for the nonresonant modes can be as small as 0.1 dB [11], which is very attractive for practical applications.

The rest of this chapter is devoted to the theoretical description of the taper modes and a fundamental model of the taper to microsphere coupling. The critical coupling condition is thus derived from the model, and possible ways to maximize the power transfer are also pointed out.

3.2 Modes in Tapered Fiber Couplers

As shown in Fig. 3.4, a section of tapered single mode fiber is virtually a symmetrical waveguide with varying transverse dimension. Such a waveguide is usually made by heating and stretching a portion of a fiber along the opposite axial directions. The fiber cladding and core reduce their sizes simultaneously and proportionally. Pulling is halted when a desired cladding size (usually less than $5\ \mu m$ in diameter) is obtained. In the taper waist region, the fiber core is no longer significant (because the size of the core is much less than the wavelength of the light) and the taper is actually a cylindrical silica waveguide surrounded by air.

There are two issues of interest. One is the characteristics of the air-cladding modes that interact directly with the sphere modes in the taper waist region. The other is the propagation of the light along the tapered fiber, which is crucial to

understanding the taper loss and the modes excited in the taper region. We will address these two problems in the rest of this section.

3.2.1 Charcteristics of Taper Modes

The wave equations have exact solutions for both the step-index optical fiber (which is most widely used nowadays) and the air-cladding cylindrical waveguide (which is just a special case of the step-index fiber). The complete mode description can be found in many references (see, for example, Ref. [12] and [13]).

For a step-index cylindrical waveguide, the propagation constant of the existing modes β is given by a transcendental function [13]:

$$\left(\frac{J_l'(ha)}{haJ_l(ha)}+\frac{K_l'(qa)}{qaK_l(qa)}\right)\left(\frac{n_1^2 J_l'(ha)}{haJ_l(ha)}+\frac{n_2^2 K_l'(qa)}{qaK_l(qa)}\right)=l^2\left[\frac{1}{(qa)^2}+\frac{1}{(ha)^2}\right]^2\left(\frac{\beta}{k_0}\right)^2$$

$$q^2=\beta^2-n_2^2k_0^2$$
$$h^2=n_1^2k_0^2-\beta^2$$
$$k_0=\frac{\omega}{c}, \tag{3.1}$$

where k_0 denotes the propagation constant in the vacuum, a is the core radius, n_1 and n_2 are refractive indices of the core and cladding media, respectively. J_l and K_l represent the modified Bessel functions of the first and second kind, respectively, and order l is a nonnegative integer.

It is well known that in the limit of $n_1-n_2<<1$, the hybrid modes (EH_{lm}, HE_{lm}) can be approximated as linearly polarized modes (LP_{lm}). In fact, the propagating constants of the exact $HE_{l+1,m}$ and $EH_{l-1,m}$ modes become the

same in the limit of $n_1 \to n_2$. The conventional labels for LP modes and their corresponding HE/EH modes are

$$\begin{aligned} LP_{01} &\to HE_{11} \\ LP_{11} &\to HE_{21}, TE_{01}, TM_{01} \\ LP_{21} &\to HE_{31}, EH_{11} \\ LP_{02} &\to HE_{12} \\ LP_{31} &\to HE_{41}, EH_{21} \\ LP_{12} &\to HE_{22}, TE_{02}, TM_{02} \\ &\cdots \end{aligned} \tag{3.2}$$

Define the effective mode index

$$n = \frac{\beta}{k_0}. \tag{3.3}$$

Fig. 3.5 shows n for a number of the low-order modes as a function of the core diameter $2a$ in an optical fiber, which has a numerical aperture of 0.11 and a core index of 1.46. The wavelength is at 1550 nm. The core refractive index is thus only slightly higher than that of the cladding medium by 0.04.

For a standard 1550 nm single mode fiber, the core diameter is about $9 \sim 10\ \mu m$, which ensures that only LP_{01}, the fundamental mode, can propagate along the fiber.

Now let's consider a tapered single mode fiber. Assume that the variation in taper diameter at the taper-sphere interaction area (usually $\sim 10\lambda$) is negligible (this assumption is justified for a gradually pulled fiber taper, and has been verified by precise measurement of the taper profiles), the taper waist region is just a special case of the step-index optical fiber with the cladding refractive index $n_2 = 1$. By contrast, a plot of the normalized propagation constant as a

function of taper diameter at the taper waist region is shown in Fig. 3.6, where the condition $n_1 - n_2 << 1$ doesn't hold, and the modes are labeled with their original HE/EH notations. The HE_{11} mode is the taper fundamental mode. Different from the single mode fiber, however, the taper is generally a multimode waveguide. A taper with a diameter of 3 μm can support as many as 12 modes. To achieve efficient coupling from the taper to the microsphere, it is very important to phase match the taper modes to the spherical whispering gallery modes. In other words, the propagation constants for both modes have to be chosen to be equal to each other. Figure 3.7 shows the results of the phase matching calculation. The solid lines are adapted directly from of Fig. 3.6, but on a smaller scale, and the dotted lines are effective refractive indices at 1550 nm for first few radial mode numbers of TE-polarized whispering gallery modes as a function of sphere diameter, plotted on the top axis. The top and bottom scales in the plot have been chosen to match approximately the effective refractive index for a given taper size with that of the lowest radial order number $(n = 1)$ mode in a particular size of sphere. In the case shown in the Fig. 3.7, the phase matching is achieved for the fundamental TE mode in a 50 μm diameter sphere when coupled by a 1.87 μm diameter taper.

Note that, besides the perfect phase matching between the fundamental taper mode and the fundamental sphere mode, other close matches still exist. For example, as shown in Fig. 3.7, the effective refractive indices for $n = 3$ sphere modes are very close to those of TE_{01} taper modes. This is, however, not desirable if it is required to excite a particular whispering gallery mode in the

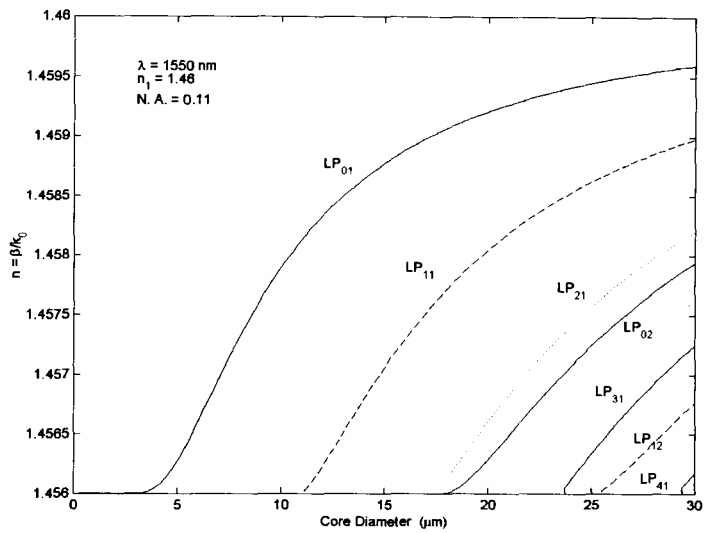

Figure 3.5 Effective mode index (normalized propagation constant) as a function of the core diameter of an optical fiber at 1550 nm. The refractive index of the fiber core is 1.46 and numerical aperture is 0.11, corresponding to $n_1 - n_2 = 0.004$.

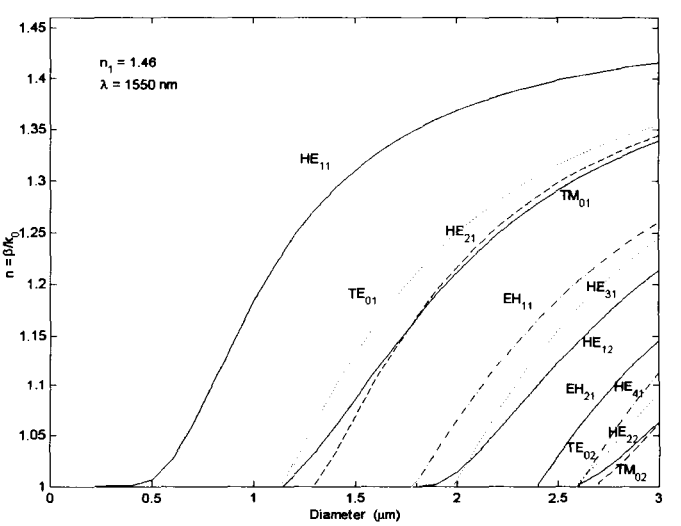

Figure 3.6 Effective mode index as a function of taper diameter at 1550 nm. The refractive index of the taper is 1.46.

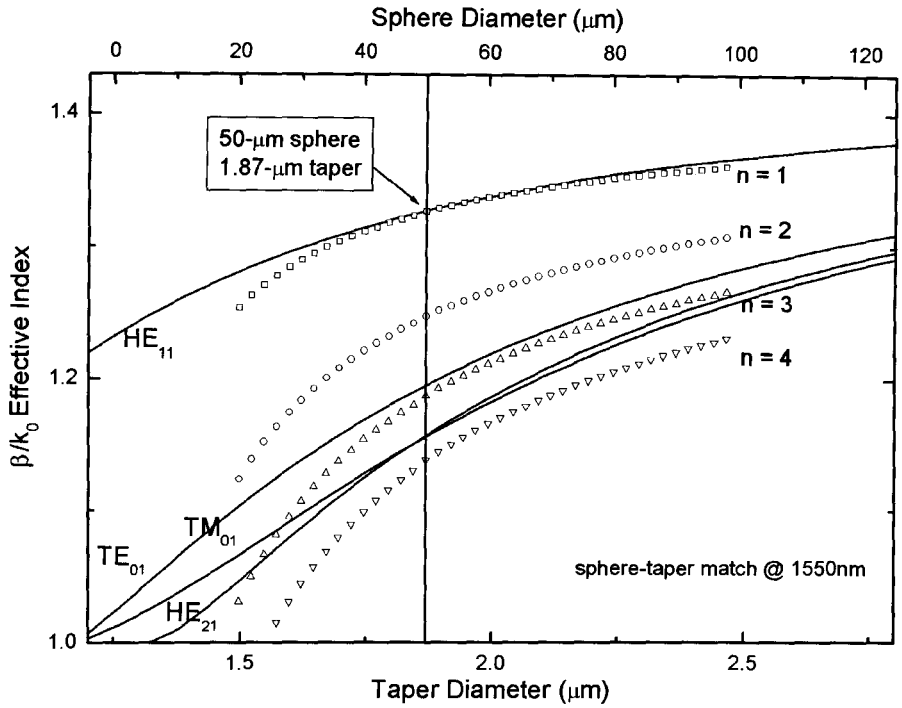

Figure 3.7 Calculated effective mode index for a tapered fiber (solid curves) as a function of the radius (plotted on the bottom axis) and for the first few radial mode numbers of whispering gallery mode resonances for spheres of different sizes, plotted on the top axis. The bulk material refractive indices for both the taper and sphere are 1.46, and the wavelength is at 1550 nm.

microsphere. To eliminate the undesirable high-order taper modes coupling to the sphere modes, the taper transition profile is of the key. In the next section, we will study the mode propagation in the tapered fibers and give the guidelines for optimal taper fabrication.

3.2.2 Propagation Along Tapered Fibers

Tapered optical fibers were first suggested in applications as bidirectional fiber couplers and fiber polarizers in the early 1980s. Mode field evolution in a tapered fiber has been thoroughly studied since then. A number of references can be found in literatures [13-19], plus the references therein. Under the assumption that the taper transition is sufficiently slow (it is practically true in our experiments where gradual pulling procedure ensures minimal taper loss.), local mode theory [13, 18] provides a simple analytical description of field propagation along the taper and enables simple physical criteria to be applied to the coupling loss mechanism.

The local mode theory states that the field and the propagation constant in an approximately adiabatic taper of a single mode fiber can be described accurately by that of local fundamental mode, which conserves power as it propagates and is the solution to the wave equations with the geometry of the local cross-section. A taper is approximately adiabatic if the taper angle is small enough everywhere to ensure that there is negligible power loss from the fundamental mode as it propagates along the length of the taper.

The adiabatic criterion (also called slowness criterion) is derived from the physical argument that the local taper length-scale must be larger than the coupling length between the fundamental mode and the dominant coupling mode for power loss to be small. Accordingly, we define the local taper length-scale z_t as the height of a right circular cone with a base coincident with the local core

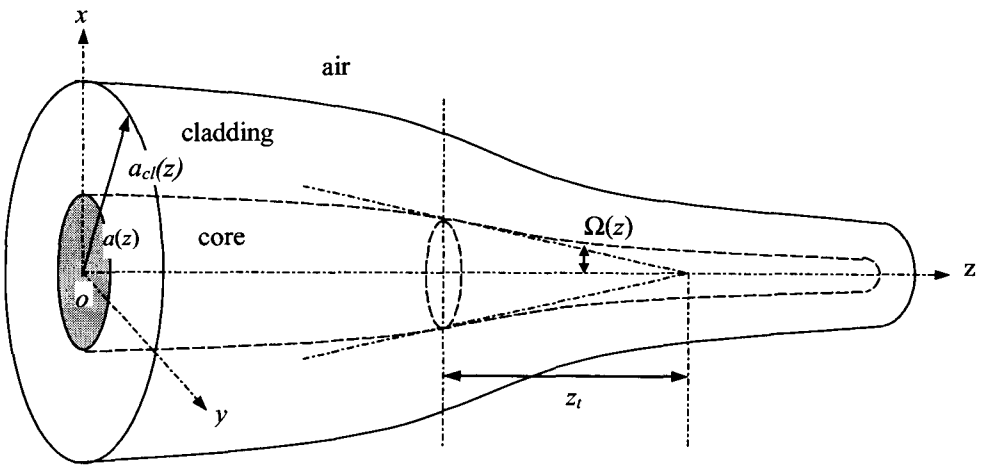

Figure 3.8 Illustration of a gradually tapered optical fiber. Adapted from Ref. [18].

cross-section and apex angle equal to the local taper angle $\Omega(z) = \tan^{-1}|da/dz|$, as illustrated in Fig. 3.8, where z is the distance along the taper, and $a = a(z)$ is the local core radius. The local coupling length between the two modes is taken to be the beat length $z_b = z_b(z)$, between the fundamental and second higher order local modes, where $z_b = 2\pi/(\beta_1 - \beta_2)$, and β_1, β_2 are the respective propagation constants. The condition $z_t = z_b$ therefore gives the adiabaticity criterion and can be re-written as

$$\Omega = \frac{a(\beta_1 - \beta_2)}{2\pi}, \tag{3.4}$$

where the approximation $z_t \approx a/\Omega$ is applied considering that $\Omega(z) << 1$ in the practical case.

As for an axisymmetric taper, the fundamental LP_{01} local mode can only couple to modes with the same azimuthal symmetry, i.e. to the higher order modes LP_{0m}, and coupling will be predominantly to the higher order mode with a propagation constant closest to that of the fundamental mode, i.e., to LP_{02} mode.

If the taper is bent, however, the coupling will be predominantly to any mode with the nearest propagation constant to the fundamental mode, i.e., to LP_{11} mode. The adiabaticity criterion therefore leads the theoretical limitation for a lossless taper. If the taper is pulled slowly, such that the local taper angle Ω is far less than the right side of Eq. (3.4), there is no power transfer between local modes, and the power of the fundamental local mode is conserved along the taper. In other words, only the HE_{11} mode exists in the taper waist region, and the taper loss is negligible. We will show later that tapers fabricated in our experiments fall far into this region.

3.3 Modeling of Taper to Microsphere Coupling

Now we have derived the exact mathematical expressions of the whispering gallery modes in a dielectric sphere (Chapter 2) and the taper modes in an adiabatically tapered fiber (Chapter 3). Coupling from the taper to the microsphere can be described by several analytical or numerical methods, such as the coupled mode theory [20], the finite-element beam propagation method (BPM), and the Finite-Difference Time Domain (FDTD) method, etc. Each of these methods is appropriate and accurate for a different set of problems and handles complicated mathematical formula or numerical solutions. The physical essence of the coupling from a waveguide to a resonant cavity, however, is hidden within these numerical calculations. In this section, we develop a simple but fundamental model for a two-dimensional system that consists of a straight

waveguide coupler and a disk resonator. This model unveils the relationship between the coupling coefficient and the cavity loss, and points out the conditions to realize the critical coupling in a high-Q resonator.

Fig. 3.9 shows a schematic of a two-dimensional taper to resonator coupling system. Light at a resonant wavelength E_i that is launched into the waveguide coupler will be coupled into the cavity and build up a large circulating optical power. A small fraction of this circulating power is re-emitted to the coupler, where it joins the field that is directly transmitted past the resonator (i.e., the uncoupled field) and forms the net transmitted field E_t.

Let κ be the amplitude of the field-coupling coefficient from the coupler to the resonator, and t the amplitude of the field-transmission coefficient through the coupler from the region before coupling to after coupling. Similarly, κ' and t' are the corresponding amplitudes of the coupling coefficient from the resonator to the coupler and the transmission coefficient inside the sphere, respectively. α is the amplitude loss factor of the cavity per round trip (caused by material absorption, whispering-gallery radiation loss, scattering from surface defects and contaminants, taper coupler scattering into radiation modes, etc.) and represents the fraction of the remaining field amplitude after one round trip in the cavity (excluding the taper coupling loss).

Assuming that the power scattering into radiation modes at the coupling region is negligible, i.e., the coupler is nearly lossless, the interaction at the coupling region can be described as

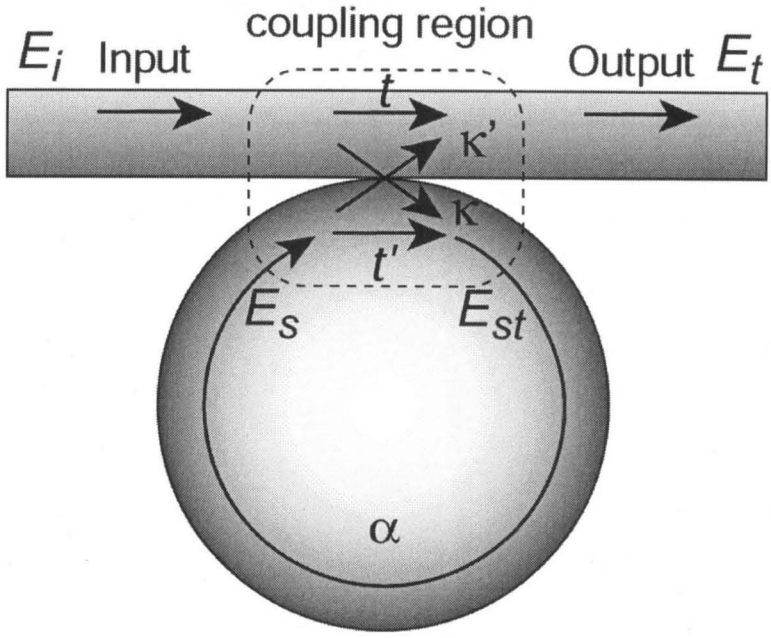

Figure 3.9 Illustration of a two-dimensional system that consists of a straight waveguide coupler and a disk resonator.

$$\begin{bmatrix} E_t \\ E_{st} \end{bmatrix} = \begin{bmatrix} t & \kappa' \\ \kappa & t' \end{bmatrix} \begin{bmatrix} E_i \\ E_s \end{bmatrix}, \tag{3.5}$$

where E_s and E_{st} are nominal field amplitudes in the resonator just before and after coupling. Applying time reversal symmetry and energy conservation to Eq. (3.5) gives

$$\begin{cases} t = t' \\ \kappa = \kappa' \\ t^2 - \kappa^2 = 1. \end{cases} \tag{3.6}$$

Furthermore, t and κ are purely real and imaginary numbers, respectively.

Note that the transmission inside the resonator is given by

$$E_s = \alpha E_{st} e^{i\varphi}, \tag{3.7}$$

where φ is the phase change in a round trip. From Eq. (3.5)-(3.7), we obtain

$$\frac{E_t}{E_i} = \frac{-\alpha + te^{-i\varphi}}{-\alpha t + e^{-i\varphi}}. \tag{3.8}$$

Therefore, the power transmission $T = \left|\frac{E_t}{E_i}\right|^2$ passing the resonator in the coupler is

$$T = \frac{\alpha^2 + t^2 - 2\alpha t\cos\varphi}{1 + \alpha^2 t^2 - 2\alpha t\cos\varphi}. \tag{3.9}$$

The cavity is on resonance when the circulating wave in the resonator returns in phase after a round trip, i.e., the phase change per round trip $\varphi = 2m\pi$, where m is an integer. This gives the power transmission on resonance T_o

$$T_o = \left|\frac{\alpha - t}{1 - \alpha t}\right|^2. \tag{3.10}$$

Eq. (3.10) is of special interest. Zero transmission is obtained when $t = \alpha$. This condition, referred to as critical coupling, is due to complete destructive interference in the outgoing waveguide between the transmitted field and the field re-emitted from the resonator to the coupler. Non-zero transmission is obtained for both cases of $t < \alpha$ and $t > \alpha$, to which we conventionally refer as respective under-coupling region and over-coupling region.

The quality factor of a loaded resonant mode is defined as $Q = \omega/\Delta\omega$ in Eq. (2.15). One can derive $\Delta\omega$ from Eq. (3.9), and thus the quality factor as follows

$$\Delta\omega = \frac{c}{\pi n_s R}\frac{1-\alpha t}{\sqrt{\alpha t}}$$
$$Q = \frac{2\pi^2 n_s R}{\lambda}\frac{\sqrt{\alpha t}}{1-\alpha t}, \tag{3.11}$$

where R is the radius of the resonator, n_s is the refractive index, and λ is the resonant wavelength.

Generally, it is more interesting to specify the coupling coefficient κ rather than the transmission coefficient t. Also, for convenience, we define β, the total loss coefficient per round trip in the cavity, in terms of α as $\alpha^2 + \beta^2 = 1$. Eq. (2.10) can thus be rewritten as

$$T_o \approx \left(\frac{\beta^2 - |\kappa|^2}{\beta^2 + |\kappa|^2} \right)^2, \tag{3.12}$$

given that β^2 and $|\kappa|^2$ are both far less than 1. Therefore, the critical coupling condition can be restated as

$$|\kappa|^2 = \beta^2. \tag{3.13}$$

The physical meaning of the critical coupling is obvious here. The power coupled into the cavity is totally dissipated by the cavity loss when circulating around the resonator. No energy escapes from the cavity and thus zero transmission through the coupler is achieved.

Fig. 3.10 shows the power transmission through the coupler against the internal loss factor α for given values of t. Due to the symmetry of α and t in Eq. 3.10, the same plots are obtained for the power transmission against the coupling parameter t for given values of α. The dependence of the transmission on α (or t) near the critical coupling point is particularly dramatic. It is obvious that one can control the transmission, and thus the power flow, through the coupler by tuning either cavity loss or the coupling strength. This control is

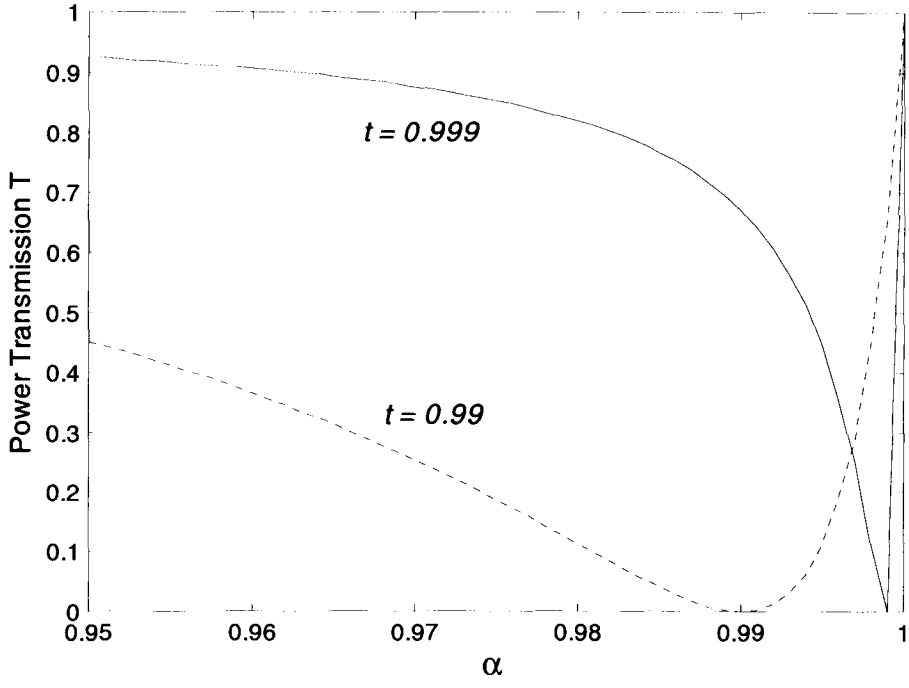

Figure 3.10 Power transmission through the coupler as a function of internal round trip loss factor α for the coupling parameter $t = 0.999$ and $t = 0.99$, respectively.

extremely sensitive near the critical coupling point in a high-Q cavity (corresponding to the case where $\alpha \to 1$ ($\beta \to 0$) and $t \to 1$ ($|\kappa| \to 0$)).

3.4 Symmetrical Taper-Resonator-Taper Structure

In the previous section, we have modeled the power transfer between a straight waveguide coupler and a disk resonator. The central results depend only on the coupling parameters (t/κ) and the internal cavity loss parameters (α/β). For a relatively large resonator ($D/\lambda \geq 15$, where D is the resonator diameter, λ is the

wavelength) without surface contaminants, the internal cavity loss is dominated by the material absorption and Raleigh scattering [1, 21]. The attenuation in fused silica, for example, can be as low as 0.2 dB/km within the 1550 nm band. This corresponds to an absorption-limited quality factor of about 10^{11}. In such a high-Q resonator, the fundamental sphere modes will likely be over-coupled using the fiber taper coupling technique, where the tapered fiber and the sphere are usually in contact. Consequently, the coupling efficiency (defined as the fraction of power absorbed by the resonator) is low. (Note that under-coupled region is also accessible provided that the highly precise positioning equipment is available to retain a very narrow gap between the taper and the sphere. This has been observed and is to be shown later in chapter 5.)

A symmetrical coupling geometry is considered to improve the coupling efficiency, as shown in Fig. 3.11. In this taper-resonator-taper (TRT) structure, one fiber taper serves as the input coupler, and another identical one as the output coupler. They are tangentially placed at the opposite sides of the equatorial plane of the microsphere. As a result, a small portion of the circulating power in the resonator is coupled to the output taper as E_k. From the point of view of the input coupler, the presence of the second coupler merely modifies the internal loss parameter from α to $\alpha t_2''$. All expressions derived in Section 3.3 apply, provided we replace α with $\alpha t_2''$, and t with t_2 (κ with κ_2). The power transmission on resonance T_{2o} becomes

$$T_{2o} = \left| \frac{\alpha t_2'' - t_2}{1 - \alpha t_2'' t_2} \right|^2 \tag{3.14}$$

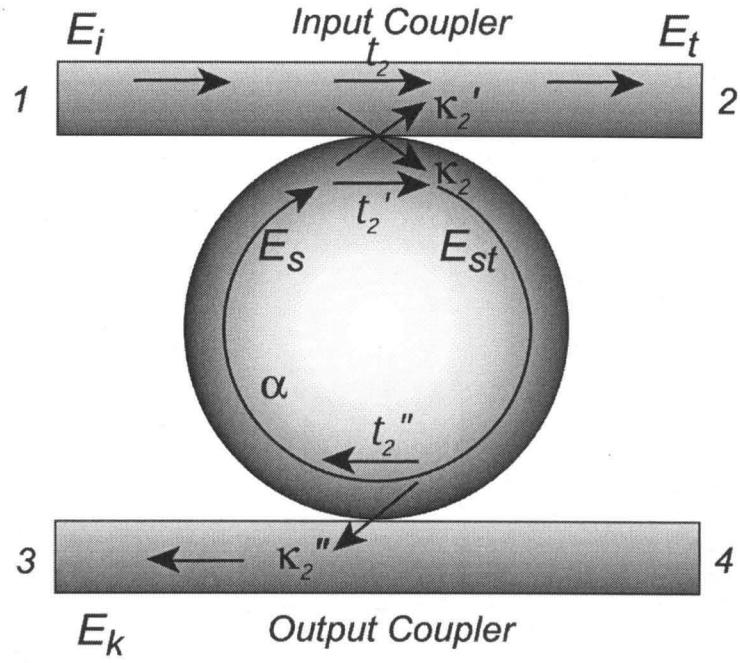

Figure 3.11 Schematic of a taper-resonator-taper coupling structure, where two identical straight tapers served as input and output couplers for a single resonator.

and the fraction of the optical power transferred to the output coupler is given by

$$\left|\frac{E_k}{E_i}\right|^2 = \frac{(1-t_2^2)(1-t_2''^2)\alpha}{(1-\alpha t_2'' t_2)^2}. \tag{3.15}$$

To obtain zero transmission through the input coupler, the critical coupling condition becomes $\alpha t_2'' = t_2$, and thus Eq. (3.15) is simplified as

$$\left|\frac{E_k}{E_i}\right|^2 = \frac{\alpha - t_2'' t_2}{1-t_2^2}. \tag{3.16}$$

Full power transfer from the input waveguide to the output waveguide, i.e. $\left|\frac{E_k}{E_i}\right|^2 = 1$, occurs when the following two conditions are satisfied: (1) $\alpha \to 1$; (2) $t_2 = t_2''$. Note that the critical coupling condition $\alpha t_2'' = t_2$ remains valid in the limit of $\alpha \to 1$.

The reason that we employ two identical taper couplers is hence obvious. Since the internal cavity loss of a fused silica resonator is extremely low (satisfies condition 1), the second identical coupler provides an additional loss mechanism that balances the difference between $t(\kappa)$ and $\alpha(\beta)$ in the single taper coupling case (satisfies condition 2). Note that the loaded quality factors in the case of double taper coupling are only degraded by a factor of about 2 due to the coupling loss from the second taper coupler.

The dual-taper symmetrically coupling configuration enables highly efficient power transfer between two waveguides [9] and opens a number of potential applications [7, 22], as we will discuss later in Chapter 5 and 6.

Bibliography

[1] M. L. Gorodetsky, A. A. Savchenkov, and V. S. Ilchenko, "Ultimate Q of Optical Microsphere Resonators," *Optics Letters*, vol. 21, pp 453-455, 1996.

[2] V. B. Braginsky, M. L. Gorodetsky, and V. S. Ilchenko, "Quality Factor and Nonlinear Properties of Optical Whispering Gallery Modes," *Physics Letters A*, vol.137, pp. 393-397, 1989.

[3] V. S. Ilchenko, X. S. Yao, and L. Maleki, "Pigtailing the High-Q Microsphere Cavity: a Simple Fiber Coupler for Optical Whispering Gallery Modes," *Optics Letters*, vol. 24, pp. 723-725, 1999.

[4] A. Serpenguzel, S. Arnold, and G. Griffel, "Excitation of Resonances of Microspheres on an Optical Fiber," *Optics Letters*, vol. 20, pp. 654-656, 1995.

[5] N. Dubreuil, J. C. Knight, D. K. Leventhal, V. Sandoghdar, J. Hare, and V. Lefevre, "Eroded Monomode Optical Fiber for Whispering Gallery Mode Excitation in Fused Silica Microspheres," *Optics Letters*, vol. 20, pp. 813-815, 1995.

[6] J. C. Knight, G. Cheung, F. Jacques, and T. A. Birks, "Phase Matched Excitation of Whispering Gallery Mode Resonances by a Fiber Taper," *Optics Letters*, vol. 22, pp. 1129-1131, 1997.

[7] M. Cai, G. Hunziker, and K. Vahala, "Fiber-Optic Add-Drop Device Based on a Silica Microsphere-Whispering Gallery Mode System," *IEEE Photonics Technology Letters*, vol. 11, pp. 686-687, 1999.

[8] G. Griffel, S. Arnold, D. Taskent, A. Serpenguzel, J. Connolly, and N. Morris, "Morphology-Dependent Resonances of a Microsphere Optical Fiber System," *Optics Letters*, vol. 21, pp. 695-697, 1996.

[9] M. Cai and K. Vahala, "Highly Efficient Optical Power Transfer to Whispering Gallery Modes Using a Symmetrical Dual-Coupling Configuration," *Optics Letters*, vol. 25, pp. 260-262, 2000.

[10] M. Cai, O. Painter and K. Vahala, "Observation of Critical Coupling in a Fiber Taper to Silica-Microsphere Whispering Gallery Mode System," *Physics Review Letters*, vol. 85, pp. 74-77, 2000.

[11] T. E. Dimmick, G. Kakarantzas, T. A. Birks, and P. S. J. Russell, "Carbon Dioxide Laser Fabrication of Fused Fiber Couplers and Tapers," *Applied Optics*, vol. 38, pp. 6845-6848, 1999.

[12] E. Snitzer, "Cylindrical Dielectric Waveguide Modes," *J. Opt. Soc. Am.*, vol. 51, pp. 491, 1961.

[13] A. Yariv, "Optical Electronics in Modern Communications," New York, Oxford University Press, 1997.

[14] R. J. Black and R. Bourbonnais, "Core-Mode Cutoff for Finite-Cladding Lightguides," *lEE Proceedings J,* vol. 133, pp. 377-384, 1986.

[15] A. C. Boucouvalas and G. Georgiou, "Tapering of Single-Mode Optical Fibers," *IEE Proceedings J*, vol. 133, pp 385-392, 1986.

[16] S. Lacroix, R. Bourbonnais, F. Gonthier and J. Bures, "Tapered Monomode Optical Fibers: Understanding Large Power Transfer," *Applied Optics*, vol. 25, pp. 4421-4425, 1986.

[17] R. J. Black, J. Lapierre, and J. Bures, "Field Evolution in Doubly Clad Lightguides," *lEE Proceedings J,* vol. 134, pp. 105-110, 1987.

[18] J. D. Love, W. M. Henry, W. J. Stewart, R. J. Black, S. Lacroix, and F. Gonthier, "Tapered Single-Mode Fibers and Devices: Part 1: Adiabaticity Criteria," *lEE Proceedings J,* vol. 138, pp. 343-354, 1991.

[19] R. J. Black, S. Lacroix, F. Gonthier and J. D. Love, "Tapered Single-Mode Fibers and Devices, Part 2: Experimental and Theoretical Quantification," *lEE Proceedings J,* vol. 138, pp. 355-364, 1991.

[20] D. R. Rowland, and J. D. Love, "Evanescent Wave Coupling of Whispering Gallery Modes of a Dielectric Cylinder," *IEE Proceedings J,* vol. 140, pp. 177-188, 1993.

[21] B. E. Litter, J. P. Laine, and H. A. Haus, "Analytic Theory of Coupling from Tapered Fibers and Half-Blocks into Microsphere Resonators," *Journal of Lightwave Technology*, vol. 17, pp 704-715, 1999.

[22] M. Cai, P.O. Hedekvist, A. Bhardwaj and K. Vahala, "5 Gbit/S BER Performance on an All Fiber-Optic Add/Drop Device Based on s Taper-Resonator-Taper Structure," *IEEE Photonics Technology Letters*, vol. 12, pp. 1177-1179, 2000.

Chapter 4

Fabrication of Microspheres and Fiber Tapers

4.1 Introduction

In previous chapters, we have given a theoretical description of the whispering gallery modes in the microsphere resonators and the tapered fiber to microsphere coupling features. Highly efficient power coupling to the microsphere and power exchange between two tapered fiber couplers have been projected. Sophisticated fabrication techniques for both the microspheres and the taper couplers are necessary to represent their unique properties physically in reality. In this chapter, we introduce the fabrication setups for both microspheres and fiber tapers. The procedures to obtain high-Q resonators and low-loss tapers are addressed in detail.

4.2 Fabrication of High Quality Microspheres

4.2.1 Description of Microsphere Fabrication Setup

Fused silica is an exceptional candidate for high-Q microspheres due to its ultra-low attenuation in the 1550 nm band, low cost, and compatibility with the fiber couplers and optical fiber systems. The fabrication procedure is basically obvious. First, remove the plastic coating of a piece of a single mode optical fiber (made of fused silica). The outer diameter of the fiber is generally about 125 μm. Then heat and pull the fiber into a thin thread (or taper) about 10-20 μm in diameter. Break the thread at the thinnest point, and then push it back into the heating source slowly. A microsphere grows automatically due to the surface tension. By controlling the length (or volume) fed into the heating source, one can virtually control the size of the microsphere. The residual fiber remains attached to the sphere for the convenience of handling.

Fig. 4.1 is a photograph of the actual microsphere fabrication setup in our lab. We use a SYNRAD 10W CO_2 laser (10.6 μm in wavelength) as the heating source (at the far back side), due to the strong absorption of silica in the infrared band. Other heating sources, for example, a Hydrogen flame, are also used by several other groups [1, 2]. As shown in Fig. 4.1, the CO_2 laser is guided by two reflective mirrors to the front side. It is then focused towards the control stages where microspheres are made. A 350× (overall) microscope is placed vertically with the focusing plane across the focus spot of the CO_2 laser such that the procedure of making spheres can be monitored using a CCD camera and thus

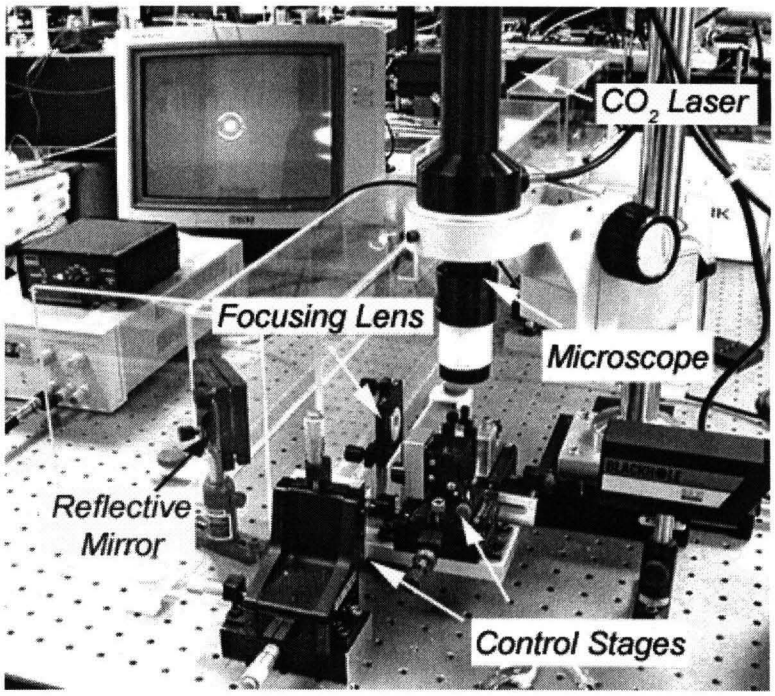

Figure 4.1 Setup for fabricating microspheres.

displayed on a screen. A beam blocker is used at the end of the setup to absorb the residual CO_2 laser radiation. The control stages holding the microsphere consist of a few three-axis/two-axis translators and a rotation stage, which enable flexible handling of the fiber stem, and thus the sphere. The CO_2 laser path through the optical table is covered with plastic hoods for safety.

A picture of a fused silica microsphere made using this setup is shown in Fig. 4.2 (a). Microspheres of diameter sizes from tens of microns to up to a few hundred microns can be easily fabricated using a CO_2 laser. There exist limitations in making high quality spheres of a size smaller than 20 μm or larger than 300 μm. Since the wavelength of the CO_2 laser is about 10.6 μm, the laser is likely scattered instead of thermally absorbed by the microspheres if their sizes

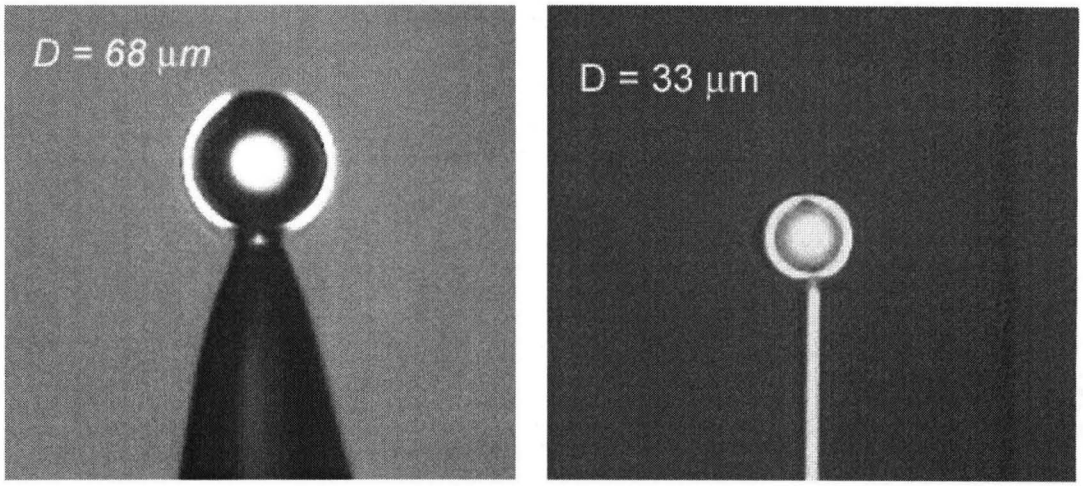

(a) (b)

Figure 4.2 Magnified pictures of (a) a fused silica microsphere of 68 μm in diameter and (b) an Er^{3+}/Yb^{3+} co-doped phosphate glass microsphere of 33 μm in diameter.

are comparable to the laser wavelength. On the other hand, spheres larger than 300 μm require comparable laser spot size so that they can be heated uniformly during the process. This would in turn require a higher power laser with the beam expanded appropriately. In fact, a Hydrogen flame can provide a large uniform heating area, which is suitable for making large spheres. Up to 4 cm "microspheres" have been reported using this method [3].

Fig. 4.2(b) shows a 33 μm microsphere that is made of erbium:ytterbium co-doped phosphate glass. Doped spheres are prepared for microsphere laser applications that we will present in Chapter 7. Extra care is needed for processing phosphate glass. The Er^{3+}/Yb^{3+} co-doped phosphate glass QX/Er is provided by Kigre, Inc. It comes as a $1'' \times 1'' \times 1$ cm slab. We first cut it into very small pieces, about 0.5-1 mm in each dimension. One of these pieces is then

placed in a metal crucible. The crucible is preheated electrically to about 480°C, which is slightly higher than the melting point of QX/Er at 450°C. The doped phosphate glass is then melted gradually and uniformly in the crucible. A section of an optical fiber, with the coating material at one end stripped off, is prepared. Since the melting point of silica 1700°C is far above the melting point of QX/Er, the optical fiber serves as a perfect supporting stem for the phosphate glass. We dip the cleaned end of the optical fiber into the melt of QX/Er and then pull it out quickly. The phosphate glass then attaches on the fiber and forms a long thin thread at the end of the fiber. The diameter of the phosphate thread is usually in the range from 5 to 20 μm. This piece of fiber is then moved to the microsphere fabrication setup. With the same procedure as making a fused silica microsphere, a doped phosphate glass microsphere is then obtained.

Several crucial points need to be taken into consideration during the fabrication. One is the cooling procedure. The phosphate glass has to be cooled down twice from the melting point during the fabrication (pre-preparation of a thin thread and finalization into a sphere after heating with the CO_2 laser). Differing from fused silica, the phosphate glass intends to crystallize as clusters if the cooling course is slow enough, which destroys the homogenous distribution of the erbium and ytterbium ions, and causes scattering loss. Therefore, quick removal from the heating source is necessary after the thread or the sphere is formed. The other crucial point is the contamination of the phosphate glass when heating in the crucible. To obtain as high temperature as 480°C locally in an open area, we usually heat a metal crucible by applying electrical current.

Contamination by dissolution of the metal ions can be disastrous for the final applications. Platinum is therefore the material of choice when the highest purity glasses are required. Careful control of the atmosphere under which melting takes place is also important for controlling the amount of water chemically absorbed in the glass, as well as the redox state of various dopants.

4.2.2 Eccentricity of Real Microspheres

The microspheres in reality are in general not perfectly spherical. They are either slightly oblate or stretched. Because of the strong confinement of the whispering gallery modes near the equatorial plane, the residual fiber stem has minimal perturbation on the resonant modes if the stem size is three times less than the sphere size [4]. The ellipticity of the microsphere, however, breaks the m degeneracy for modes with equal l and n but different m values. In Chapter 2, Eq. (2.8) gives the resonant frequencies for a perfect microsphere. Here, the first order approximation of the frequency shifts due to a slightly deformed cavity can be estimated by

$$\frac{\omega_{n,l,l} - \omega_{n,l,m}}{\omega_{n,l,l}} = \pm \frac{l^2 - m^2}{4l^2} \varepsilon^2, \tag{4.1}$$

where a positive sign stands for oblate spheroid and negative sign for a prolate spheroid one, and ε^2, the eccentricity of the sphere, is related to the axial and equatorial semi-axes r_a and r_e by the expression $\varepsilon^2 = 2|r_e - r_a|/r_e$.

In our experiments, the eccentricity of the microspheres can be calculated with Eq. (4.1) by identifying a series of the m-splitting modes. In general, the eccentricity falls within the range of 1-3%.

4.3 Fabrication of Tapered Fibers

An ideal taper coupler is lossless and propagates only the fundamental taper mode in the taper-sphere coupling region. As we have shown in Chapter 3, the adiabatic criterion (or slowness criterion) is required to obtain such an ideal taper coupler.

Fig. 4.3 shows the taper fabrication setup in our lab. A section of a standard single mode fiber is prepared by removing the plastic coating for about $1''$ in length and then cleaned. It is then clamped on a pair of motorized translators. Each of the translators has a resolution of $0.1\,\mu m/\,step$, and speed from $0.5\,\mu m/s$ to $200\,\mu m/s$. A Hydrogen microtorch is placed underneath the prepared optical fiber. A microscope is installed horizontally for monitoring the pulling process.

During the tapering procedure, the Hydrogen torch is lighted and the two translators move apart in opposite directions at a certain speed. The taper loss is closely monitored by detecting the power transmission through the tapered fiber.

We have noticed that the flame position, Hydrogen flow, and the pulling speed are all important factors in obtaining the adiabatic taper transition. Precise

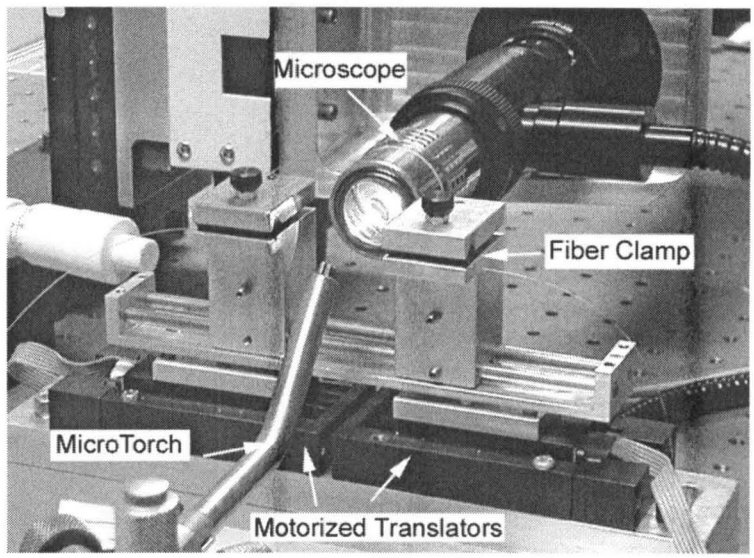

Figure 4.3 Fabrication setup for fiber tapers

control and adjustment of these parameters are necessary to locate the desired pulling conditions. Once the lossless power transmission is recorded, high quality tapers are reproducible under the same conditions.

In our experiments, the traveling length of each translator is limited to 13 mm. To obtain a taper as thin as 2-3 μm in diameter under the slowness criterion, we make use of the full traveling length of the translations while keeping the pulling speed as low as possible. A relatively small speed of 20 $\mu m/s$ is generally applied. The torch position and the Hydrogen flow are adjusted accordingly.

Tapers of diameters ranging from 1-3 μm with loss less than 0.1 dB are routinely fabricated under these conditions. A magnified photograph of a tapered fiber is shown in Fig. 4.4. The diameter of the taper is about 2.5 μm. For comparison, a picture of the optical fiber (125 μm in diameter) before tapering is also shown in the same figure.

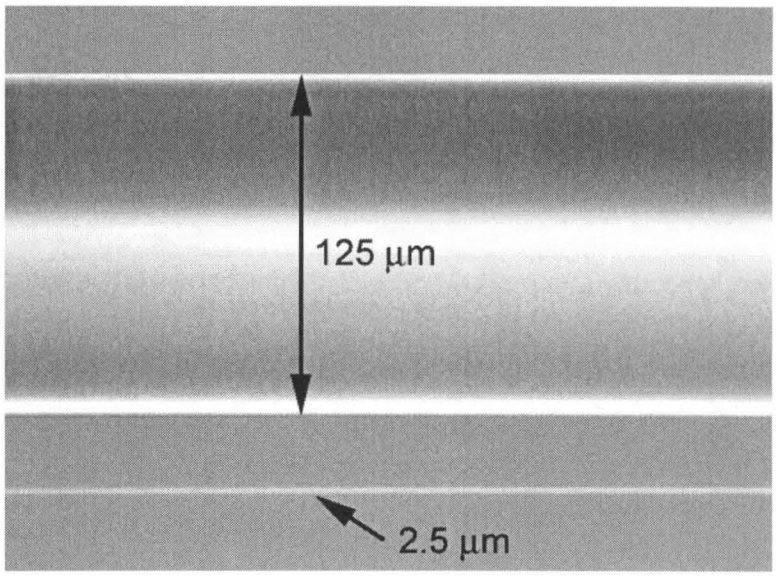

Figure 4.4 Magnified photograph of a tapered fiber about $2.5\ \mu m$ in diameter. For comparison, a standard single mode fiber of $125\ \mu m$ in diameter is also shown.

The profiles of the tapers fabricated using this method can be described reasonably by a parabolic model [6]. Considering that the total elongation of the taper in our experiments is about $26\ mm$ and the size of the micro-torch is about $5\ mm$, using the model in Ref. [6], the local taper length-scale z_t is estimated to be about 7 mm. It is much larger than the beating length z_b between LP_{01} and LP_{02} modes at 1550 nm, which is about 0.9 mm. The slowness criterion is thus satisfied in our experiments.

We have discussed the advantages of the symmetrical taper to sphere coupling configuration in Chapter 3. To fabricate a pair of nearly identical fiber tapers, we clamp two fibers closely in parallel, and then pull them simultaneously. A slightly stronger flame is applied to provide sufficient heat to melt the fibers while other conditions are kept the same. The two fibers are

separated naturally. The spacing, however, can be adjusted to fit the size of the microsphere by applying a couple of needles to push or pull one fiber toward or away from the other one. The needles are usually placed far away from the taper region, and therefore have almost no perturbation to the taper modes or the taper to sphere coupling.

4.4 Typical Measurement Setups

To characterize the taper to microsphere coupling system, it is very convenient to measure the transmission spectra at the throughput end of the taper coupler. Shown in Fig. 4.5 is a schematic of the typical transmission spectrum measurement setup. A New Focus tunable external-cavity diode laser, having a linewidth of less than 300 KHz, is used as the laser source. It is continuously scanned around 1550 nm using a periodic triangle signal. Field intensity inside the sphere can be extremely high when it is on resonance. To avoid the undesired distortion on the resonance spectra caused by the instant heating, the frequency of the scanning signal is set at a relatively low value of about 40 Hz, such that the heat can be released within one scanning period. A low-noise photo-detector with a bandwidth of 125 MHz is used to collect the laser power at the throughput end of the taper coupler. The electrical waveform is then displayed on a digital oscilloscope.

Figure 4.6 shows the experimental setup for characterizing the taper-sphere

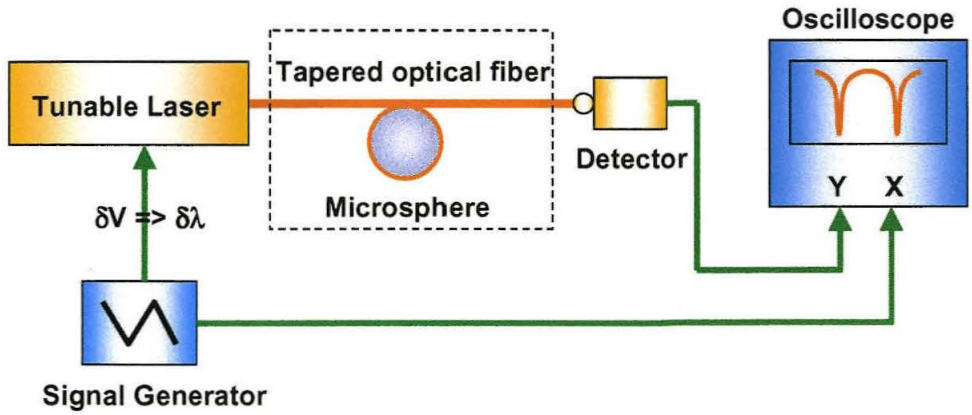

Figure 4.5 Schematic of the transmission spectrum measurement setup.

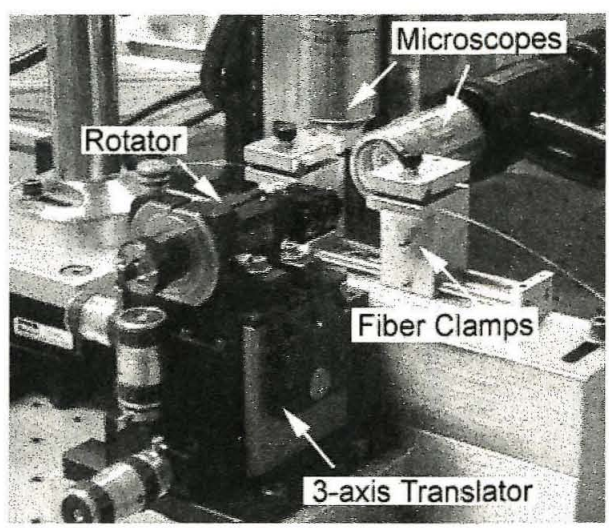

Figure 4.6 Experimental setup for characterizing the taper-sphere coupling system.

coupling system. After fabrication, the fiber taper coupler is moved to this setup. The microsphere is held using a Thorlabs rotator and mounted on a three-axis precise translator. Two microscopes with CCD cameras are placed in horizontal and vertical directions, respectively, to monitor the alignment between the taper

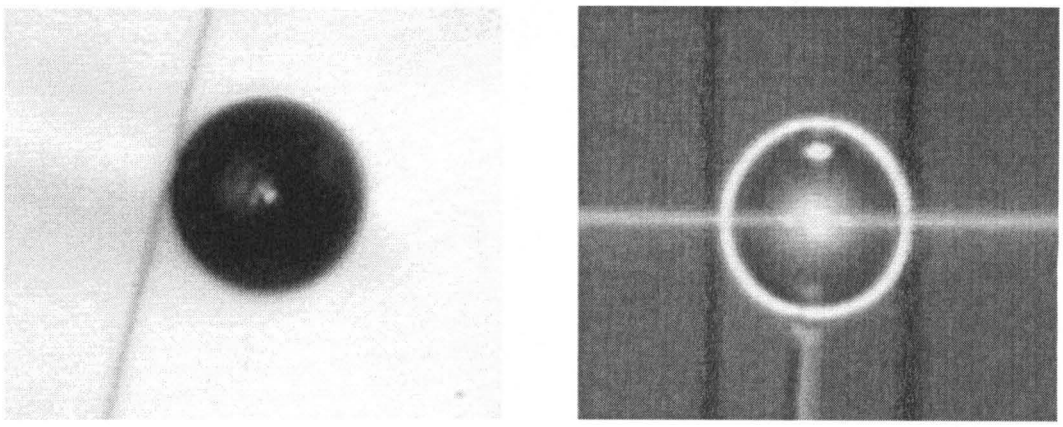

(a) (b)

Figure 4.7 Magnified photography of a single fiber taper to microsphere coupling system (a) top view and (b) side view, respectively.

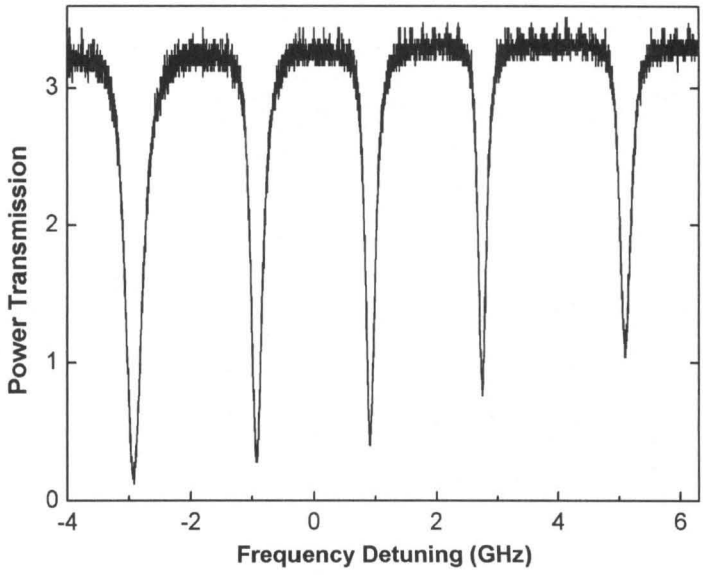

Figure 4.8 Typical transmission spectrum measured at the throughput end of the taper coupler. The transmission dips correspond to the whispering gallery mode resonances in the microsphere cavity.

and the sphere. Fig. 4.7 (a) and (b) show magnified photography of a single taped fiber coupled to a microsphere from the top and side views, respectively. A typical transmission spectrum read from the digital oscilloscope for such a system is shown in Fig. 4.8. As we have discussed in Chapter 2, the whispering gallery modes are characterized by four indices (p, n, l, m), where p designates either TE or TM polarization while (n, l, m) are radial and angular indices. In an ideal sphere each (n, l, m) subspace is $2l+1$ degenerate. Actual resonators exhibit slight eccentricity that splits the resonant frequencies into $2l+1$ distinct values associated with the index m. The size and the refractive index of the microsphere determine the resonant frequencies which are associated with the indices n and l. The whispering gallery mode resonances in an actual sphere are thus easily identified with these mode indices. The transmission dips shown in Fig. 4.8 are associated with the modes that have the same n and l, but different m indices. They are split by the resonator eccentricity.

Fig. 4.9 shows a symmetrical double-taper to microsphere coupling system. The characteristics of the transmission spectra from each port of the couplers and potential applications of this structure will be addressed in the next two chapters.

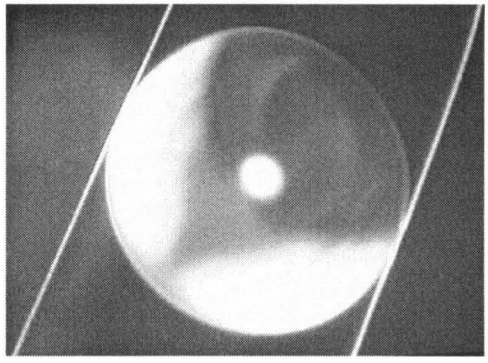

Figure 4.9 Magnified photography of a double-taper to sphere coupling system.

Bibliography

[1] V. B. Braginsky, M. L. Gorodetsky, and V. S. Ilchenko, "Quality Factor and Nonlinear Properties of Optical Whispering Gallery Modes," *Physics Letters A*, vol.137, pp. 393-397, 1989.

[2] S. W. Vernooy, V. S. Ilchenko, H. Mabuchi, E. W. Streed, and H. J. Kimble, "High-Q Measurements Of Fused Silica Microspheres in the Near Infrared," *Optics Letters*, vol. 23, pp. 247-249, 1998.

[3] S. Schiller and R. L. Byer, "High-Resolution Spectroscopy of Whispering Gallery Modes in Large Dielectric Spheres," Optics Letters, vol. 16, pp 1138-1140, 1991.

[4] F. Treussart, N. Dubreuil, J. Knight, V. Sandoghdar, J. Hare, V. Lefevre-Seguin, J.M. Raimond, and S. Haroche, "Microlasers Based on Silica Microspheres," *Annual Telecommunications*, vol.52, pp. 557-568, 1997.

[5] A. C. Boucouvalas and G. Georgiou, "Tapering of Single-Mode Optical Fibers," *IEE Proceedings J*, vol. 133, pp. 385-392, 1986.

[6] W. K. Burns, M. Abebe, and C. A. Villarruel, "Parabolic Model for Shape of Fiber Taper," *Applied Optics*, vol. 24, pp. 2753-2755, 1985.

Chapter 5

Experimental Observation of Taper to Sphere Coupling

5.1 Introduction

We have developed in Chapter 3 a simple two-dimensional model for a system that consists of a straight coupler and a disk resonator. Under the assumption that there is no radiation loss at the coupling region, only a few coupling parameters are necessary to describe the nature of the coupling system. The power transmission through the taper coupler is thus determined by two quantities: the coupling strength and the intrinsic cavity loss. For convenience, we rewrite Eq. (3.10), the transmittance on resonance as follows,

$$T_o = \left|\frac{\alpha - t}{1 - \alpha t}\right|^2 \approx \left(\frac{\beta^2 - \kappa^2}{\beta^2 + \kappa^2}\right)^2, \tag{5.1}$$

where $(a,\ \beta)$ are the fractions of the remaining field amplitude and the amplitude of the cavity loss after one round trip in the cavity, respectively; $(t,\ \kappa)$ are the amplitudes of the field transmission coefficient and the field coupling coefficient, respectively. For convenience, we replace thereafter $|\kappa|$ in Chapter 3 with κ, which now represents a real number. The relationships between these parameters are given by

$$\begin{cases} \alpha^2 + \beta^2 = 1 \\ t^2 + \kappa^2 = 1. \end{cases} \tag{5.2}$$

We also define that the system is under-coupled, critical coupled, or over-coupled if $\kappa < \beta$, $\kappa = \beta$, or $\kappa > \beta$, respectively.

Two significant facts have been derived from Eq. (5.1): (1) Zero transmission through the taper coupler is achieved if the coupling loss is equal to the intrinsic cavity loss (the critical coupling condition). (2) For an ultra-low loss cavity, highly efficient power transfer to the cavity can be realized using a symmetrical coupling structure.

In this chapter, we examine experimentally the tapered fiber to microsphere coupling systems. First of all, it is shown that the taper mode can be nearly ideally coupled into a whispering gallery mode, where the ideal coupling is defined as such that there is no radiation loss at the coupling region and the taper and sphere modes are phase-matched. For a nearly ideally coupled taper-sphere system, well-controlled critical coupling is then achieved by tuning either the cavity loss or the coupling strength to the cavity [1]. Finally, we demonstrate highly efficient power transfer in a taper-resonator-taper (*TRT*) *structure [2].*

Possible applications of these extremely efficient coupling systems are also discussed.

5.2 Observation of Ideal Coupling

Fused silica microspheres can support very high-Q whispering gallery mode resonances. These modes have a long lifetime and couple out of the cavities slowly. By reciprocity, they also couple into the cavities slowly. In other words, these modes are not easily accessible from the outer world. Efficient coupling into these resonators requires a near-field evanescent wave with perfect phase matching to the whispering gallery modes. Tapered optical fibers are such couplers that can be readily tailored to provide ideal coupling to different sized microspheres.

The amplitude of the field-coupling coefficient κ from the taper mode to the sphere mode can be evaluated using the couple mode theory as following:

$$\kappa = \int_{-\infty}^{+\infty} \kappa_0(z) e^{-i\Delta\beta z} dz, \tag{5.3}$$

where $\kappa_0(z)$ is the overlap integral between the fiber and sphere modes in the transverse plane (here, the x-y plane), and $\Delta\beta$ is the difference in propagation constants of the two modes. Obviously, the transverse overlap integral of the mode fields is a constant for a given x-y plane and a fixed air gap between the taper coupler and the microsphere, however, the overall coupling coefficient κ decreases exponentially as the phase mismatching $\Delta\beta$ increases. A large phase

mismatching between the taper mode and the sphere mode would render the microsphere resonator permanently under-coupled.

The resonant wavelength and the propagation constant of a sphere mode are well defined by the sphere size. Similarly, for a certain wavelength, the propagation constants of the mode in a straight cylindrical waveguide are determined only by the size of the waveguide and decrease as the diameter decreases (as shown in Fig. 3.6). Suppose we have an adiabatic taper coupler (satisfies with the slowness criterion), the local mode theory thus applies and the propagation constants of the taper modes along the taper are then determined by the local diameter of the taper. In other words, the propagation constant of a taper mode changes continuously along the gradually varied fiber taper. Therefore, by moving the sphere along the taper, one can eventually match the propagation constant of a sphere mode with that of the taper mode, provided that the taper waist is small enough. The phase matching condition becomes simply the size matching between the sphere resonator and the taper coupler.

5.3 Observation of the Critical Coupling

Ideal coupling from a nearly lossless taper coupler to a microsphere can be obtained by matching the sizes of the taper and the sphere. Since the field overlap integral $\kappa(z)$ increases monotonically as the taper size decreases while the phase mismatching factor $e^{i\Delta\beta z}$ does not, the overall coupling coefficient κ (*see* Eq. 5.1) is evolved in a complicated way along the taper. Simply moving the

sphere along the taper does not guarantee the matching between the coupling coefficient κ and the cavity loss β, and thus the critical coupling. In this section, we demonstrate extremely efficient control of resonator coupling in a well-tailored fiber taper coupler to high-Q microsphere system by tuning either the resonator loss or the coupling strength.

We first prepared a fiber taper and a fused silica microsphere using the technique described in Chapter 4. The diameter of the microsphere was about $150\ \mu m$, and the taper coupler was fabricated with a diameter optimized to ideally match the size of the sphere. Fig. 5.1 shows the transmission spectrum for the sphere-taper system, and the inset shows a magnified image of the fiber-taper attached to the microsphere.

To study critical coupling, a plastic probe having a smooth, round tip was prepared by slightly melting the tip of a multimode plastic optical fiber. The diameter of the probe tip was made comparable to the microsphere diameter so as to minimize probe-induced backscattering within the resonator. In addition, the plastic material was lossy in the $1.55\ \mu m$ band so that power coupled from the resonator would be quickly absorbed within the probe. The probe was positioned near the microsphere using a piezoelectric motor with a $0.2\ \mu m$ resolution encoder for reading off the position of the probe. By approaching the probe to the surface of the microsphere, the total cavity loss of the resonant modes was increased due to the probe scattering and absorption.

The fiber taper was tailored and aligned to the microsphere such that the

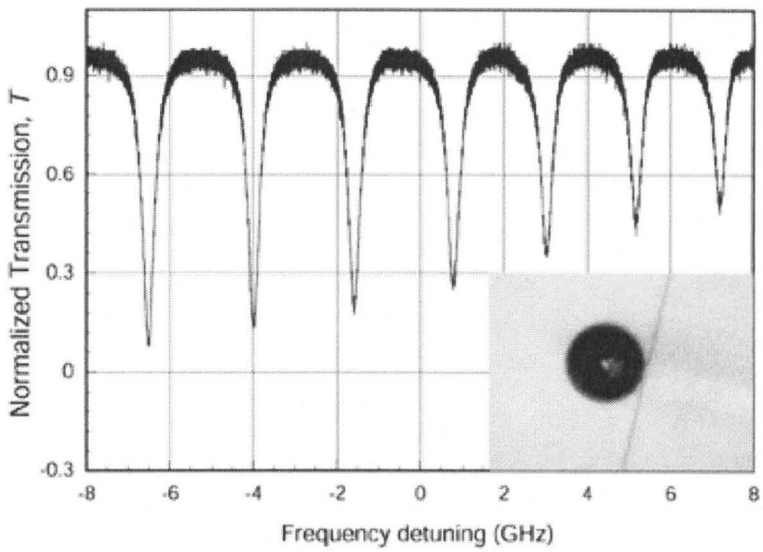

Figure 5.1 Typical transmission spectrum for the microsphere-taper system. The inset shows a magnified image of the fiber taper attached to the microsphere.

fundamental taper mode is ideally coupled to a resonance that is near fundamental whispering gallery mode ($n = 1$, $m \approx l$). Power transmission was measured for this mode as the probe position was varied in the vicinity of the microsphere. Figure 5.2 shows the resonant transmission versus probe position. A clear minimum versus probe position is apparent in the figure, corresponding to the critical point. Note that prior to the probe being brought into close proximity of the microsphere (0 point) the taper-microsphere system is biased well into the over-coupled regime ($T > 70\%$). In fact, over-coupled transmissions of greater than 95% were observed for optimum taper diameters, limited by our ability to accurately measure the transmission and linewidth due to overlap with other

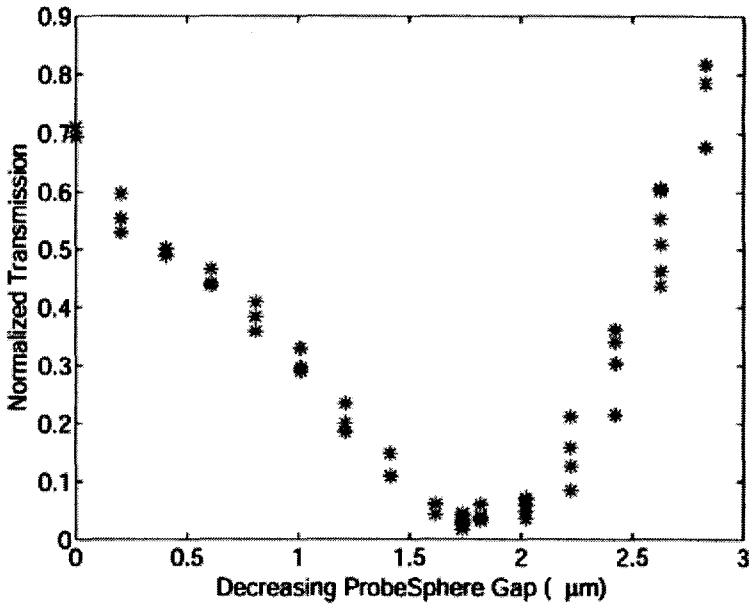

Figure 5.2 Normalized transmission as a function of the probe position for a near fundamental ($n=1$, $m \approx l$) whispering gallery mode in a $150\,\mu m$ microsphere. The horizontal axis gives the change in the distance of the probe to the microsphere relative to an arbitrary position.

whispering gallery modes. The role of taper diameter here is believed to result from phase-matched mode selection. This mechanism favors whispering gallery mode coupling to the fundamental taper mode as opposed to higher order taper modes. The ability to detect the critical point and to push the taper-microsphere system well into the over-coupled regime attests to the highly ideal nature of the taper-to-sphere junction.

Since the probe position is not linearly related to the mode loss (in addition there is variation in the motor step movement from step to step), a better way to plot the transmission data is shown in Fig. 5.3. In this plot, *the on-resonance*

power transmission is shown plotted versus the linewidth of the resonant whispering gallery mode. Linewidth is a convenient measure of the mode loss and increases as the probe position is advanced towards the sphere. Transmission versus linewidth can also be easily calculated using the simple model of Eq. (5.1). For comparison, a calculation is provided in Fig. 5.3, where the transmission coefficient t is fit to match the linewidth at the critical point. The critical coupling loss rate can be read directly off this kind of plot, giving it an even greater value to ascertain properties of the taper-sphere system. As an aside, note that the Q values of the loaded sphere in this measurement are between $10^6 \sim 10^7$. The extremely sharp transition from the over-coupling region to the critical point and the correspondingly minute variation in resonator loss bode well for application of these structures as improved sensing devices [3].

Extinction in the vicinity of the critical point was difficult to assess owing to minute fluctuations in the probe's position affecting the power transmission. However, by covering the probe-taper-resonator system in a small box the stability improved sufficiently to enable more careful examination of the critical point region. The probe was set at a fixed distance from the sphere, and the taper-sphere gap was varied to adjust the coupling to the critical point. In this case the taper was slightly detached from the sphere. A plot of the on-resonance transmission versus linewidth is shown in Fig. 5.4, along with a one- parameter fit in which the resonator round-trip amplitude (α) was chosen to match the linewidth at the critical point. Extinction as high as 26 dB in the

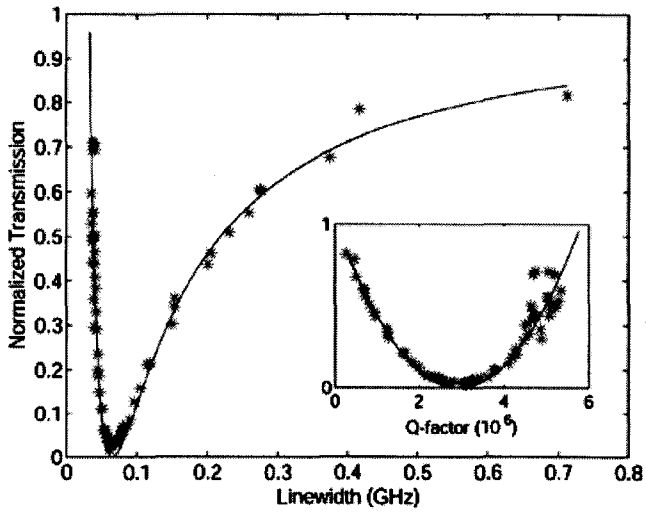

Figure 5.3 Power transmission as a function of the linewidth (FWHM) of the mode for varying probe position (and resulting absorption). The solid line is calculated using the simple model of Eq. 5.1 with t fixed. The inset shows the transmission as a function of the microsphere loaded Q.

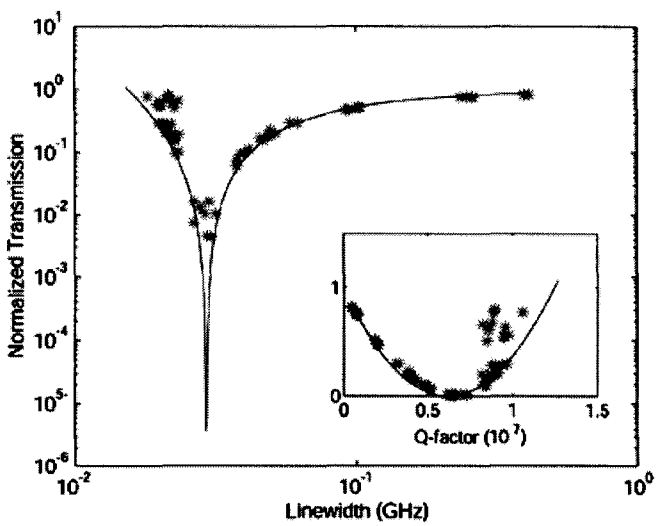

Figure 5.4 Power transmission as a function of the linewidth (FWHM) of the mode for varying taper-sphere coupling gap. The solid line is calculated using the simple model of Eq. 5.1 with α fixed. The inset shows the transmission as a function of the microsphere loaded Q.

transmitted power was measured, limited by the degree of control over the input wave polarization in the fiber.

Another important test of the junction is to measure the non-resonant insertion loss associated with the sphere being in contact with the taper. For this measurement, a trace of the transmission spectrum was stored using a digital oscilloscope both with and without the sphere in contact with the taper. The difference of the two traces was then computed to ascertain the insertion loss. By proper selection of the taper diameter this value was observed to be less than 0.3%. The optimal taper diameters were in the range of three microns for the spheres studied here.

5.4 Highly-Efficient Power Transfer in a Taper-Resontator-Taper Structure

Section 5.3 has shown that one can obtain critical coupling for a whispering gallery mode by matching the coupling strength to the cavity loss. Once coupling is optimized for a particular mode, other adjacent modes, however, would be mismatched due to their distinct spatial locations and field distributions, which results in different coupling coefficient κ and loss coefficient β for each mode. In this section, we first examine quantitatively the relationship between the coupling and loss coefficients for a series adjacent modes in a single taper coupled microsphere resonator. A dual-taper coupling scheme is then introduced to

improve dramatically the coupling efficiency for each of these modes. Both experimental results and theoretical analysis are given.

The transmission spectra of the resonance system are extremely informative. The transmittance and linewidth of each on-resonance whispering gallery mode are readily read off from the spectra. The mode linewidth can be expressed as (*see* Eq. 3.11)

$$\Delta\omega = \frac{c}{\pi n_s R}\frac{1-\alpha t}{\sqrt{\alpha t}}. \tag{5.4}$$

Therefore, with Eqs. (5.1) and (5.4), the transmission coefficient t and the cavity loss factor α for each resonant mode can be inferred from the experimental data. Generally, it is more interesting to specify the coupling coefficient κ and cavity loss coefficient β rather than the transmission coefficient t and loss factor α.

Fig. 5.5 shows a typical normalized transmission spectrum for a single tapered-fiber coupled microsphere resonant system. These modes have the same n and l indices, but different m values. The microsphere resonator had a diameter of about 140 μm, and the wavelength of the scanning laser is near 1550 nm. Fig. 5.6 shows the calculated results for κ_1^2 and β_1^2 in this case, where subscript 1 is used hereafter to refer to the quantities in the single taper coupling case, while subscript 2 will be used to refer to those in the dual-taper coupling case. Note that t and α (and thus κ and β) are symmetrical in both Eqs. (5.1) and (5.4). They can be identified, however, by an argument that modes differing only from m indices have nearly identical cavity loss in a uniform resonator

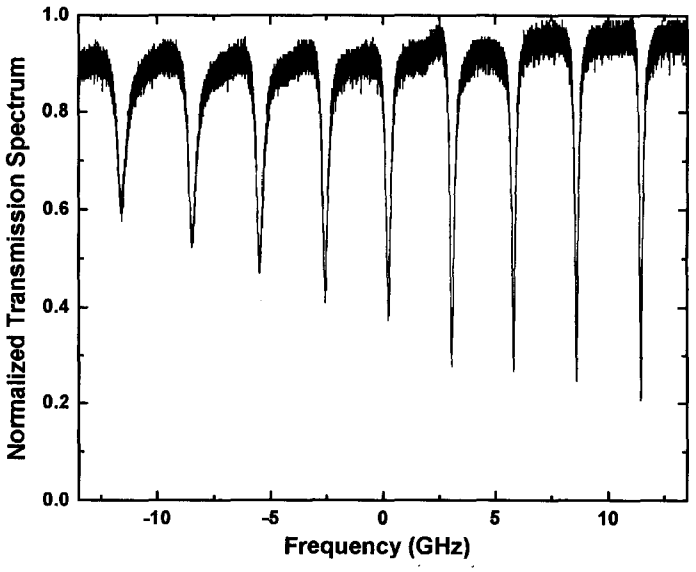

Figure 5.5 Normalized transmission spectrum for a single taper coupled microsphere resonator system.

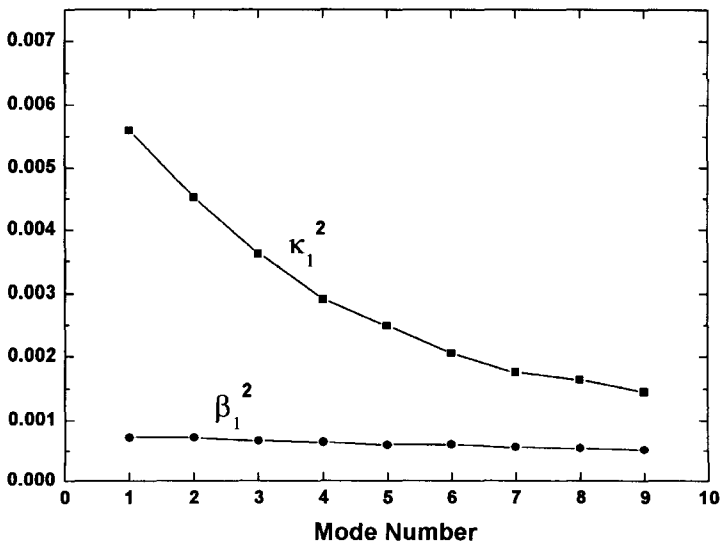

Figure 5.6 Calculated coupling coefficients κ_1^2 and total cavity loss β_1^2 corresponding to the spectrum shown in Fig. 5.6.

(they are virtually degenerate in a perfect spherical cavity), while the coupling strength of these modes vary significantly due to their distinct spatial locations. We will verify this argument later by comparing with the results from double taper coupled resonator system.

It is apparent from the calculation results in Fig. 5.6 that the taper-microsphere resonant system was over-coupled ($\kappa > \beta$ for each mode). The cavity loss coefficients β_1^2 were at least two times smaller than the coupling coefficient κ_1^2. Consequently, the coupling efficiencies of these modes were generally in the range $40 \sim 80\%$.

In Chapter 3, we have predicted theoretically that by applying a second nearly identical coupling to a low intrinsic loss cavity, one can expect high power transfer (critical coupling) to the cavity from the first coupler.

We demonstrated this idea using a symmetrical taper-resonator-taper (TRT) structure as illustrated in Fig. 5.7 (a). Two nearly identical taper couplers are placed tangentially at the opposite sides of the equator of a microsphere. One serves as the input coupler, while the other is the output coupler. Light at a resonant wavelength that is launched into the input coupler will be coupled into the cavity and buildup a large circulating optical power. A small fraction of this circulating power is re-emitted to the input coupler where it joins the field that is directly transmitted past the sphere (i.e., the uncoupled field) and forms the net transmitted field E_t. Likewise, at the other taper, a small portion of the circulating power is coupled out to the second fiber taper as E_k. This coupling

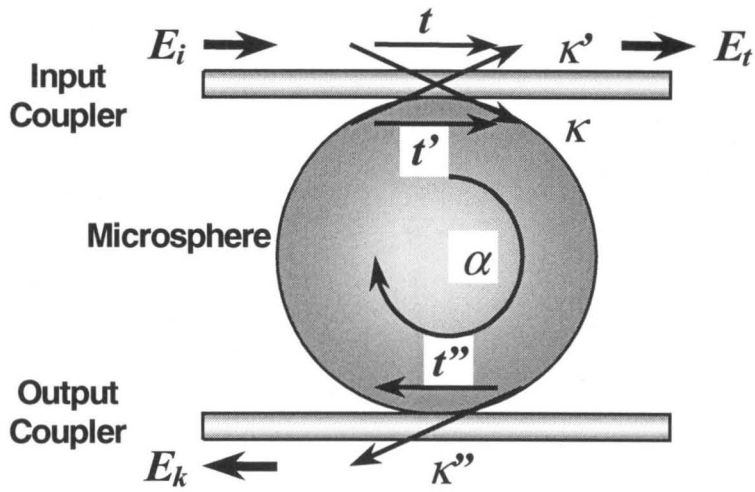

(a)

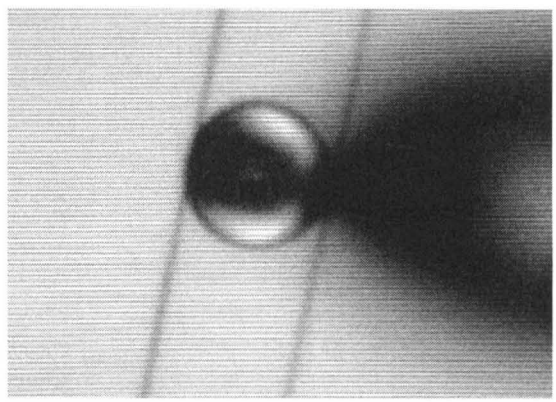

(b)

Figure 5.7 (a) Schematic of a microsphere resonator in the dual-taper coupling configuration. (b) Magnified photograph of the actual system. The background shadow is produced by the fiber stem, which is used to hold the sphere.

acts effectively as an added cavity loss in the dual-taper coupling measurements. Fig. 5.7 (b) is a micrograph of the actual system and shows two tapered-fibers attached to a fused-silica microsphere. The shadow on the background is the image of the glass stem that is used to support and manipulate the microsphere. Transmission spectrum at the throughput of the input fiber for the dual-taper coupled resonant system was measured as shown in Fig. 5.8. One can find immediately that the dual-taper coupling scheme dramatically improved the power transfer efficiencies not only for a particular whispering gallery mode, but also for a wide range of adjacent modes. The measured transmitted power at the center frequency of the resonance marked with an asterisk in figure 5.8 was less than $-28\,dB$, corresponding to a coupling efficiency that is greater than 99.8%. For those resonances marked with arrows, the transmittances were less than $-20\,dB$, corresponding to greater than 99% power transfer. The corresponding coupling coefficients κ_2^2 and the total cavity loss β_2^2 were calculated as in Fig. 5.9. The system is slightly under-coupled ($\kappa_2 < \beta_2$). The determination of κ_2^2 and β_2^2 will be reasoned later.

For comparison, we usually first measured the transmission spectra in the dual-taper and then in the single-taper coupling system. We did this by first measuring the dual-taper system spectrum and then gently detaching the second fiber taper (the output coupler) from the sphere to maintain the coupling condition between the first fiber taper (the input coupler) and the microsphere. Actually, the transmission spectra in Fig. 5.5 and 5.8 were just taken under this procedure.

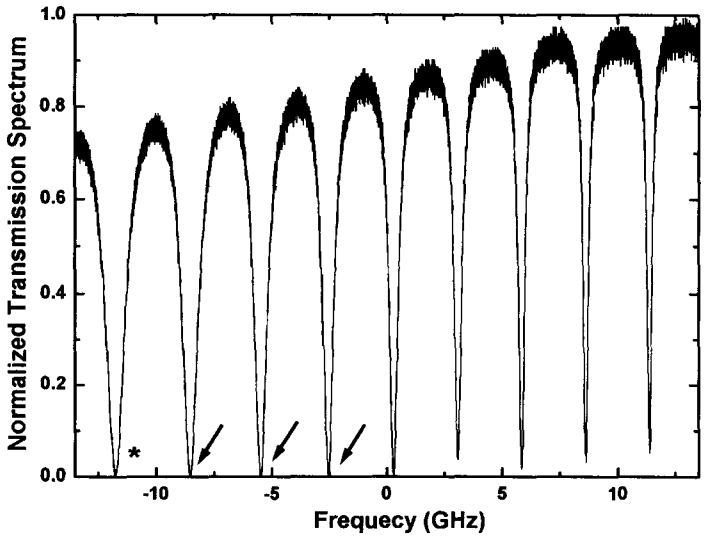

Figure 5.8 Normalized transmission spectra for the dual-taper coupling configuration. The resonance marked with an asterisk has a coupling efficiency greater than 99.8%. Those marked with arrows have power transfer efficiencies in excess of 99%.

To unveil the nature of the symmetrical TRT coupling structure, we redraw κ_1^2, κ_2^2 and β_1^2, β_2^2 in the same plot as shown in Fig. 5.10. Since the coupling condition of the input fiber taper is believed to remain nearly unchanged in our experiments, κ_1^2 and κ_2^2 should be nearly equal for each resonance under both single- and double-coupling conditions. The calculated results in figure 5.10 confirm this assertion, and consequently, β_1^2 and β_2^2 are easily determined in two respective cases.

Ideally, the loss coefficient β_2^2 in the case of dual-taper coupling will be the simple combination of β_1^2 and κ''^2 (assuming that the coupling of the output

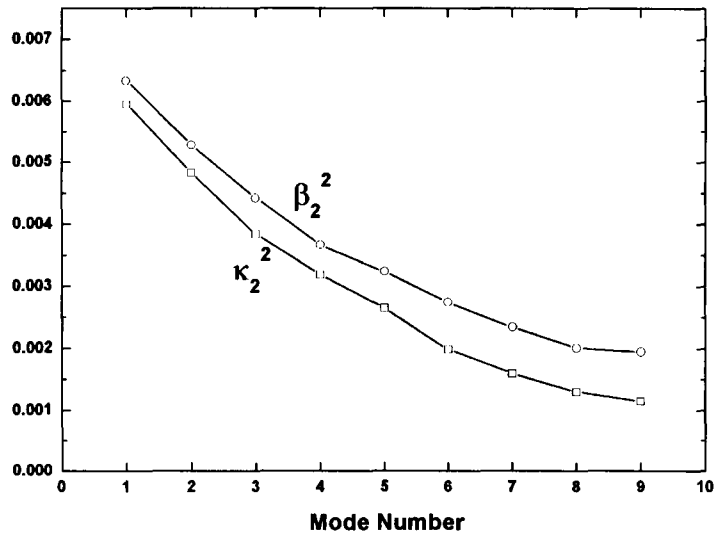

Figure 5.9 Calculated coupling coefficient κ_2^2 and total cavity loss β_2^2, corresponding to the spectrum shown in Fig. 5.9.

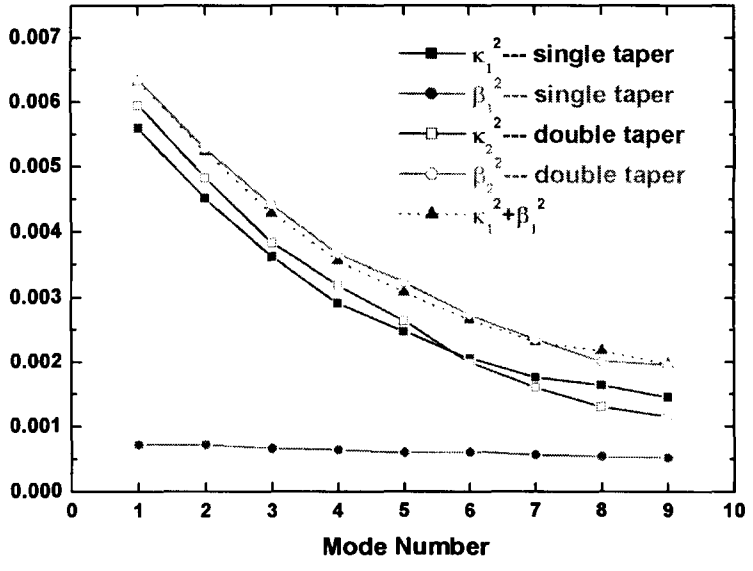

Figure 5.10 Calculated coupling coefficient κ_1^2, κ_2^2 and total cavity loss β_1^2, β_2^2, corresponding to the spectrum shown in Fig. 5.6 and 5.9. For comparison, $\kappa_1^2 + \beta_1^2$ was plotted in solid triangle points connected by a dashed line. The close agreement between $\kappa_1^2 + \beta_1^2$ and β_2^2 shows that the second coupler is nearly identical to the first coupler.

fiber does not introduce any significant additional loss aside from the coupling loss κ'^2). We fit β_2^2 using β_1^2 and κ_1^2, and the fact that $\beta_2^2 \approx \beta_1^2 + \kappa_1^2$ (the solid triangle points connected by a dashed line as shown in figure 5.10) indicates that the output fiber exhibits a nearly identical coupling coefficient for each resonance as the input fiber. This fact also shows that the second coupler introduces minimal scattering loss to radiation modes. The microsphere resonator is therefore under nearly symmetrical coupling conditions in the double-taper coupling system.

The symmetrical coupling structure plays an important role in obtaining the nearly critically coupled resonances. From Fig. 5.6, the intrinsic loss β_1^2 was observed to be nearly independent of the mode index and to remain very small. In our experiments, β_1^2 was approximately three to ten times smaller than the coupling coefficients κ_1^2 of the observed modes in the single taper geometry. The dual coupling case, however, is quite different. The output coupler introduces a mode dependent loss to the resonant modes that tends to track the coupling through the first taper. Therefore, as shown in the spectrum of the dual coupling case (Fig. 5.8), the critical coupling condition can be nearly satisfied for a wide range of modes. Furthermore, since the additional loss mainly comes from coupling to the taper mode (not scattering), the high fiber-to-fiber coupling efficiencies has also been observed.

We repeated the same experiments for various sized spheres in a range from $300\ \mu m$ to $30\ \mu m$ in diameter. Greater than 99% power transfer was routinely observed in the dual-coupling configuration. Using a microsphere having a

diameter of about $30\ \mu m$, the linewidth of a resonance was measured to be $15\ GHz$ under the dual-coupling condition. The coupling efficiency, however, remained as high as 99.3%. The resonantly transferred power to the second fiber was about 85% of the power transmitted through the first fiber in the non-resonant condition. This result shows the potential of the dual-coupling configuration as an add/drop filter for telecommunication applications in which high extinction, high drop efficiency, and a bandwidth of several gigahertz are required.

Bibliography

[1] M. Cai, O. Painter and K. Vahala, "Observation of Critical Coupling in a Fiber Taper to Silica-Microsphere Whispering Gallery Mode System," *Physics Review Letters*, vol. 85, pp. 74-77, 2000.

[2] M. Cai and K. Vahala, "Highly Efficient Optical Power Transfer to Whispering Gallery Modes Using a Symmetrical Dual-Coupling Configuration," *Optics Letters*, vol. 25, pp. 260-262, 2000.

[3] G. Hunziker, P. Bridger, M. Cai, and K. Vahala, patent application.

Chapter 6

Applications Towards Channel Add/Drop Filters

6.1 Introduction

An enormous amount of bandwidth capacity is required to provide the services demanded in the information age due to the proliferation of data-intensive applications, such as the internet and telecommunications. Wavelength division multiplexing (WDM) is a proven solution for addressing the bandwidth bottleneck. A WDM system utilizes the tremendous bandwidth of an optical fiber and multiplexes many independent channels modulated with their own data onto a single fiber, thereby give an n-fold increase in throughput of data. Add/drop filters that access one channel of a WDM system without disturbing other channels are very important components that allow networks architects more flexibility in designing systems. Figure 6.1 (a) and (b) illustrate the drop and add

functions, respectively. A WDM signal is introduced at port #1. A designed wavelength (in this case wavelength λ_3) is dropped and output through port #3. The remaining wavelengths are output through port #2. A vacant wavelength slot is filled by input of a signal on wavelength λ_3 at port #4. Although shown separately, the adding and dropping functions can be performed simultaneously.

Desirable properties of such an optical filter are listed below:

1. Low insertion loss for both the throughput channels and the dropped (or added) channel;
2. Little or no cross-talk between channels (meaning high extinction of dropped channel and high rejection of throughput channel);
3. Polarization insensitivity;
4. Low cost manufacturability (cost effectiveness);
5. Ease of integration, especially fiber optic compatibility;
6. Ideally wide tunable range to enable selection of a large number of channels, etc.

There are now several different technical approaches for realization of an add/drop device. Resonantly coupled waveguides based on dielectric micro-cavities have recently received considerable attention for possible applications as such devices. Monolithic devices based on coupling of waveguides via a microring (or disk) [1-2] resonator have been recently demonstrated by semiconductor nano-fabrication technology. However, this approach requires fiber-to-chip coupling,

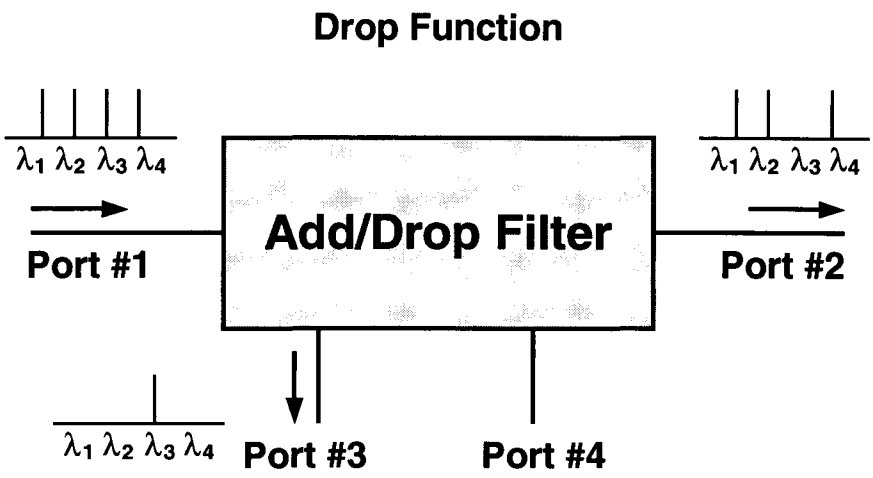

(a)

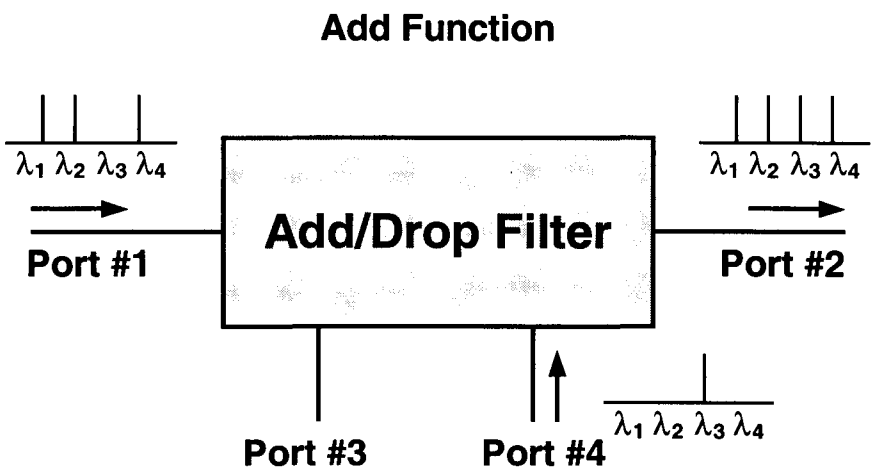

(b)

Figure 6.1 (a) Illustration of the drop function in an add/drop filter. The channel at wavelength λ_3 is shown being dropped in the schematic. (b) Illustration of the add function in an add/drop filter. A vacant channel slot at λ_3 is filled by input at port #4.

adding cost as well as insertion loss to the device. Other disadvantages include the radiative bending losses due to the low index contrasts and the parasitic optical loss induced by scattering from imperfections at the lithographically defined interfaces. In this chapter, we propose another potential approach to utilize the double taper symmetrically coupled microsphere resonator as an all-fiber four-port add/drop device, and demonstrate exceptional performance improvement especially upon properties of high extinction and low insertion loss [3, 4].

6.2 All Fiber Optic Microsphere Channel Add/Drop Devices

A typical schematic of the double taper coupled microsphere channel add/drop filter is shown in Fig. 6.2. Two nearly identical tapered fibers are positioned to tangentially touch opposite sides of an equator of the microsphere. The microsphere sustains whispering gallery mode resonances at a series of wavelengths $\{\lambda_i\}$. Careful positioning of the two fibers at the upper and lower taper-microsphere contact points enables coupling to these resonant modes. The four coupling ports are labeled as shown. If a signal containing several channels at wavelengths λ_1, λ_2, λ_3, λ_4... is input at port 1, then power transfer to the microsphere and to port 3 will occur for any input channel that is resonant with a whispering gallery mode (λ_3 in the figure). Other nonresonant channels travel through the upper fiber past the microsphere with minimal power loss. Similarly,

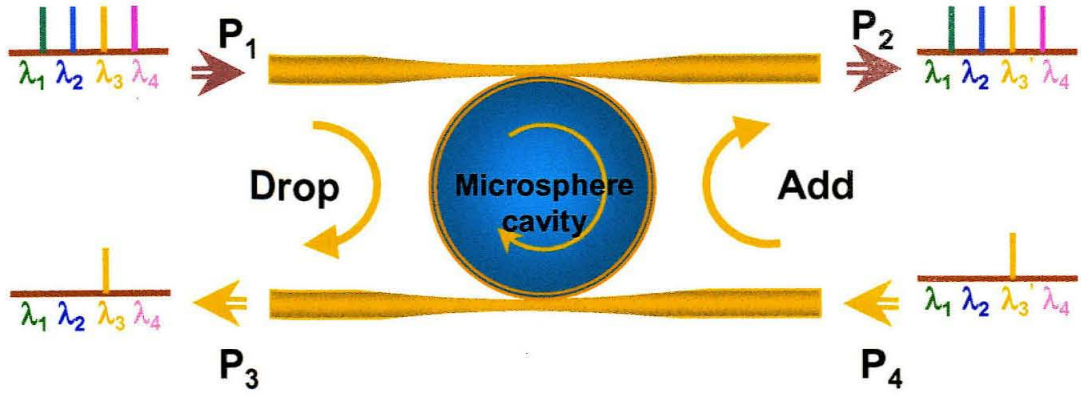

Figure 6.2 Schematic of the microsphere channel add/drop device showing a channel at wavelength λ_3 being dropped from port 3 while another channel at λ_3' is added from port 4.

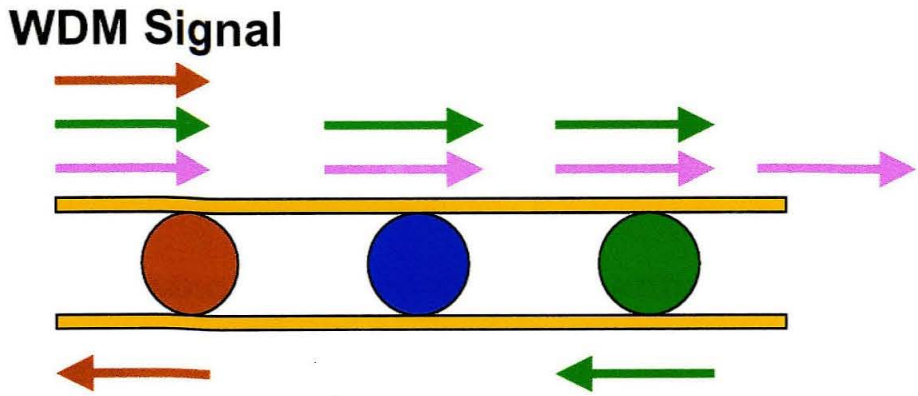

Figure 6.3 Ideal configuration of an optical add/drop multiplexer (OADM) based on a number of microsphere resonators coupling to two tapered fibers.

a channel input at port 4 that is resonant with a whispering gallery mode would be transferred to the upper fiber and would join the other channels at port 2. Channel adding and dropping therefore can be realized simultaneously.

An optical add/drop multiplexer (OADM) can be created by cascading a number of microsphere channel add/drop filter units. The ideal configuration for such an OADM is shown in Fig. 6.3. Each microsphere resonator is designed to be resonant at a particular channel wavelength and coupled by a pair of tapered fibers. When a WDM signal stream is launched into the upper fiber, the channel that is resonant with the microsphere will be transferred to the lower fiber through the microsphere. The add function can be fulfilled by inputting the signal from the other end of the lower fiber and joining the signal stream to the upper fiber through the microsphere. The OADMs with this configuration are easy to scale by changing the number of the microsphere resonators.

6.3 Performance of Microsphere Channel Add/Drop Filters

A magnified photograph of the top view of a microsphere channel add/drop filter is shown in Fig. 6.4. It consists of a $45\ \mu m$ fused silica microsphere and two nearly identical tapered fibers with diameters about $2 \sim 3\ \mu m$. The shadow on the background is the image of the glass stem that is used to support and manipulated the microsphere. Microspheres with diameters ranging from

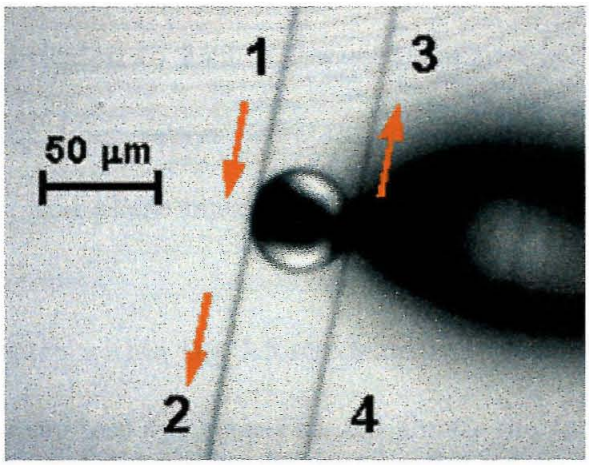

Figure 6.4 Photograph of the top view of the microsphere and double tapered fiber system. All components shown are fabricated from standard single mode fibers. The microsphere has a diameter of 45 μm and the waists of the two fibers are about $2 \sim 3$ μm. All ports have been numbered for reference.

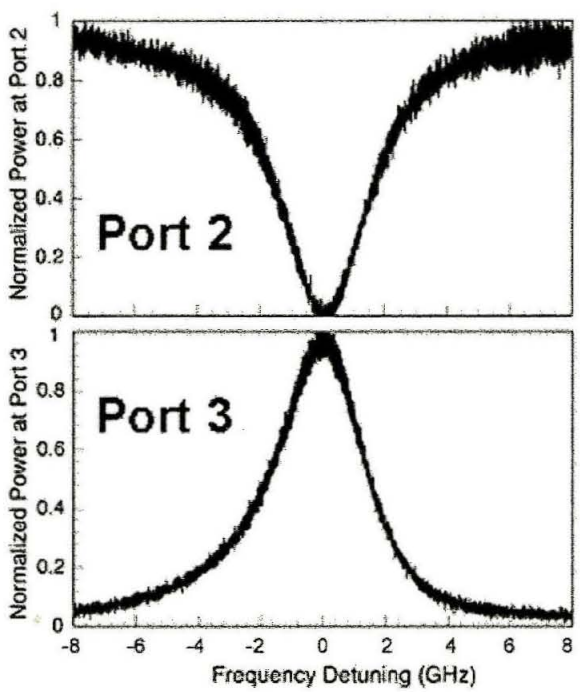

Figure 6.5 Transmission spectra measured simultaneously at both port 2 and port 3 for the add/drop device using a microsphere of 45 μm in diameter.

30 to 50 μm were fabricated to form a few systems to test as add/drop devices. The diameters of the fiber tapers were tailored carefully in order to provide nearly ideal coupling and phase matching between the fundamental modes in the microsphere and the tapers.

Transmission spectra within the 1.5 μm band were measured at ports 2 and 3 simultaneously for these test systems. Fig. 6.5 shows the transmission spectra of the device using the 45 μm diameter microsphere. The bandwidth (FWHM) of the resonance was about 3.8 GHz. The mode spacing of two adjacent modes was measured to be about 30 GHz (about 0.25 nm) by coarse tuning the laser wavelength (with a resolution of 0.01 nm). As high as 26 dB extinction ratio (defined as the ratio of the transmitted optical power at the resonant wavelength to that at a nonresonant wavelength at port 2) was obtained. We believe that higher extinction levels may be possible using better-matched fiber tapers.

The insertion loss of the dropped signal from port 1 to port 3 was approximately 3.2 dB, and the loss of the nonresonant optical power from port 1 to port 2 was approximately 3.1 dB. The taper loss for each coupler was measured at about 3.0 dB when the sphere was detached from the couplers. It is therefore reasonable to assume that the insertion losses of the device were dominated by the taper losses, which are believed to result from the sharp transition between the fiber-guided mode and the cladding-guided mode in the taper region. Note that after this work had been done, the taper pulling technique was greatly improved. We are now able to make tapers with loss as low as 0.2 dB routinely. Consequently, we believe the insertion loss of the

microsphere channel add/drop filters can be lowered to be less than 0.3 dB for both the throughput and dropped channels.

We evaluated the quality of the dropped signal at port 3 for data transmission purposes. Bit-error-rate (BER) measurements at different bit rates were performed for the couplers using different microspheres. Fig. 6.6 shows the experimental setup. The external cavity laser source was tuned to the central wavelength of a resonance to give the maximum power transfer from port 1 to port 3. The laser power was modulated with a $2^{15}-1$ bit PRBS from the BER tester using an external Mach-Zehnder modulator and then boosted by an erbium-doped fiber amplifier (EDFA) before launching into port 1 of the device. The receiver consisted of a low-noise EDFA preamplifier, optical band-pass filters and a high-speed photodetector. Fig. 6.7 shows the BER curves obtained for the dropped signal resonantly coupled from port 1 to port 3 through the 45 μm microsphere. The power penalty was less than 2 dB at a bit rate of 5 Gbit/s. No penalties were observed at a modulation rate of 2.5 Gbit/s or below. There was also no sign of an error-rate floor at either bit rate. The eye patterns at both bit rates are also shown as insets in Fig. 6.7. The experimental results obtained using other sizes of microspheres exhibited similar BER performance except that the maximum bit rates varied depending on the exact resonance bandwidth.

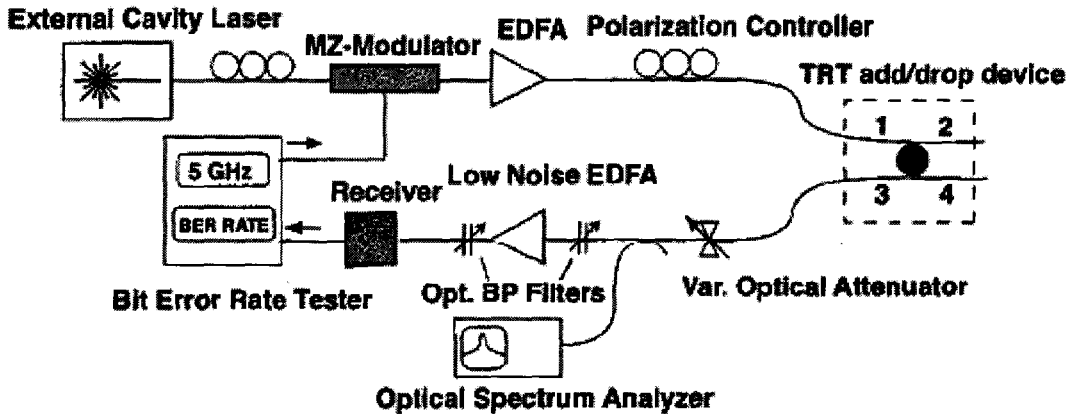

Figure 6.6 BER experimental setup

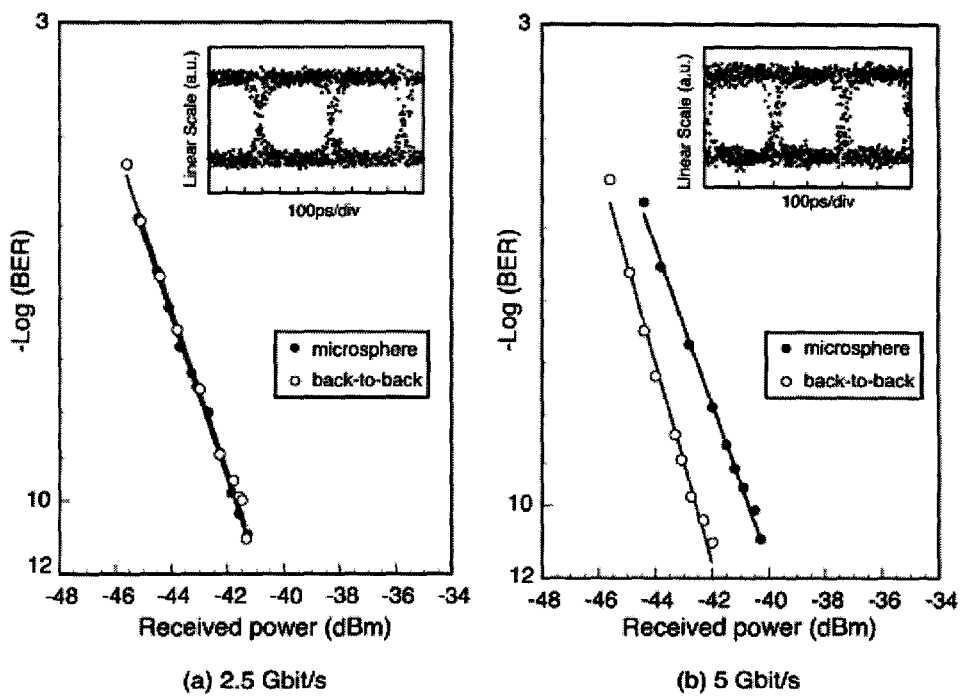

Figure 6.7 BER performance of an add/drop filter using a 45 μm diameter microsphere at (a) 2.5 Gbit/s and (b) 5 Gbit/s, respectively. The eye patterns in both cases are shown as insets.

6.4 Discussion and Conclusion

In consideration of practical application to WDM systems, the all-fiber microsphere-resonator-based add/drop devices have shown promising characteristics including high extinction ratio (> 26 dB), low insertion loss (< 0.3 dB), appropriate channel bandwidth (several gigahertz), fiber optic compatibility, and compact dimensions. Additionally, BER performance is satisfactory at OC48 rates.

There still remain significant technical challenges, however, before these devices can be considered seriously for applications. The adjacent resonant mode spacing should be increased substantially. Several-terahertz separation would be desirable to enable single-channel selection by one device. This problem might be solved by using highly eccentric spherical structures or even cylindrical structures such as fiber ring or disk resonators. Furthermore, wavelength tunability, thermal stability, and polarization dependence are all interesting topics for future work.

Bibliography

[1] B. E. Little, S. T. Chu, H. A. Haus, J. Foresi, and J. P. Laine, "Microring Resonator Channel Dropping Filters," *Journal of Lightwave Technology*, vol. 15, pp. 998-1005, 1997.

[2] B. E. Little, J. Foresi, H. A. Haus, E. P. Ippen, W. Greene, and S. T. Chu, "Ultra-Compact Si/SiO2 Micro-Ring Resonator Channel Dropping Filter," *IEEE Photonics Technology Letters*, vol. 10, pp. 816-818, 1998.

[3] M. Cai, P. O. Hedekvist, A. Bhardwaj, and K. Vahala, "5 Gbit/S BER Performance on an All Fiber-Optic Add/Drop Device Based on a Taper-Resonator-Taper Structure," *IEEE Photonics Technology Letters*, vol. 12, pp. 1177-1179, 2000.

[4] M. Cai, G. Hunziker, and K. Vahala, "Fiber-Optic Add/Drop Device Based on a Silica Microsphere-Whispering Gallery Mode System," *IEEE Photonics Technology Letters*, vol. 11, pp. 686-687, 1999.

Chapter 7

Applications Towards Microsphere Lasers

7.1 Introduction

Whispering gallery modes in glass microspheres exhibit unique properties of extremely high quality factors (up to 10^{10}) [1] and very small mode volumes (in the order of 100 μm^3). Strong confinement of light in both time and space makes the microsphere systems very attractive as resonant cavities for laser oscillation, where very low threshold and high pump efficiency are expected. Furthermore, with the fiber taper coupling scheme we have introduced in previous chapters, these microsphere lasers are fiber compatible with telecommunication systems and might be used as seed laser sources.

Initial work on neodymium-doped glass microsphere lasers at 1.08 μm [2] was explored using prism couplers. Pump threshold as low as 200 nW was

demonstrated; however, the laser was in multimode operation, and the output laser power was in the order of 100 pW. Other efforts on glass microsphere lasers with different dopants, such as erbium-doped ZBLAN (lasing at 1.56 μm [3] or up conversion at 0.54 μm [4]), exhibited similar laser characteristics of multimode oscillation and low pump efficiency.

In this chapter, we demonstrate a low threshold erbium/ytterbium co-doped phosphate microsphere laser that is coupled by a single fiber taper and oscillates at single frequency in the 1550-nm band [5]. With an improved hybrid taper coupler, up to 110 μW output laser power and 12% pump quantum efficiency are measured [6]. The theoretical analysis of the laser threshold, the resonantly coupled pump ring modes, as well as the reason of employment of hybrid taper couplers are also provided.

7.2 Microsphere Laser Characteristics

7.2.1 Erbium:Ytterbium Co-Doped Phosphate Glass

Since erbium ions in glass hosts are the material of choice to provide laser emission in the optical spectrum of $1.5-1.6\,\mu m$, which is favored by telecommunication applications, we used Kigre QX/Er phosphate glass that is heavily doped with erbium (0.5% by weight) and ytterbium (20% by weight) to fabricate microspheres. Fig. 7.1 shows a simplified energy level diagram of the erbium:ytterbium laser system and the processes of main interest for pumping in

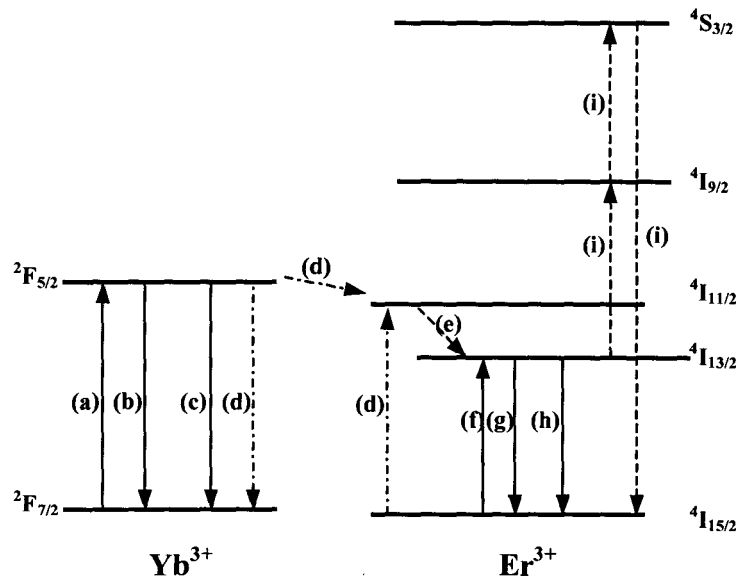

Figure 7.1 Energy level diagram of the erbium:ytterbium system. The solid-line arrows refer to radiative phenomena, the dashed-dot arrows to erbium:ytterbium energy transfer process and the dashed arrows to non-radiative transitions.

the 980 nm band and for laser action in the 1550 nm band. A complete description of these processes is provided in Ref. [7] and references therein. Listed below are those processes crucial for understanding the laser characteristics in the microspheres:

(a) and (b): radiative absorption and emission of a pump photon from the $F_{7/2}$ and $F_{5/2}$ ytterbium levels, respectively.

(d): the Yb to Er transfer process that acts as indirect pumping of Er ions.

(f) and (g): stimulated emission and absorption between $I_{13/2}$ upper and $I_{15/2}$ ground Er laser levels. The fluorescence lifetime of the $I_{13/2}$ level is about 10 ms.

(i): cooperative up-conversion (UC) process between two excited Er ions that promotes one ion to the upper levels ($I_{9/2}$, $S_{3/2}$, etc.) while the second ion decays

to the ground level. At room temperature, a green emission at 540 nm is routinely observed due to the spontaneous emission of the up-converted erbium ions to the ground state ($S_{3/2} \rightarrow I_{15/2}$).

The absorption of the Kigre QX/Er glass due to the $F_{5/2} \rightarrow F_{7/2}$ transition of the Yb^{3+} ions is strongly peaked around 976 nm (±5 nm). The $F_{7/2}$ level of Yb^{3+} is resonantly coupled to the Er^{3+} $I_{11/2}$ level, which then relaxes to the $I_{13/2}$ level. The 1.5 μm lasing transition is between the ground state $I_{15/2}$ level and the $I_{13/2}$ excited state level of Er^{3+}. The specification of the Kigre QX/Er phosphate glass sample is listed below [7,8]:

QX/Er sample: 0.8% Er_2O_3 and 20% Yb_2O_3

($n_{Er} = 7.3 \times 10^{19}$ cm^{-3} and $n_{Yb} = 1.5 \times 10^{21}$ cm^{-3})

Center lasing wavelength (nm)	1535
Stimulated emission cross section σ_{Er} (x 10^{-20} cm^2)	0.8
Loss at 1535 nm δ_{Er} (% cm-1)	0.02
Center pump wavelength (nm)	796
Absorption cross section σ_{Yb} (x 10^{-20} cm^2)	1.05
Fluorescence lifetime τ_{Er} (ms)	7.9
Index of refraction at 1.535 nm n_s	1.521
Transformation temperature (°C)	450
Softening temperature (°C)	485

Fabrication of the phosphate glass microspheres in our experiments followed the instructions in Chapter 4. The sizes of the microspheres ranged from 40 to 100 μm. The eccentricity of the spheres was measured by analyzing the resonant mode structure at 1.5 μm, and it usually fell into the range from 1% to 3%.

The microsphere lasers were coupled using tapered fibers as one can expect. Tapers were fabricated using 1550 nm single mode fibers (SMFs) under the adiabatic criterion (see Chapter 3), and the waists were tailored to be approximately $1.5 \sim 2\ \mu m$ in order to obtain phase matching between the fundamental taper mode and the sphere modes.

7.2.2 Typical Microsphere Laser Performance

In this section, we demonstrate a typical fiber taper coupled microsphere laser and the experimental results on its basic performance. The physical interpretation of the laser characteristics and a series of interesting phenomena associated with the microsphere laser will be addressed in the next section.

In our experiment, a 1.5 μm wavelength microlaser was formed by placing a single tapered fiber into contact with an Er:Yb doped phosphate glass microsphere. The microsphere had a diameter of 57 μm and the taper waist was approximately 1.75 μm. The fiber taper served as an efficient input and output coupling port that guided the pump wave to the surface of the microsphere, coupled the pump into the sphere, and then collected the resulting laser emission. Fig. 7.2 shows a photograph of the taper-microsphere laser system.

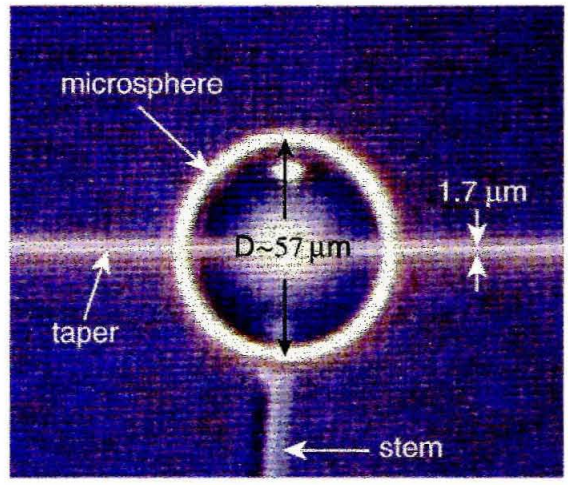

Figure 7.2 Image of a fiber taper coupled microsphere laser.

The pump wave in this experiment was launched from a 980 nm wavelength, narrow-linewidth (<300 kHz), tunable external-cavity laser into the fundamental mode of the fiber taper. The tuning range of the pump laser is from 967 nm to 986 nm. By scanning the wavelength of the pump source, the transmission response was measured at the output end of the taper coupler, as shown in Fig. 7.3. This spectrum looks very different from what we have seen in passive (high-Q) silica microsphere. There are a number of interesting features, which we will discuss in the next section. Here, however, it is necessary to point out that the pump wave was resonantly coupled into the cavity as pump sphere modes, which was further confirmed by the image of the photoluminescence at the green wavelength 540 nm, which corresponds to the spontaneous emission of the up-converted erbium ions ($S_{3/2} \rightarrow I_{15/2}$). The green emission, although lowering the

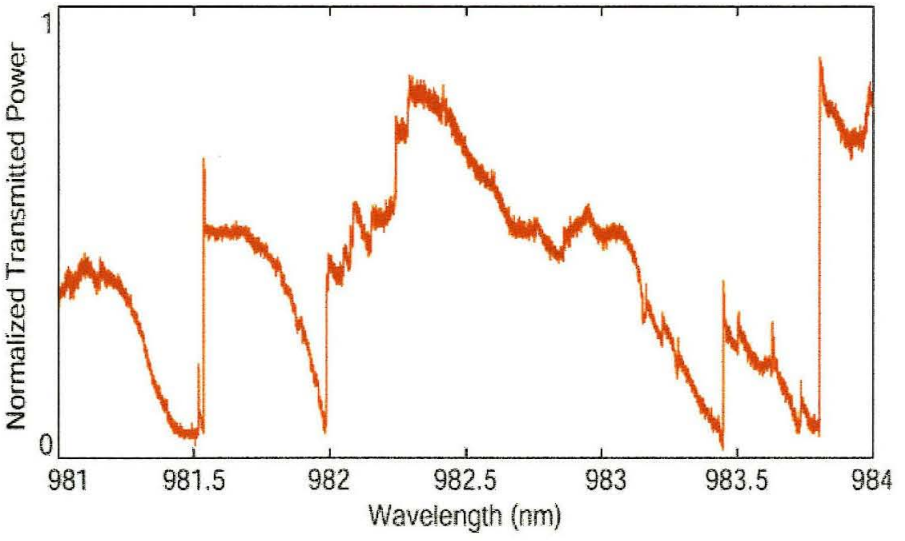

Figure 7.3 Pump transmission spectrum of a fiber taper coupled microsphere laser.

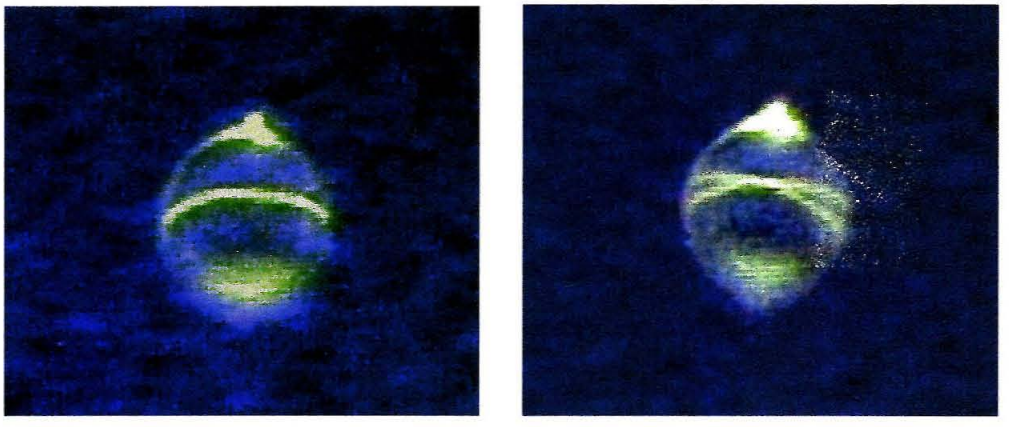

(a) (b)

Figure 7.4 Pictures of green emission of the microsphere laser with (a) single ring and (b) crossing rings.

pump efficiency, indicates the path taken by the 980 nm pump wave within the sphere. Fig. 7.4 (a) and (b) show pictures of the signature green emission in the microsphere laser when pumped at different wavelengths. In Fig. 7.4 (a), the

single ring encircling the equator of the sphere suggests that the pump wave was coupled to a fundamental sphere mode ($m = l$), while the two crossing rings with the normal inclined to the symmetrical axis of the system implies that the pump wave was coupled to sphere modes with $m \neq l$ $(m < l)$. The spatial distribution of the pump modes defines the active gain region and provides a potential mechanism of wavelength selection for the laser cavity. This is because only those laser modes that have maximum spatial overlaps with the pump modes can first achieve enough gain to initiate the lasing. In general, a fundamental pump mode is most likely to excite a fundamental laser mode. Further understanding of the ring modes of the pump wave will be investigated in the next section.

Beside the pump spatial selectivity, there exist many other factors contributing to the laser operation in the microsphere, such as the loading of the sphere due to the taper, the broad homogeneous gain spectral bandwidth and variation in emission and absorption cross-sections versus wavelength in the phosphate material. Depending on the gain region within the sphere, lasing occurred at wavelengths ranging from 1520 to 1560 nm in both multimode and single-mode fashion. By adjusting the taper contact position on the sphere and the pump wavelength, we were able to switch between multimode and single-mode lasing action. The single-mode lasing is most likely obtained by tuning the pump wavelength to a fundamental whispering gallery mode resonance that produces a narrow equatorial-ring gain region.

A typical single-mode lasing spectrum (as collected by the taper) for an

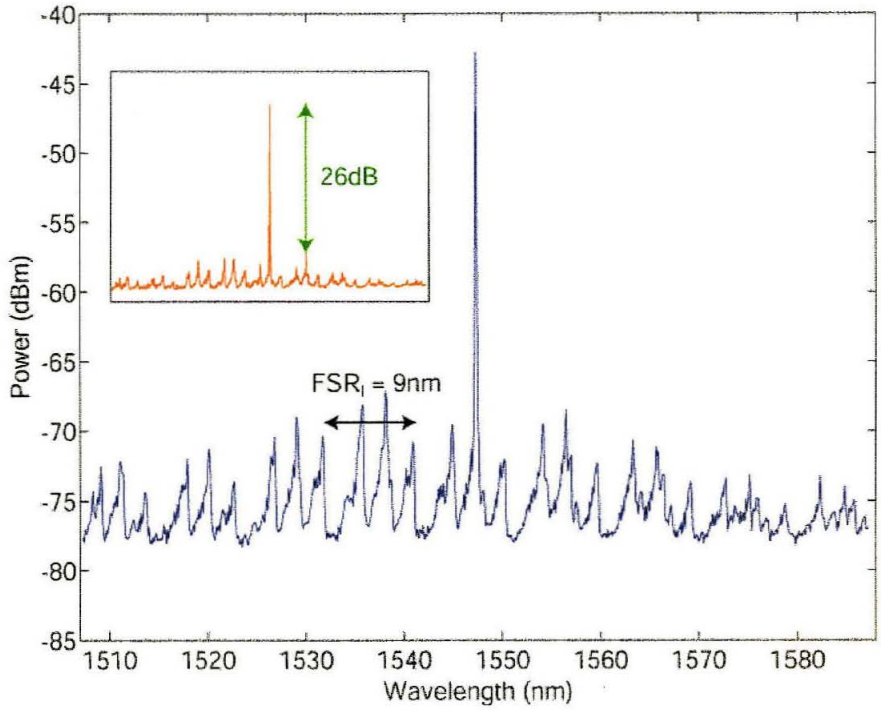

Figure 7.5 Photoluminescence spectra of the microsphere for an annular pump region about the equator. The inset shows the side-mode suppression is 26 dB.

equatorial-ring pump region is shown in Fig. 7.5. To resolve the fine spectral features of the laser (different m modes) we used a high-finesse (about 5,000) scanning Fabry-Perot cavity with a spectral resolution of a few megahertz to obtain the spectra shown in the inset of Fig. 7.5. The microsphere was found to lase on a single m whispering gallery mode over the entire pump range depicted in Fig. 7.5. In previous fused-silica microsphere laser experiments [2-4], laser emission in a multimode regime was generally observed. Further explanation of the single-mode lasing nature in our experiment will be addressed in the next section.

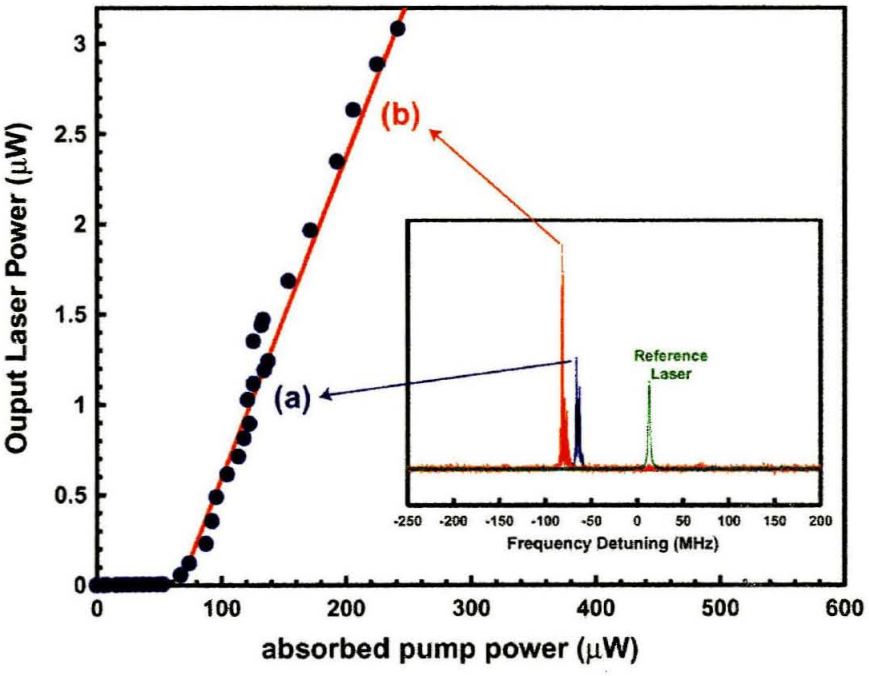

Figure 7.6 Collected laser output power versus absorbed pump power in the microsphere ($L_{out} - L_{in}$). The inset, spectral output from a Fabry-Perot spectroscopy, showing the single-mode nature of the microsphere laser, where for reference a single-frequency laser with a known linewidth of 300 kHz is also shown.

A plot of the laser power collected in the taper versus the total pump power absorbed and scattered by the presence of the sphere ($L_{out} - L_{in}$) is shown in Fig. 7.6. The lasing threshold is estimated at $60\ \mu W$, and the laser reaches an output power of $3\ \mu W$ while retaining single mode operation. A collected power as high as $10\ \mu W$ was obtained in a single line at higher pump power, although the laser was multimode at that point. The differential quantum efficiency, which is defined as

$$\eta = \frac{P_{laser}}{P_{pump} - P_{th}} \frac{\lambda_{laser}}{\lambda_{Pump}} \tag{7.1}$$

was measured to be about 2.6%.

As we use the same taper to couple in the 980 nm pump power as that used to couple out the 1.5 μm laser power from the sphere, and we designed the taper for phase matching at the pump wavelength to reduce the lasing threshold, the laser emission is not optimally collected by the taper (as the higher-order taper modes will be radiated away before reaching the detector). In the last section of this Chapter we will propose a few methods to improve this situation. Among them, a novel coupling technique, so called hybrid taper coupler, will be highlighted and the experimental results on the hybrid fiber taper coupled microsphere laser are to be presented.

The phosphate glass microsphere laser that we studied here was also found to be self-pulsing under these pump conditions, with a period of roughly 15 μs and a pulse width of 500 ns. The peak single frequency output power from the microsphere laser is thus about 36 μW.

7.3 Interpretation of the Lasing Action

In this section, we review many interesting phenomena associated with the microsphere lasers and try to give them physical explanations.

7.3.1 Estimation of the Laser Threshold

For the microsphere laser we studied in previous section, the lowest possible threshold can be estimated by calculating the total cavity loss per round trip L_{oss}. The computation will be carried for the fundamental laser mode only. Additionally, assume the fundamental mode is located along the equatorial circle, and the diameter of the circle is approximately equal to the microsphere diameter D_s (= 57 μm). The lasing wavelength of the microsphere laser was around 1547 nm. For simplification, however, data at the sample's peak wavelength, 1535 nm, are used for the estimation. The results can be scaled to other wavelengths by replacing parameters appropriate for other wavelengths.

From the specification of the Kigre QX/Er phosphate glass sample [7, 8], the intrinsic loss at peak wavelength 1535 nm is about $0.02\%\, cm^{-1}$. This gives an intrinsic cavity loss per round trip

$$\begin{aligned} \beta_{\mathrm{Er}}{}^2 &= 3.58\times10^{-6} \\ \alpha_{\mathrm{Er}}{}^2 &= 1-\beta_{\mathrm{Er}}{}^2 = 0.9999964, \end{aligned} \tag{7.1}$$

where α^2 and β^2 have the same definition as they first introduced in Chapter 3. Therefore, the cold (unloaded) cavity has an intrinsic quality factor as high as 5×10^7.

Beside the intrinsic cavity loss, the laser power coupling from the sphere to the taper has also to be counted as a part of the total cavity loss. In our case, the phase matching between the taper and sphere modes was optimized for the pump wave, and consequently the coupling strength at the laser wavelength was relatively small. In general, under the condition that the sphere and the taper are

in physical contact and phase matched, the coupling coefficient κ^2 is usually in the range of $0.5\% \sim 1\%$ [10], hence we can reasonably assume that the coupling coefficient at the laser wavelength $\kappa_{Er}{}^2$ is approximately 0.1%, corresponding to a transmission coefficient $t_{Er}{}^2$ of 0.999. Note that the microsphere laser supports traveling waves of the laser emission in both clockwise and counterclockwise directions, the total coupling loss is thus given by $2\kappa_{Er}{}^2 \approx 0.2\%$ (assume almost equal coupling strengths in both directons). The coupling-induced cavity loss is much larger than the intrinsic cavity loss as given in Eq. (7.1), and consequently determines the microsphere laser threshold.

The laser threshold is defined as the least pump power required for a laser system to obtain enough gain to overcome the total cavity loss. The laser threshold condition requires

$$g_{th} \cdot L_{oss} = 1, \tag{7.2}$$

where g_{th} and L_{oss} are the threshold gain and total cavity loss per round trip, respectively. From the cavity loss analysis above, we obtain

$$L_{oss} = (1 - 2\kappa_{\mathrm{Er}}{}^2)\,\alpha_{\mathrm{Er}}{}^2 = 1 - 2.0036 \times 10^{-3} = 1/\,g_{th}. \tag{7.3}$$

Therefore, the population inversion density at the threshold is

$$\Delta n_{th} = \ln(g_{th}) \Big/ (\sigma_{\mathrm{Er}} \cdot \pi \mathrm{D_s}) \approx 1.4 \times 10^{19}\ cm^{-3} \tag{7.4}$$

and the threshold pump power is inferred to be

$$P_{th} = \Delta n_{th} V_p h\nu_p \Big/ (\alpha \tau_{Er}) \approx 1\ \mu W, \tag{7.5}$$

where $h\nu_p$ represents the energy of a single pump photon, $\tau_2 \approx 7.7\ ms$ is the total decay rate of the excited level ($I_{11/2}$) of the lasing transition [11], and $\alpha \approx 0.5$ is the estimated efficiency of the pumping mechanism ($Yb{:}F_{7/2} \rightarrow Yb{:}F_{5/2} \rightarrow Er{:}I_{11/2} \rightarrow Er{:}I_{13/2}$) [11], V_p is the pump mode volume. By measuring the volume occupied by the grean up-conversion emission, the pump mode volumn is estimated to be approximately $(3\lambda_p)^2 \cdot \pi D_s \approx 1550\ \mu m^3$.

Since the variation of the total cavity loss with wavelength is generally negligible, the threshold pump power is proportional to $1/\sigma_{Er}$. For laser wavelengths other than the peak wavelength 1535 nm, for example, at 1547 nm, the threshold pump power is increased to be about $2\ \mu W$ since the emission cross section at 1547 nm is almost a half of the value at the peak wavelength 1535 nm.

Note that in our experiment, the absorbed pump power at the threshold was measured to be about $60\ \mu W$, which is much larger than the theoretical expectation. We attribute this to several factors.

First, in the real system the absorbed pump power by the microsphere is also shared by many processes other than the lasing transition. Such processes include strong up-conversion emission, excited state absorption (ESA), impurity scattering and radiative loss, etc.

Secondly, the laser mode and the pump mode are actually not completely overlapped because the laser mode is more spread out (due to longer wavelength) and more importantly, the laser mode has much longer lifetime (higher Q) than that of the pump mode such that they are evolving in totally different manners, for which we have more detailed explanations in the next part.

Thirdly, the 1550 nm single-mode fiber taper doesn't actually serve as an optimal pump coupler, because it is a multimode waveguide for the pump wave, which has a wavelength (980 nm) shorter than 1550 nm. In other words, there exists a higher order pump mode coupling, which is not favored for the fundamental laser mode. We will further investigate this issue and propose possible solutions in the last section of this chapter.

Fourthly, we believe the intrinsic cavity loss of the phosphate microsphere is increased significantly after the fabrication. This is because the phosphate glass is very easy to crystallize into clusters during the cooling procedure of the fabrication, which is of course undesirable and cause excess scattering loss.

Finally, the measurement of the absorbed pump power is limited by the difficulty of accurately defining the small difference of the pump power through the fiber coupler with and without sphere coupling. This problem can be solved by developing a more sophisticated measuring method.

7.3.2 Resonaut pumping into the microsphere

In this section, we will develop an explicit picture of the resonant pumping into the microsphere. It is shown that such a picture is of great importance for us to understand the physics of the laser behavior in the microsphere laser.

We first look at the excitation of whispering gallery modes in a real (i.e., slightly aspherical) microsphere resonator.

The electrical field of the whispering gallery modes inside a microsphere can be approximately expressed as (see Chapter 2)

$$\begin{cases} E_\theta(r,\theta,\phi) \sim -\dfrac{kn_s m}{\sin\theta} j_l(kn_s r) Y_l^m(\theta,\phi) & \text{TE modes} \\ E_r(r,\theta,\phi) \sim \dfrac{l(l+1)}{r} j_l(kn_s r) Y_l^m(\theta,\phi) & \text{TM modes.} \end{cases} \tag{7.6}$$

Here we pay special attention to the angular dependence of the field, which is represented by the spherical harmonics $Y_l^m(\theta,\phi)$ and study the establishment of the spherical modes as well as the index m-dependent frequency splitting in the spherical resonators.

It has been shown in terms of the semiclassical picture that an arbitrary spherical function $Y_l^m(\theta,\phi)$ in a slightly eccentric sphere can be modeled as a result of precession of inclined fundamental circular mode $Y_l^l(\theta,\phi)$ [12, 13], as illustrated in Fig. 7.7.

In a perfect spherical resonator, each m-index whispering gallery mode has the same perimeter length and thus is spectrally $(2n+1)$ degenerate. The mode field has the same distribution as $Y_l^l(\theta,\phi)$ except the distinct orientation along the angle $\theta_{l,m} = \cos^{-1}(m/l)$ with respect to the symmetry axis of the sphere z. The mode propagating along the great circle would not precess because of the symmetry. If the sphere is slightly distorted (either prolate or oblate) with the eccentricity ε^2, however, after each evolution the mode will come to a shifted point at the equator, and therefore the orbit will in effect turn by a small angle. After a number of precession periods, a stationary field distribution is eventually

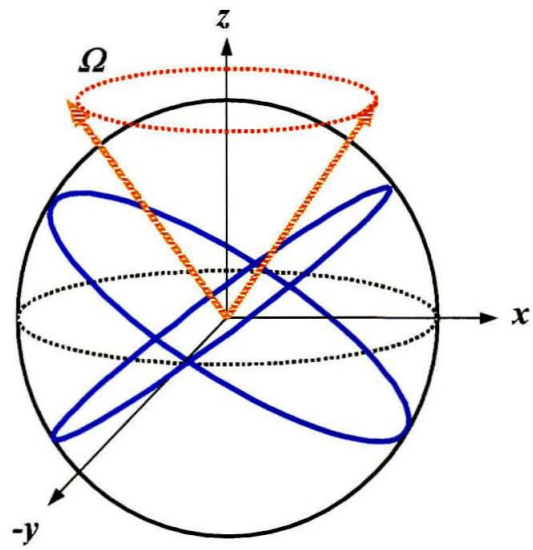

Figure 7.7 Illustration of whispering gallery mode precession in a slightly aspherical resonator.

formed, which is effectively identical to the undisturbed spherical hormonic $Y_l^m(\theta,\phi)$. Since the great circles of a sphere become great ellipses of a spheroid and each of them inclined at a different angle $\theta_{l,m}$ has a different perimeter length, each precessing resonant mode will have a different resonant frequency from the initial degenerate freqency.

Note that the precession evolution of the whispering gallery modes takes time. The precess frequency Ω is simply determined by the eccentricity of the sphere or the m frequency splitting, and can be approximately calculated by $\left|\omega_{l,m} - \omega_{l,l}\right|/m$ [12]. For a microsphere having a diameter of $57\ \mu m$ and eccentricity of about 2.4% [5], the precession frequency is in the order of tens of GHz at 1550 nm wavelength (about 1.5 times scaled down at 980 nm), corresponding a precession period of about 0.07 ns. Within one precession period,

the light will have traveled along the great circle 80 times. If the microsphere has a quality factor of 10^7, the photon lifetime is about 8 ns (at 1550 nm) or 5 ns (at 980 nm), which is long enough for the precessing mode to establish a steady orbit described by $Y_l^m(\theta,\phi)$.

The angular dependence $Y_l^m(\theta,\phi)$ of the whispering gallery modes suggests that the intensity pattern of a spherical harmonic with l, m mode numbers is an oscillating function in the $\hat{\theta}$ direction with two strong peaks at an angle of $\theta_{l,m} = \pm\cos^{-1}(m/l)$. Thus one would expect to see two rings symmetric about the equator with latitude given by $\theta_{l,m}$. This has been confirmed in Refs. [12, 14] for fused silica microspheres. In the phosphate glass microspheres, however, we see 980 nm wavelength pumping into semiclassical orbits as indicated by the green emission of single and crossing rings in Fig. 7.4.

To understand the pump coupling behavior, let's first calculate the quality factor of the phosphate glass microsphere at 980 nm. Note that the concentration of erbium ions is far less than that of ytterbium ions in the sample. It is reasonable to ignore the contribution of erbium ions to the pump absorption. Therefore, the pump absorption coefficient ($F_{5/2} \rightarrow F_{7/2}$ @ 976 nm) is given by $\delta_{Yb} = \sigma_{Yb} \cdot n_{Yb} \approx 15.75\ \text{cm}^{-1}$ (6840 dB/m), corresponding to a round trip loss coefficient $\beta_{Yb}{}^2 = 0.448$ and a quality factor of about 600! The 980 nm average photon lifetime is thus as short as 0.3 ps, which is comparable or less than the round trip traveling time for the photon ($= \pi n_s D_s / \lambda_p \approx 0.9$ ps), and not long enough for the 980 nm phone to even finish one circle of the round trip, not to mention the precession. This explains that pump wave is coupled into semi-

classical orbits other than the symmetrical two-peak patterns in the strong damping phosphate glass microsphere. One can also think of this phenomena as resulting from the broadening of the cold cavity $Y_l^m(\theta,\phi)$ states resulting in spectral overlap and excitation of a superposition of the true eigen-states.

It is also of great interest to observe the transition of the ring patterns as the pump wavelength varies. For comparison, we redraw Figs. 7.3 and 7.4 together into Fig. 7.8.

The pump transmission spectrum is interesting in itself. First, there appear many very sharp transitions in the transmission response. We attribute these jumps in transmitted power to discontinuities in the phase-matching of the taper mode and the excited whispering gallery mode. For fixed values of n and l, the different m valued whispering gallery modes span a significant wavelength range due to the eccentricity of the sphere. For a $TE(TM)_{n,l}$ set of WG modes, the magnitude of the azimuthal mode number, m, of the resonantly coupled whispering gallery mode scans from 0 to l as the pump wavelength is increased. Once the wavelength passes the $m = l$ whispering gallery mode, a new set of modes is addressed with different p, n or l. A jump in the transmission curve appears as a result of the rapid change in the input coupling strength (κ_p) due to phase-matching as the excited sphere mode transitions from a whispering gallery mode with $m = l$ to one with $m << l$.

As the pump wavelength is tuned, the coupling ring pattern changes accordingly as indicated in Fig. 7.8. The image in Fig. 7.8 (a) corresponds to the

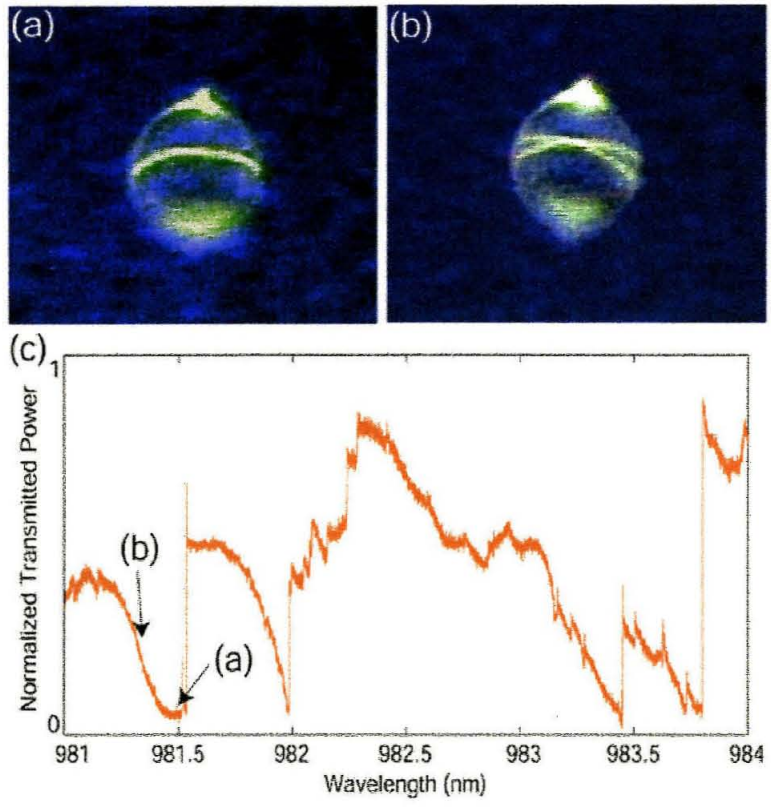

Figure 7.8 Color image of the green up-converted photoluminescence from the taper pumped microsphere. (a) the pump wavelength is tuned close to a fundamental whispering gallery mode ($m = l$). (b) the wavelength corresponds to a mode with $m < l$. (c) a pump band transimission spectrum of the taper-sphere system.

bottom of a transmission dip, just before a discontinuous transition point, and shows a micron sized ring encircling the equator of the sphere. This equatorial ring corresponds to resonant pumping of a whispering gallery mode with $m \approx l$. At pump wavelengths away from a transition point in the transmission curve, a crossing ring pattern is present on the sphere surface, as shown in Fig. 7.8 (b). The image in (b) was taken diametrically opposite the taper-sphere contact point, on the backside of the sphere. Imaging of the front side shows that the

rings re-cross at the contact region. The crossing angle of the rings tunes with wavelength, starting from large angles at peaks in the transmission and then smoothly closing to form a bright single equatorial ring at the bottom of a dip in the transmission plot. The evolution of the crossing rings follows exactly the peaks and valleys of the transmission plot at the bottom of Figure 7.8, strengthening the phase-matching argument made above, as the degree of phase-matching will vary as the cosine of the inclination angle of the rings.

Fig. 7.9 shows more pictures of these ring patterns at different pump wavelengths for a microsphere with a diameter of about $45\ \mu$m. The pictures were taken using an Apogee KX85 CCD camera, which has a resolution of a few nanometers. Fig. 7.9 (a) again is a typical fundamental whispering gallery mode, and Fig. 7.9 (b) shows two higher-order whispering gallery modes with large inclination angles, corresponding to $|l-m| \approx 10$. The image shown in Fig. 7.9 (c) is quite interesting because the two crossing rings were actually out of phase at the point that is diametrically opposite to the taper-sphere contact region. They interfered destructively and produced a very narrow dark gap that was captured by the high resolution camera. This pattern also confirms that the two rings were $\pm m$-index whispering gallery modes and couped symmetrically with equal strength.

However, it is not always the case. The pump power coupled into the ring modes could be influenced by many factors, such as the taper-sphere alignment, polarization states of the pump beam, the symmetry of the microsphere, etc. Fig.

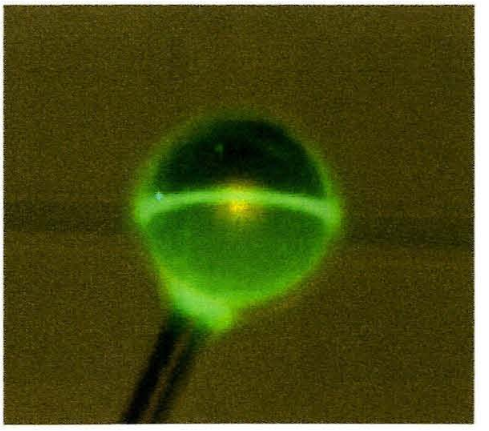

(a)

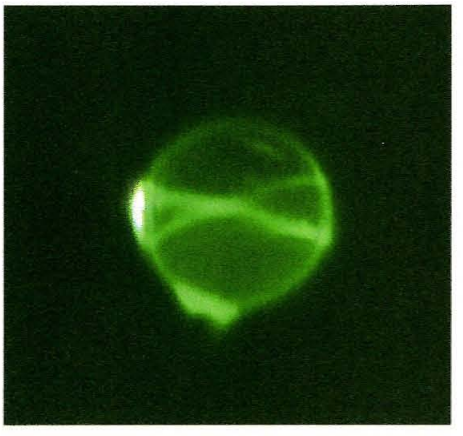

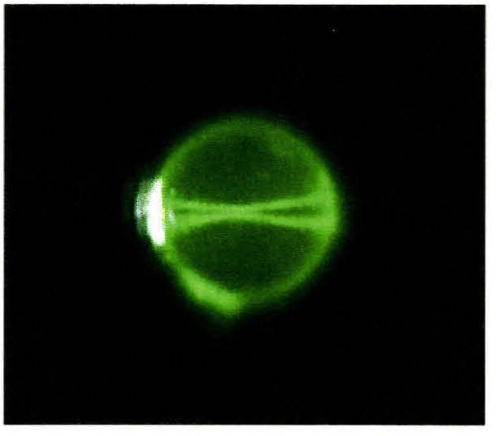

(b) (c)

Figure 7.9 More ring patterns as the pump wavelength varies. Pictures are taken with an Apogee KX85 CCD camera. (a) a fundamental whispering gallery mode ($m = l$). (b) two crossing rings with large inclination angles ($|l - m| \approx 10$). (c) two symmetrical ring modes destructively interfere at the point that is diametrically opposite to the taper-sphere contact region.

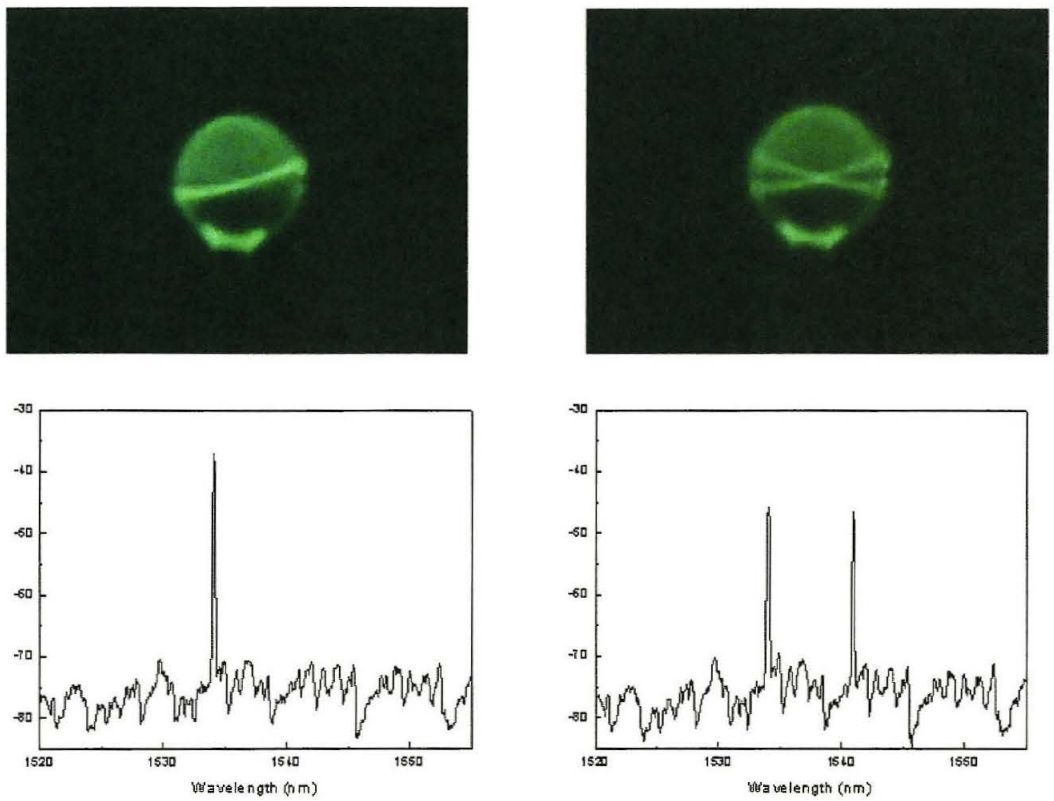

(a) (b)

Figure 7.10 Pump ring pattern switches as the polarization state of the pump beam changes. Each ring supports lasing emission at a different wavelength.

7.10 shows the pump coupling switches between the single ring pattern and the double crossing ring pattern due to the different polarization state of the input pump beam. Each pump ring excites lasing emission at a different wavelength. Consequently, the microsphere laser is operating at either single frequency or double frequency as the pump pattern switches.

7.3.3 Single-Mode Laser Oscillation

In our experiments, single frequency lasing operation was routinely observed by adjusting the taper-sphere coupling, pump wavelength, ring patterns as well as polarization states. It is somewhat surprising that a single-mode output can be excited, given the large number of possible lasing modes within the sphere and very broad gain bandwidth (typically from 1510 nm to 1560 nm for erbium ions). We attribute this to the unique mode selection mechanisms existing in the taper coupled microsphere laser.

As we have shown, the pump wave couples into semiclassical ring orbits in the phosphate glass microsphere because of the high ytterbium doping induced strong damping. For the laser wavelength, however, the attenuation is far less than that in the pump band, and the laser modes will be exact eigen modes of the spheroid and thus have an angular distribution of the spherical harmonics $Y_l^m(\theta,\phi)$, which rotate around the equator centered at a latitude given by $\cos^{-1}(m/l)$. Consequently, if the pump wave coupled into crossing ring orbits, there are a large set of laser modes that do not significantly overlap each other, and yet have near-equal overlap with the gain region. This reduces mode competition and allows for multimode lasing. When the pump volume is a single equatorial ring (corresponding to a fundamental pump mode), the prospective laser modes in the 1550 nm band would also be fundamental whispering gallery modes because of their highest spatial overlap with the gain region. Thus, lasing occurs first where the spectral gain is greatest, and the other modes remain sub-threshold due to homogeneous gain clamping.

In previous fused silica microsphere laser experiments [2], a relatively broadband laser diode was used, which pumped a number of whispering gallery modes simultaneously, thus expanding the gain region within the microsphere to nearly 10 times the volume of a single whispering gallery mode and resulting in multi-m mode excitation. In addition, the pump absorption is relatively small, which allows high spatial overlap for $m \neq l$ modes. Work on millimeter sized Nd:YAG spherical laser resonators [9] shown similar laser mode selection as in our experiment when a narrow linewidth pump source was focused to optimize coupling to s single whispering gallery mode within the sphere.

A thorough study on the lasing spectrum has confirmed our inference. Fig. 7.11 shows again the laser spectrum, but with calculations of the laser mode wavelengths. The free spectrum range (FSR) for the l index is approximately 9 nm for a 57 μm diameter sphere, which matches the period of the deep troughs in the collected spontaneous emission power. There are three distinct peaks within each FSR_l over nearly the entire emission bandwidth. These peaks are sawtooth-like with a sharp long wavelength edge. This is due to a combination of the spatial mode selection performed by the annular pump region and the spatial filtering performed by the output coupling of the taper. Due to the oblate eccentricity of this microsphere, each set of $2l + 1$ whispering gallery modes with fixed polarization and n, l mode numbers spans a wavelength range of approximately 6 nm, with wavelength increasing with m value. Within each peak there is a gradual rise in out-coupled power as the wavelength is increased and

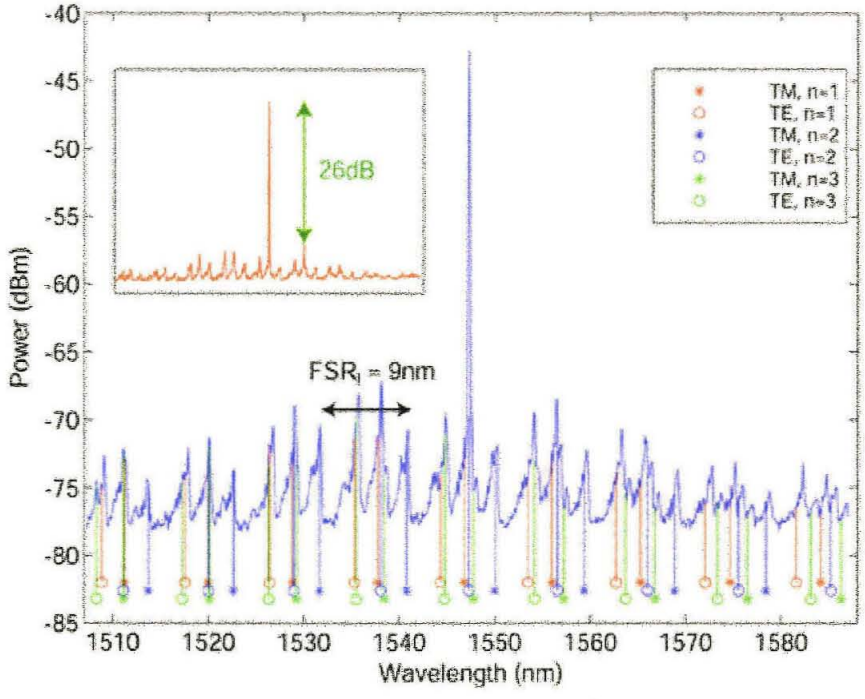

Figure 7.11 Photoluminescence spectra of the 980 nm pumped microsphere. The FSR_l is clearly visible as periodic deep troughs in the emission. The calculated wavelengths of the first three radial mode numbers (n) for TE and TM polarizations are plotted for varying l values. The PL at twice threshold is plotted in the inset.

the m number increases towards l. This is a result of the improved overlap with the annular gain region for $m \approx l$ whispering gallery modes and the improved taper coupling.

The presence of only three dominant peaks within each FSR_l can be attributed to the taper coupling mechanism. The diameters of the taper and sphere in this experiment are such that the fundamental taper mode is phase matched best with the $n = 1$ TE and TM fundamental ($m \approx l$) whispering gallery modes of the sphere at the pump wavelength. Thus, the pump volume is restricted to a micron or so beneath the sphere surface. Emission then occurs

predominantly into the lower order radial modes at $1.5\ \mu m$. The wavelengths of the fundamental TE and TM whispering gallery modes for $n = 1, 2, 3$ are calculated using Eq. (2.9) with previously measured microsphere parameters ($D = 57\ \mu$m, $n_s = 1.521$) and plotted along with the PL spectra in Figure 7.11. In the whispering gallery mode calculation the radius of the microsphere was adjusted by tenths of microns in order to center the three photoluminescence peaks with the nearest set of calculated peaks. Notice that due to the near (accidental) degeneracy in this wavelength range, the possible six distinct peaks merge into three. The deep troughs in the photoluminescence, which occur at the FSR of the l mode number, are also very well predicted by the calculation. A further confirmation of this model is that as the calculated mode peaks start to separate for longer wavelengths we see that the individual peaks in the PL also start to break up. The additional subpeaks that are more weakly present in the spectrum are due to higher radial mode number WG modes.

From the fit of the whispering gallery mode resonance peaks to the laser spectrum in Fig. 7.11, the laser mode is most likely a $m \approx l$, $TM_{n=1}$ or $TE_{n=2}$ mode as the fundamental lower radial number modes will have the highest overlap with the narrow annular gain region near the sphere surface.

7.3.4 Temporal Response of the Laser Oscillation

Upon further investigation of the microsphere laser, we noticed that the relaxation oscillations of the microsphere laser were very strong. This prompted

us to investigate the temporal response of the laser. We found that the laser was self-pulsing with a period of roughly 15 μs and a pulse width of 500 ns. This can be explained by the large amount of unpumped, absorbing region within the sphere. The taper provides a significant amount of loading for sphere modes at the equator [15], thus reducing the Q of equatorial modes. The actual laser mode will be determined by balancing the overlap with the gain region against the loading of the taper. This will tend to push the laser mode slightly away from the equator resulting in significant overlap with pumped as well as unpumped regions within the sphere. This is amplified even more for crossing-ring pumped regions. Instability in lasers which have modal overlap with both gain and absorbing regions is quite common [16] and results from the nonlinear dynamics associated with absorption saturation.

7.4 Bi-Sphere Experiment

One of the advantages in using a fiber taper to couple light into and out of a microsphere resonator is the ability to cascade a series of devices, each addressing a single wavelength channel on the fiber taper. As an example of this, we placed two phosphate glass microspheres, one after the other, along a fiber taper. In Fig. 7.12 we show a single taper with two differently sized microspheres attached. In this case the first laser has a wavelength of 1535 nm and after placing the second microsphere in contact with the taper a second laser line at 1533 nm appears. In

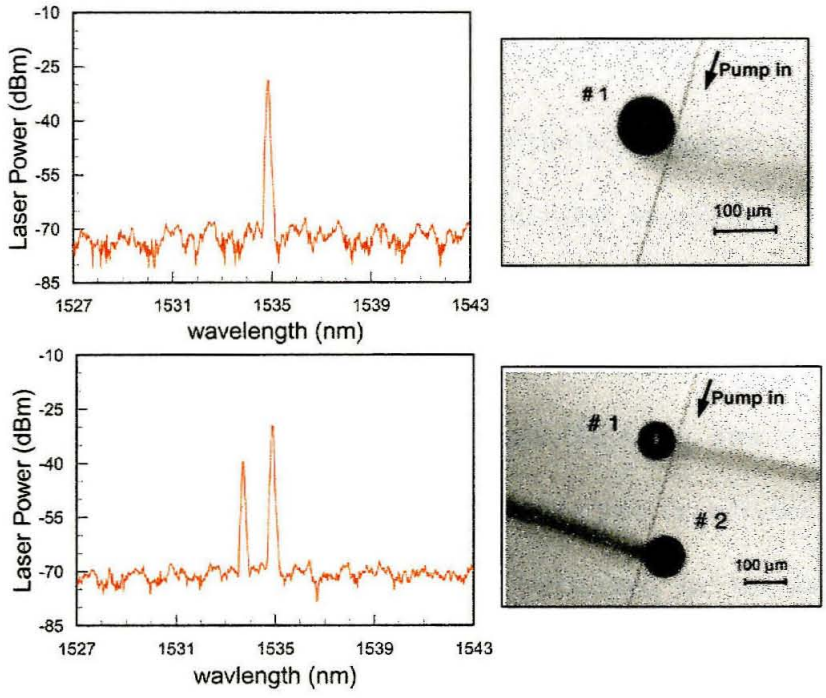

Figure 7.12 Bi-sphere system in which two spheres have been placed on the same taper and pumped by a single 980 nm laser source, producing two separate laser lins at 1533 nm and 1535 nm.

this case the first microsphere laser seems relatively unaffected by the presence of the second microsphere; however, one can imagine passive and active microsphere systems forming "photonic molecules" [16] where coupling is provided by the fiber taper.

7.5 Hybrid Taper Coupled Microsphere Lasers

In this section, we consider the optimization of the taper-sphere coupling for the microsphere laser system where at least two distinct wavelength bands (pump and laser) are engaged.

The taper coupler used in our previous experiment was fabricated using a standard 1550 nm single-mode fiber (SMF), and the taper size was tailored to phase matching at the pump wavelength. There are two drawbacks for this kind of simple coupler. First, the taper size is not optimized for the laser emission, which requires larger size compared to the pump wave to obtain phase matching. Laser output power coupled into higher-order taper mode will be radiated away before reaching the detector. Secondly, the 1550 nm SMF generally has a cut-off wavelength at 1250 nm. It is thus a multimode waveguide for the 980 nm pump wave and supports both LP_{01} (fundamental) and LP_{11} (second higher order) modes as shown in Fig. 7.13. The power carried by the two modes depends on the launching condition. As a result, even if the taper is pulled adiabatically, there exist both fundamental taper mode (HE_{11}) and higher-order taper modes (HE_{21}, TE_{01} and TM_{01}) at the taper waist region due to the following adiabatic transition:

$$LP_{01} \rightarrow HE_{11}$$
$$LP_{11} \rightarrow HE_{21}, TE_{01}, TM_{01}.$$

The higher-order taper modes HE_{21}, TM_{01}, TE_{01} hence carry a fraction of input pump power. Once phase matched to the fundamental taper mode HE_{11}, the

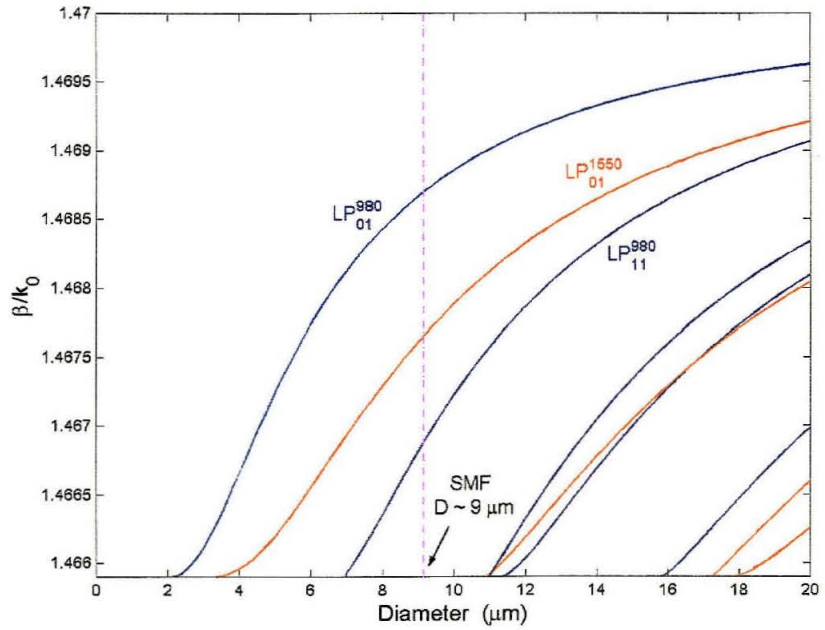

Figure 7.13 Effective index of fiber modes in a standard 1550 nm single-mode fiber. If 980 nm pump wave is launched into such a fiber, there exists both LP_{01} and LP_{11} depending on the input condition.

sphere fundamental mode will mismatch to higher-order modes thereby limiting sphere excitation.

An ideal microsphere laser coupler, therefore, would be a dual taper system similar to what was used in our earlier work on a microsphere add/drop filter [17], except that one of the adiabatic tapers is made from a 980 nm single-mode fiber and optimized for the pump wavelength, while the other one is made from a 1550 nm single-mode fiber and optimized for the laser wavelength. Due to the different size requirements for the two taper couplers, we have to fabricate the tapers separately and then bring them close enough to coupling to the

microsphere. There is, however, unexpected difficulty in positioning these two couplers with our current lab equipment.

We hence propose a substitute coupling method, so-called hybrid fiber taper coupler, for the sake of solving the second problem as stated above.

The hybrid fiber taper coupler is a combination of both 980 nm SMF and 1550 nm SMF, as shown in figure 7.14. The hybrid fiber taper was prepared in two steps. First, a section of 1550 nm SMF is spliced with a section of 980 nm SMF. It is then put on the top of a Hydrogen flame, with the splice in the center of the heating source. The fiber is tapered by stretching it slowly apart by about one inch in total to obtain a very narrow waist of about 1-2 microns and a relatively low taper loss. Before tapering, the hybrid fiber had a loss of less than 0.2 dB, which resulted from the splice and connector losses. An additional 0.5 dB loss was measured after tapering.

Since the taper modes are defined by the taper size and the material refractive index (i.e., the old core is vestigial), the splice in the center region of the hybrid taper has no deleterious effect on the taper performance when compared to normal (non-hybrid) tapers. However, as illustrated below, the hybrid fiber taper has the significant advantage that it transitions to SMF fiber optimized for propagating either the 980 nm pump source or the 1550 nm laser emission.

The diameter of the Er:Yb co-doped phosphate microsphere in this experiment was about 45 μm and the taper size that best matched the sphere

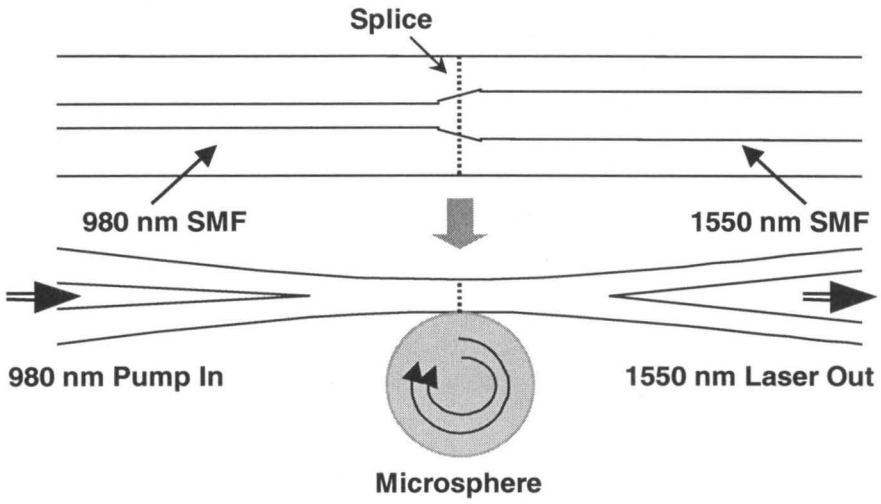

Figure 7.14 Schematic of hybrid fiber taper coupling to a microsphere laser.

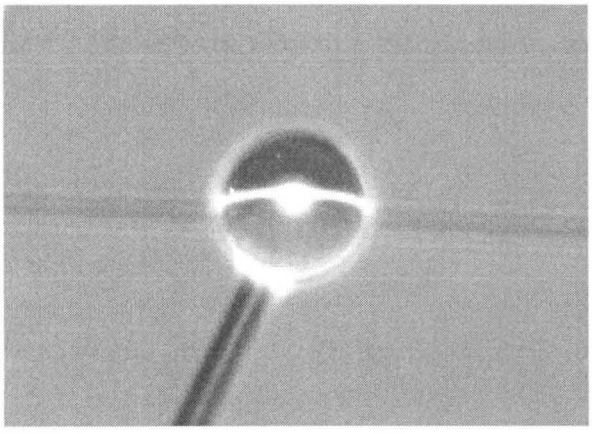

Figure 7.15 Magnified photograph of the hybrid taper-sphere coupling system. The hybrid fiber taper is placed underneath the sphere with 980 nm single-mode fiber at the left side and 1550 nm single-mode fiber at the right side.

was about $1.5\,\mu m$. Figure 7.15 shows a magnified image of the taper-sphere coupling system. The hybrid taper was placed underneath the sphere with the

980-nm SMF at the left side and 1550-nm SMF at the right side. The pump wave was launched from a 980-nm single-mode tunable external-cavity laser. In this case, it shows the pump wave was resonantly coupled into a fundamental whispering gallery mode, producing a narrow equatorial-ring gain region. The pump transmission response was measured at the other end of the hybrid fiber taper by scanning the wavelength of the pump laser, as shown in Fig. 7.16. Comparing with the pump transmission spectrum of a conventional fiber taper coupled microsphere laser as shown in Fig. 7.3, we can easily conclude that the power scattering induced by the higher order pump modes was nearly suppressed in the hybrid taper coupled microsphere laser system as the off-resonance transmission was close to 1, while it was only 50%-60% in average in the conventional system. This confirms the improvement made by the hybrid taper configuration.

Lasing action was observed with the hybrid fiber taper coupled microsphere by tuning the pump wavelength to a pump band resonance of the sphere. Figure 7.17 shows a typical laser spectrum (as collected from the 1550 nm single mode fiber end) read from an optical spectrum analyzer (OSA) with resolution of 0.08-nm. In order to resolve the fine spectral features of the laser, a high finesse (about 5,000) scanning Fabry-Perot (FP) etalon with a spectral resolution of a few MHz was used to analyze the spectrum. Figure 7.18 shows the resulting microsphere laser spectrum. For reference, a single frequency laser with known linewidth of about 300 kHz is also shown. The spectral output shows the single frequency nature of the microsphere laser.

A plot of laser power collected from the SMF fiber as a function of total pump power absorbed and scattered is shown in figure 7.19. As high as 112 μW output laser power was measured with the laser still remaining single mode. The differential quantum efficiency of this laser is calculated to be about 12%. In our previous work [5] using a conventional 1550 nm single-mode fiber taper, the quantum efficiency was about 2.6%, while it was about 0.037% in work [2] that used the prism coupling technique.

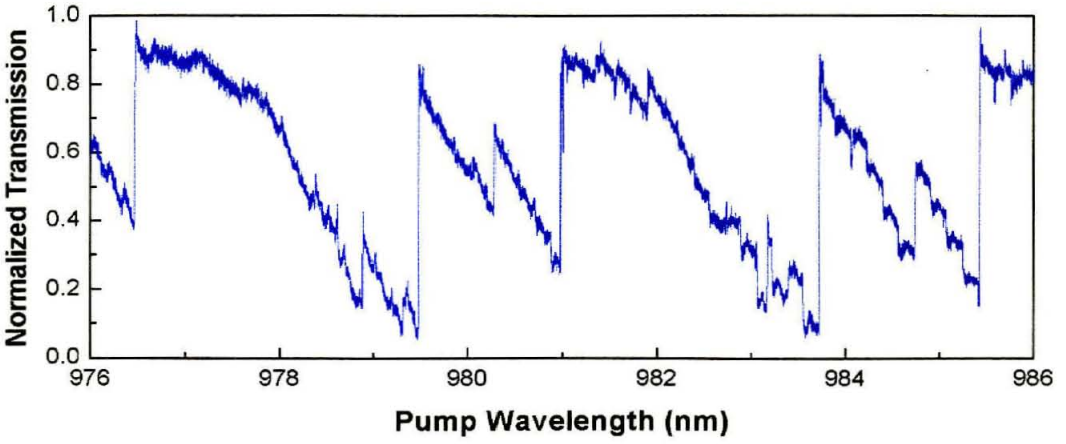

Figure 7.16 Pump band transmission spectrum of the hybrid-taper coupled microsphere laser.

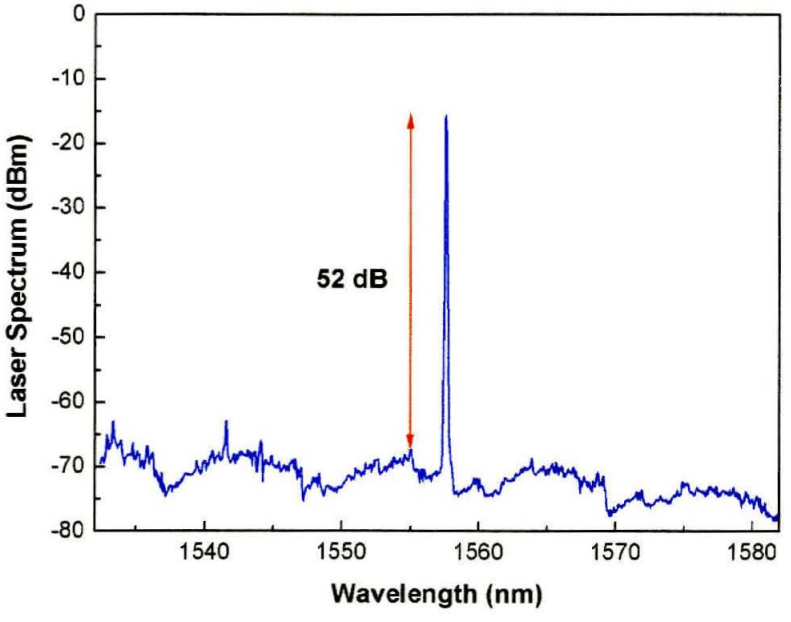

Figure 7.17 Laser spectrum collected from the 1550 nm fiber end.

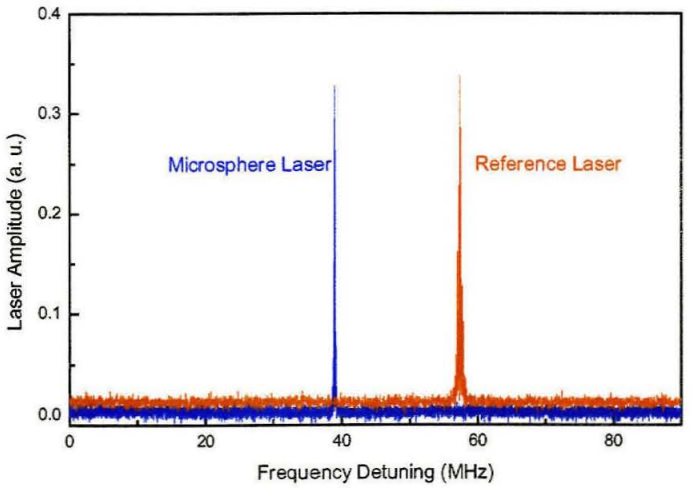

Figure 7.18 Laser spectrum observed using a Fabry-Perot etalon showing the single mode nature of the microsphere laser. Reference laser scan is from a single-mode laser with a linewidth of 300 kHz.

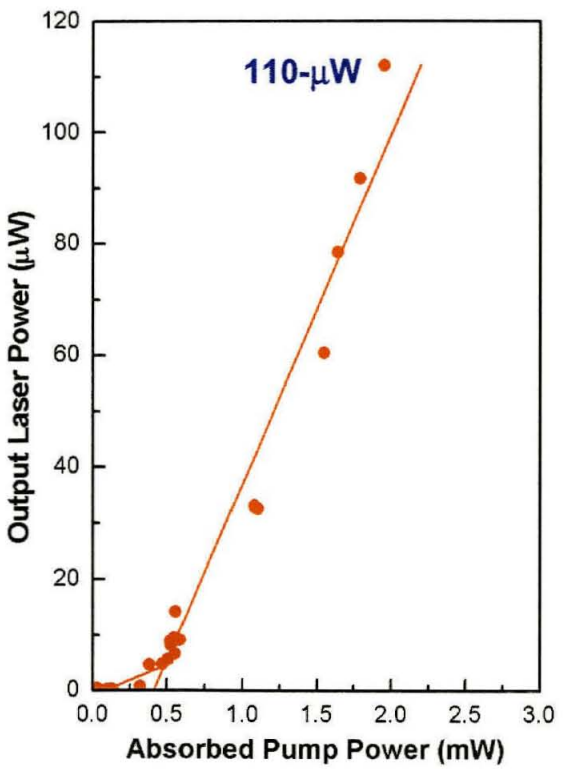

Figure 7.19 Measured, total output laser power versus absorbed pump power in the microsphere.

Bibliography

[1] M. L. Gorodetsky, A. A. Savchenkov, and V. S. Ilchenko, "Ultimate Q of Optical Microsphere Resonators," *Optics Letters*, vol. 21, pp 453-455, 1996.

[2] V. Sandoghdar, F. Treussart, J. Hare, V. Lefevre-Segin, J. -M. Raimond, and S. Haroche, "Very Low Threshold Whispering-Gallery-Mode Microsphere Laser," *Physics Review A*, vol. 54, pp 1777-1780, 1996.

[3] W. von Klitzing, E. Jahier, R. Long, F. Lissillour, V. Lefevre-Seguin, J. Hare, J. M. Raimond, and S. Haroche, "Very Low Threshold Lasing in Er^{3+} Doped ZBLAN Microsphere," *Electronics Letters*, vol. 35 pp 1745-1746, 1999.

[4] F. Lissillour, P Feron, N. Dubreuil, P. Dupriez, M. Poulain, G. M. Stephan, "Erbium-Doped Microspherical Lasers at 1.56 μm," *Electronics Letters*, vol. 36, pp 1382-1384, 2000.

[5] M. Cai, O. Painter, K. Vahala, and P.C. Sercel, "Fiber-Coupled Microsphere Laser," *Optics Letters*, vol. 25, pp. 1430-1432, 2000.

[6] M. Cai, and K. Vahala, "High Efficient Microsphere Laser Coupled Using a Hybrid Fiber Taper," to be published in *Optics Letters*.

[7] P. Laporta, S. Taccheo, S. Longhi, O. Svelto, and C. Svelto, "Erbium-Ytterbium Microlasers: Optical Properties and Lasing Characteristics," *Optical Materials*, vol. 11, pp 269-288, 1999.

[8] Kigre QX/Er sample data sheet.

[9] T. Baer, "Continuous-Wave Laser Oscillation in a Nd-YAG Sphere," *Optics Letters*, vol.12, pp.392-394, 1987.

[10] M. Cai and K. Vahala, "Highly Efficient Optical Power Transfer to Whispering Gallery Modes Using a Symmetrical Dual-Coupling Configuration," *Optics Letters*, vol. 25, pp. 260-262, 2000.

[11] R. Francini, F. Giovenale, U. M. Grassano, P. Laporta, S. Taccheo, "Spectroscopy of Er and Er-Yb-Doped Phosphate Glasses," *Optical Materials*, vol. 12, pp. 417-425, 2000.

[12] M. L. Gorodetsky, V. S. Ilchenko, "High-Q Optical Whispering Gallery Microresonators: Precession Approach for Spherical Mode Analysis and Emission Patterns with Prism Couplers," *Optics Communications*, vol. 112, pp. 133-143, 1994.

[13] J. C. Swindal, D. H. Leach, and R. K. Chang, "Precession of Morphology-Dependent Resonances in Nonspherical Droplets," *Optics Letters*, vol. 18, pp. 191-193, 1993.

[14] J. C. Knight, N. Dubreuil, V. Sandoghdar, J. Hare, V. Lefevre-Seguin, J. M. Raimond, and S. Haroche, "Mapping Whispering Gallery Modes in Microspheres with a Near Field Probe," *Optics Letters*, vol. 20, pp. 1515-1517, 1995.

[15] B. E. Little, J.P. Laine and H. A. Haus, "Analytic Theory of Coupling from Tapered Fibers and Half-Blocks into Microsphere Resonators," *Journal of Lightwave Technology*, vol. 17, pp. 704-715, 1999.

[16] T. Mukaiyama, K. Takeda, H. Miyazaki, Y. Jimba, and M. Kuwata-Gonokami, "Tight-Binding Photonic Molecule Modes of Resonant Bispheres," *Physics Review Letters*, vol. 82, pp. 4623-4626, 1999.

[17] M. Cai, G. Hunziker, and K. Vahala, "Fiber-Optic Add-Drop Device Based on a Silica Microsphere-Whispering Gallery Mode System," *IEEE Photonics Technology Letters*, vol. 11, pp. 686-687, 1999.